



# Utilizing gradient samples to investigate solid state dewetting of a bimetallic Au - Ni - system

# **Master Thesis**

by Christian Volland

Supervisor: M.Sc. Martin Dierner

Erlangen, December 2023

**Institute of Micro- and Nanostructure Research** 

Prof. Dr. rer. nat. habil. Erdmann Spiecker Friedrich-Alexander-Universität Erlangen Nürnberg

# Acknowledgements

As first I want to thank Prof. Spiecker for reaching out to me, to conduct my master thesis on this wonderful topic at his department, but also for his investment in my thesis and research.

Secondly, I am grateful for having Martin Dierner as my supervisor. Not only did he guide me through my time as a Hiwi and latter my master thesis, but he also encouraged me to do things beyond those topics. Without him I would have missed some amazing moments of my live, like going onto a conference and giving a presentation in front of way too many people.

In addition, I would like to thank Johannes Will for his valuable knowledge and input on thin film systems and joying up every meeting or 'teambuilding exercises' I was able to attend.

The next thanks go to our technician Robert Branscheid who build the whole gradient deposition device on his own, which worked perfectly from the first day on. He made it possible that the result came quick and easy without any headache with the deposition process it-self.

I also want to thank everyone else from the institute of micro and nanostructure research. The time at the department was wonderful and went by way to quickly, because it was so joyful. I am grateful for the environment at which I worked for the last one and a half years thanks to all of you.

Lastly, I want to thank my family and girlfriend for being there for me in every time. I love all of you for helping through everything and knowing that no matter what I have people I can count on that we be there for me.

# **Abstract**

In this study, the kinetics of Solid State Dewetting (SSD) and the texture evolution of the AuNi system on  $\alpha$ -Al $_2$ O $_3$  is investigated. To achieve an analysis of the whole concentration range, samples of 40 nm thickness with a concentration gradient were successfully synthesized via electron beam physical vapour deposition, as proofed by SEM-EDX and local XRD measurements. Afterwards samples were heated at different temperatures and time. The shape and morphology of the samples were analysed via SEM imaging and the texture evolution via EBSD.

At 875 °C the samples showed typical SSD which changes over the concentration range. Between 10 at% and 35 at% Au the SSD kinetic decreases but increases afterwards in a concentration range from 35 at% to 75 at%. With increasing time areas of slow SSD start to catch up with the rest of the sample. The texture of the samples shows an orientation relation (OR) I, with an out of plane (OOP) alignment of the {111} AuNi plane with the {0001} planes of the sapphire substrate and an in-plane alignment of the {110} planes of the AuNi alloy with the {10-10} planes of the sapphire. At low Au concentrations the OR is only slightly present, but enhances throughout the sample, reaching a nearly perfect OR I close to the lattice matching.

At higher temperatures above 910 °C, an area of very fast-dewetting forms around the lowest melting point of the system. Comparing the dewetting behaviour with samples heated at 1000 °C shows that inside of the fast-dewetting area liquid state dewetting (LSD) is most likely occurring. Additionally, inside the fast-dewetting area the OR is lost. Increasing the process temperature to 1000 °C reveals that three areas exist on the sample, depending on the relation between process temperature and solidus and liquidus line. If the liquidus line is lower than the process temperature the OR is lost and LSD is happening, but if only the solidus line is surpassed the sample shows LSD but no loss of OR.

# Eidesstattliche Erklärung

Ich versichere, dass ich die Arbeit ohne fremde Hilfe und ohne Benutzung anderer als der angegebenen Quellen angefertigt habe und dass die Arbeit in gleicher oder ähnlicher Form noch keiner anderen Prüfungsbehörde vorgelegen hat und von dieser als Teil einer Prüfungsleistung angenommen wurde. Alle Ausführungen, die wörtlich oder sinngemäß übernommen wurden, sind als solche gekennzeichnet.

| Erlangen, 05.12.2023 |  |  |                   |
|----------------------|--|--|-------------------|
|                      |  |  | Christian Volland |

# Content

| 1  | In                                   | ntroduction 1                                     |  |      |  |  |  |  |
|--|--------------------------------------|---|--|------|--|--|--|--|
| 2  | Fundamentals                         |   |  |      |  |  |  |  |
|  | 2.1                                  | Soli  | d-state dewetting                                  | 2    |  |  |  |  |
|  | 2.                                   | 1.1   | Hole formation                                     | 2    |  |  |  |  |
|  | 2.                                   | 1.2   | Hole growth  | 3    |  |  |  |  |
|  | 2.                                   | 1.3   | Winterbottom shape                                 | 4    |  |  |  |  |
|  | 2.1.4                                |   | Kinetics of SSD                                    | 5    |  |  |  |  |
|  | 2.                                   | 1.5   | Influence of alloying                              | 6    |  |  |  |  |
|  | 2.2                                  | Liqu  | uid state dewetting                                | 7    |  |  |  |  |
|  | 2.3                                  | Epit  | taxy of metals on ceramic                          | 9    |  |  |  |  |
|  | 2.4                                  | Me  | Iting point depression of thin films               | . 10 |  |  |  |  |
| 2.4.1  |                                      | 4.1   | Film thickness                                     | . 10 |  |  |  |  |
|  | 2.                                   | 4.2   | Grain size   | . 11 |  |  |  |  |
| 3  | Materials and Methods                |   |  |      |  |  |  |  |
| 3.1 Gold Nickel-system on $\alpha$ -Al <sub>2</sub> O <sub>3</sub> |                                      |   |  | . 13 |  |  |  |  |
|  | 3.2 Electron beam physical vapour de |   | ctron beam physical vapour deposition (e-beam PVD) | . 14 |  |  |  |  |
| 3.3 Scanning electron microscopy (SEM)                             |                                      | Sca   | nning electron microscopy (SEM)                    | . 16 |  |  |  |  |
|  | 3.                                   | 3.1   | Electron beam – specimen interactions              | . 16 |  |  |  |  |
|  | 3.                                   | 3.2   | Electron backscatter diffraction (EBSD)            | . 19 |  |  |  |  |
| 3.4 Foo  |                                      | Foc   | used ion beam                                      | . 23 |  |  |  |  |
|  | 3.5 Scan                             |   | nning transmission electron microscopy (STEM)      | . 25 |  |  |  |  |
|  | 3.6                                  | X-ra  | ay diffraction (XRD)                               | . 27 |  |  |  |  |
|  | 3.7                                  | 7 Basics of combinatorial material investigations |  |      |  |  |  |  |
|  | 3.8                                  | San   | nple preparation and analysis                      | 31   |  |  |  |  |

|   | 3.8 | 3.1                             | Precleaning procedure                       | 1 |  |  |
|---|-----|---------------------------------|---|---|--|--|
|   | 3.8 | 3.2                             | Deposition process                          | 1 |  |  |
|   | 3.8 | 3.3                             | Heating of samples                          | 2 |  |  |
| 4 | Re  | sults                           |   | 4 |  |  |
|   | 4.1 | Pro                             | of of concept                               | 4 |  |  |
|   | 4.2 | Pro                             | cess-Time variation at 875°C                | 8 |  |  |
|   | 4.3 | 3 Process-temperature variation |   |   |  |  |
|   | 4.4 | LSD                             | at 1000°C                                   | 6 |  |  |
| 5 | Dis | scussi                          | on5   | 1 |  |  |
|   | 5.1 | Pea                             | k analysis of local XRD measurements5       | 1 |  |  |
|   | 5.2 | Influ                           | uence of Au concentration onto SSD5         | 3 |  |  |
|   | 5.3 | Influ                           | uence of time onto SSD5                     | 5 |  |  |
|   | 5.4 | SSD                             | at higher temperatures5                     | 7 |  |  |
|   | 5.5 | Text                            | ture evolution at 900 °C6                   | 0 |  |  |
|   | 5.6 | Text                            | ture evolution of partially molten samples6 | 2 |  |  |
| 6 | Со  | nclus                           | ion 6                                       | 6 |  |  |
| 7 | Lis | t of F                          | igures 6                                    | 8 |  |  |
| 8 | Re  | References                      |   |   |  |  |
| 9 | An  | nend                            | ix  | q |  |  |

# List of Abbreviations

ADF annular dark field

AE Auger electrons

BF bright field

BSE back scattered electrons

CL cathodoluminescence

CTEM conventional transmission electron microscopy

CVD chemical vapour deposition

DI dictionary indexing

e-beam electron beam

EBSD electron backscattered diffraction

ECD equivalent circle diameter

EDX energy dispersive x-ray

fcc face centered cubic

FIB focused ion beam

HAADF high angle annular dark field

HI Hough indexing

LSD liquid state dewetting

MAD mean angular deviation

MPD melting point depression

MUD mean uniform density

OOP Out of plane

OR orientation relation

PVD physical vapour deposition

RTA rapid thermal annealing

SE secondary electrons

SEM scanning electron microscopy

SSD solid state dewetting

STEM scanning transmission electron microscopy

XRD x-ray diffraction

# 1 Introduction

Metallic nanoparticles exhibit fundamental different properties compared to their respective bulk variant. By tuning the size and shape of metallic nanoparticles, their magnetic, electrical, optical, and chemical properties can be adjusted. This makes them interesting for biomedical application, imaging, and heterogeneous catalysis. The use of bimetallic alloys opens an additional way of changing existing properties of metallic nanoparticle. Alloying either enhances existing properties, beyond the respective pure metals, or adds additional properties to the system. For instance, nanoparticles of Pt and Cu show an enhanced performance for photocatalytic H<sub>2</sub> evolution than the respective pure elements [1]–[3].

Bimetallic nanoparticles can be produced by various different techniques, which are divided into bottom-up and top-down approaches. One of the most effective ways of producing them is called solid state dewetting (SSD). SSD is a phenomena, which happens when a thin metal film is heated up to a temperature well below the melting temperature of the respective metal. To minimize the surface energy, the metal film agglomerates and forms nanoparticles. [4]–[6].

The aims of this master thesis are firstly, to produce a combinatorial sample with a concentration gradient of a bimetallic alloy and secondly, to utilize this sample for investigating the concentration dependent thermal stability and microstructural evolution of a gold (Au) nickel (Ni) thin film system.

# 2 Fundamentals

# 2.1 Solid-state dewetting

SSD is a phenomenon which describes the process of agglomeration of thin films into particles via surface-diffusion, while the temperature is well below the melting point. The process of SSD is generally divided into three different stages. The first stage of SSD is the formation of holes, followed by the growth of these holes and the last step is the break-up of elongated structures into small particles, also known as ligament break-up [6]. The three steps will be discussed in more detail in the upcoming sections.

#### 2.1.1 Hole formation

For polycrystalline thin films, hole formation happens at sites where the crystal is not in its most ordered state. These are for example the edges of the film, grain boundaries or grain boundary triple junctions. To minimize the surface energy, spherical shapes evolve leading to a height increase near to the grain boundary and the sinking of the film into the grain boundary (see Figure 1). This process is called grain boundary grooving, which was first described by Mullins et al. [7]. In his study he investigated the transport mechanism, which guide the formation and growth of grooves. He conducted, that for thin films thinner than a  $\mu m$  the main transport mechanism is surface self-diffusion. The rate of morphology change is thereby described via the Mullins coefficient B:

$$B = \gamma \frac{D_{s} v}{kT} \Omega^{2} \tag{1}$$

with  $\gamma$  being the surface energy,  $D_s$  the surface self-diffusion coefficient, v the number of mobile surface atoms, k the Boltzmann constant, T the temperature, and  $\Omega$  the atomic volume.

Mullins also observed that the rate of groove formation and thus the time it takes to form a hole  $\tau_n$  scales with the surface self-diffusion coefficient as well as the thickness of the film d [6], [8]:

$$\tau_n \propto \frac{d^4}{D_s} \tag{2}$$

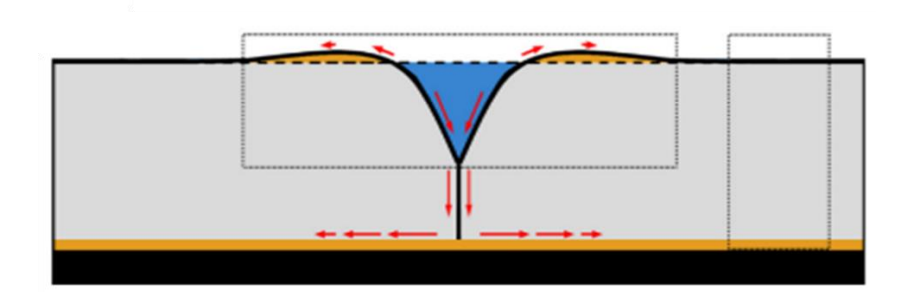


Figure 1: Schematic representation of a Mullins type grooving of a grain boundary. At the position of the grain boundary the material sinks in, reducing the height of the film locally. This process proceeds until the depth of the groove exceeds the film thickness. Simultaneously material moves from the grain boundary to the edges of the boundary, which results in a local increase of film thickness. The main mass transport mechanism during SSD is surface self-diffusion [8].

## 2.1.2 Hole growth

The second step of SSD is the growth of the just-formed holes. In general, this happens through the retraction of edges (see Figure 2 a i). During the retraction the material bulges up directly at the front of the retracting material (Fig.2 a ii) however, directly behind the height of the film decreases (see Figure 2 a iii). This process reduces the curvature of the retracting rim, which is one of the main driving forces for SSD. The retraction of the edge proceeds as long as the rim is still connected to the rest of the thin film. When the valley, which has formed behind the rim, reaches the substrate, the rim is disconnected from the rest of the film (see Figure 2 a iv). This process is known as rim pinch-off mechanisms [6], [9].

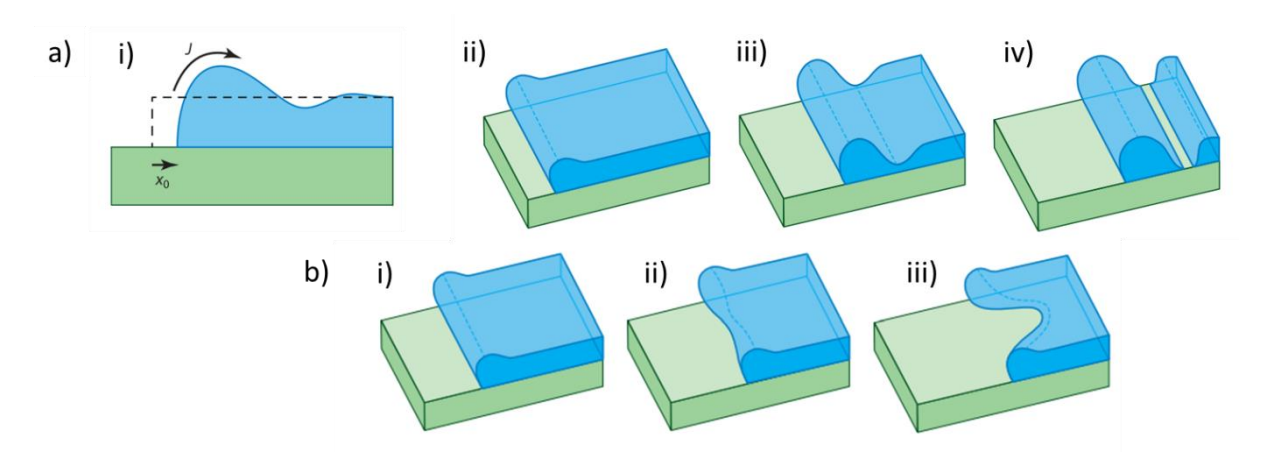


Figure 2: The edge of a thin film will retract during SSD. a) During the retraction of the edge the material height will increases directly at the edge (ii) but decreases behind the edge (iii), which will lead to the edge being pinched-of (iv). b) If the edge does not retract uniformly finger like instabilities form [9].

It could also happen that the edge does not retract with the same rate at all points. In this case, finger-like structures evolve during the edge retraction. This process is called fingering instability (see Figure 2 b). Contrary to the rim pinch-off mechanisms, there is no distinct stop of this process. The fingering instability will proceed until there is no film left. In all cases the resulting structures are elongated, finger-like structures. These structures are also unstable and will break down into individual particles, due so-called Rayleigh-Plateau instability, which can be seen in Figure 3 [6], [10], [11].

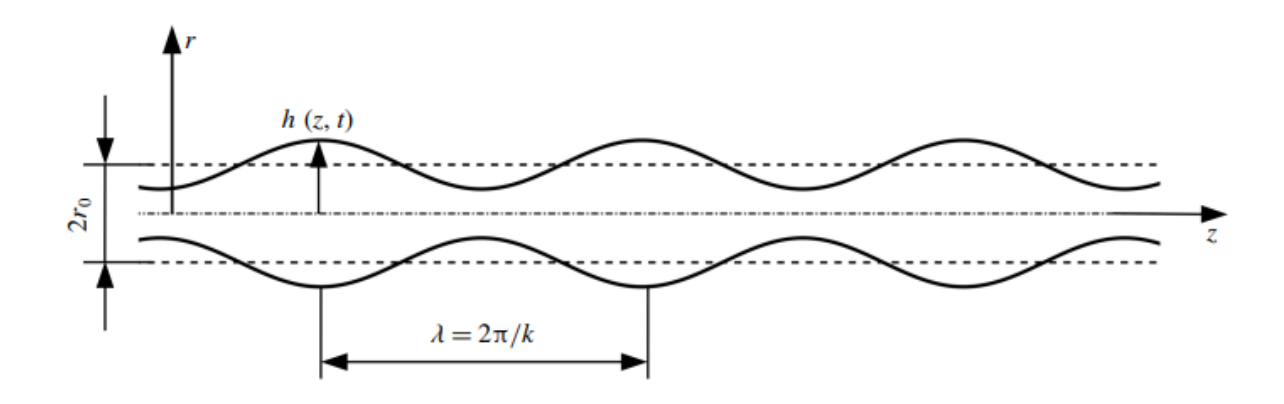


Figure 3: The Rayleigh plateau instability is shown in this graph. This phenomena was firstly covered for liquid jets, which, if thin enough, will break down into small droplets. The distance between the droplets, and thereby their resulting size, depends on the thickness of the jet [11].

#### 2.1.3 Winterbottom shape

In the case of a liquid droplet on top of a substrate, spheres with different wetting angles form, depending on the interface energy between liquid, solid and the atmosphere. In the case of solid droplets, the behaviours are in some ways equivalent, but the sphere will not be perfectly round. Due to the crystallinity of metals, different planes exhibit different surface energies, thus leading to the formation of a Wulff-shape [12]. Additionally, the interaction of the particle with the substrate influences the precise shape. These interactions were firstly covered by Winterbottom [5]. The general Winterbottom-shape is similar to that of Wulff, however only parts of the polyhedral are visible. The behaviour is close to that of a liquid droplet on a surface. Depending on the wetting angle, a complete sphere is visible (in the case of no wetting) or only the tip of the sphere. This is shown in Figure 4. The centre of the Winterbottom-shape, which is called Wulff point, can be used to determine the interface energy between particle- and substrate. This is done by comparing the distance between the

Wulff point and the substrate  $(R_1)$  with the distance between the surface of the particle and the Wulff point  $(R_2)$ :

$$\frac{R_1}{R_2} = \frac{\gamma_{sp} - \gamma_{sv}}{\gamma_{pv}} \tag{3}$$

, where  $\gamma_{sp}$   $\gamma_{sv}$  and  $\gamma_{pv}$  are the interfacial energies between substrate and particle, substrate and vapour and particle and vapour, respectively.

Although this is an elegant routine to determine the different energies, this technique is related to some limitations: The particle has to be a single crystalline particle, and the substrates surface has to be coplanar to the upper most facet of the particle [5], [6], [13]–[15].

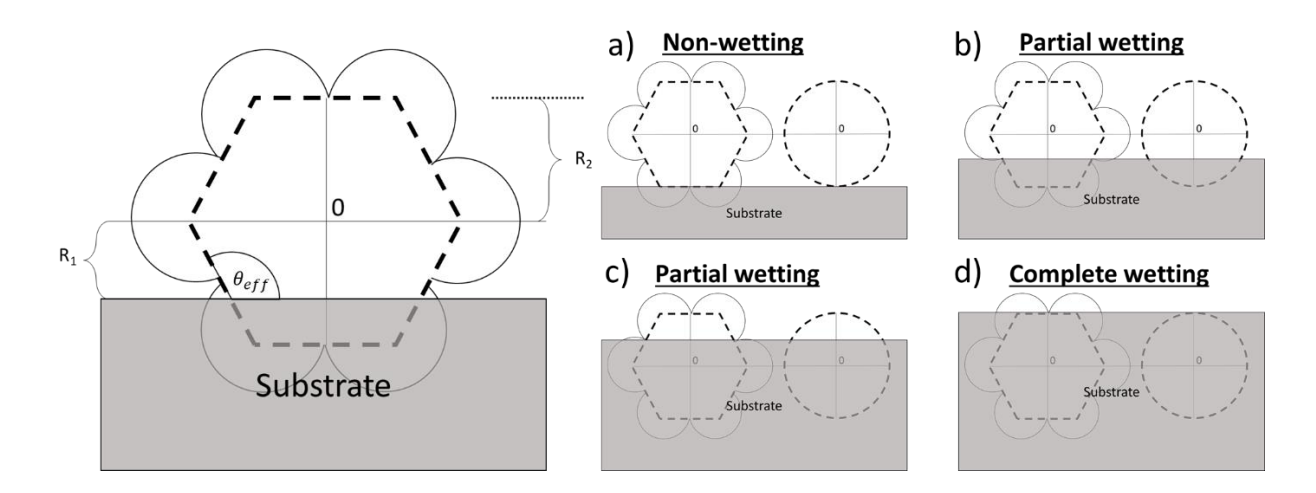


Figure 4: The shape of the metal droplets can be described similar to a liquid droplet. In the case of a liquid droplet the angle between substrate and particle is dependent on the wetting behaviour. In the case of a solid droplet the distance between substrate, the centre of the Wulff-plot and the upper most facet is the indication for the wetting behaviour, which is depicted on the left side. Image a) shows a solid particle and a liquid droplet which are not wetting at all, image b) and c) partial wetting and image d) the case of complete wetting [5].

## 2.1.4 Kinetics of SSD

When looking at the stages of SSD, several factors, influencing the SSD kinetic, become obvious. At first, the overall crystallinity plays an important role for the formation of holes, but also for the propagation of hole growth. The film thickness is also highly influencing the SSD (see Formula 2 and Figure 5). It defines the overall thermodynamic landscape, but also the point at which grain boundary grooving results into holes [16]. Additionally, to the defect structure, the substrate structure and morphology can significantly influence the SSD kinetics [6]. Another factor influencing the kinetics is the process temperature, which in principle is

directly connected to the surface diffusion coefficients [6]. In addition, alloying influences the thermodynamic driving force, which is described in more detail in the upcoming section.

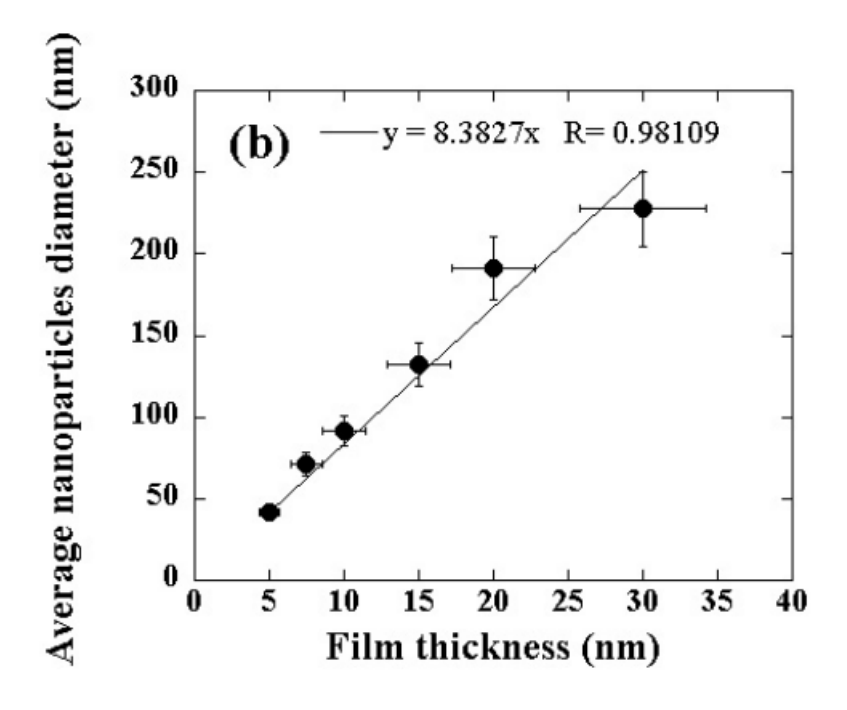


Figure 5: The graph shows that the average particle diameter is directly proportional to the initial film thickness [16].

## 2.1.5 Influence of alloying

SSD can be substantially changed via alloying. One obvious influence is the change of crystal structure and melting point by alloying. Alloying can either result in a melting point laying between that of the alloy components or even be lower, which is the case for eutectic systems [17].

Another influence on SSD can be the segregation of alloy components. In a study of Devaraj et al. [18] the grain size of an aluminium-magnesium alloy was investigated. They observed a reduced grain size at room temperature with increasing Mg content and additional to that a decrease in grain growth at elevated temperatures. This was attributed to the segregation of Mg at the grain boundaries and the formation of precipitates in the matrix, both hindering the grain growth and size [18], [19]. If a material is conducted of many small grains, the density of grain boundaries and grain boundary triple junctions are increased. Both, grain boundaries and grain boundary triple junctions act as nucleation sites for hole formation [6].

Additionally, alloy-components are able to segregate at the surface of the film or at the interface between the film and the substrate. This has quite large effects on the SSD kinetic,

even at minor alloying concentrations. In a study of Barda and Rabkin they observed a substantial decrease of SSD of Ni thin films when adding small amount of Au to the system. They observed a segregation of Au on the surface and interface of the film, which resulted in an increase of surface-anisotropy. This affected the shape and size of grain boundary grooving, making the grooves less deep and thus effectively slowing down SSD [20]. Furthermore, alloying indeed influences the surface and interface energies of the systems, which directly influences the behaviour of SSD [6], [21].

# 2.2 Liquid state dewetting

Beside the process of SSD many studies are conducted to investigate the dewetting in a molten state. This process is then called liquid state dewetting (LSD) [22], [23].

The processes occurring during LSD are fundamentally different to those happening in SSD. As already mentioned above, the crystal structure and defects of the metal are very important for SSD, but in a liquid form those kinds of sites are missing. Additionally, without a crystal structure there are no surface anisotropies and also no residual stresses inside the metal film. It is noteworthy, that the main transport mechanism in SSD is surface self-diffusion (see Section 2.1), whereas for LSD the mass transport is limited by hydrodynamics [22]–[24].

Besides all these fundamental differences, there are also similarities between SSD and LSD. Both processes will produce nanoparticles as the final result. The particle state in LSD is reached even after a few seconds of melting, whereas for SSD this process may take hours or even days [25]. The particles formed via SSD are faceted particles, showing a Winterbottom-shape. In the liquid state atoms do not form any kind of a crystal ordered structure, but even though during the solidification of the particles they form a Winterbottom-shape, as can be seen in Figure 6. This was shown for various metals, like Au on silicon carbide or Cu on sapphire [24], [25]. The precise orientation of the facets may vary between SSD and LSD, which will be covered in more detailed in section 3.1.

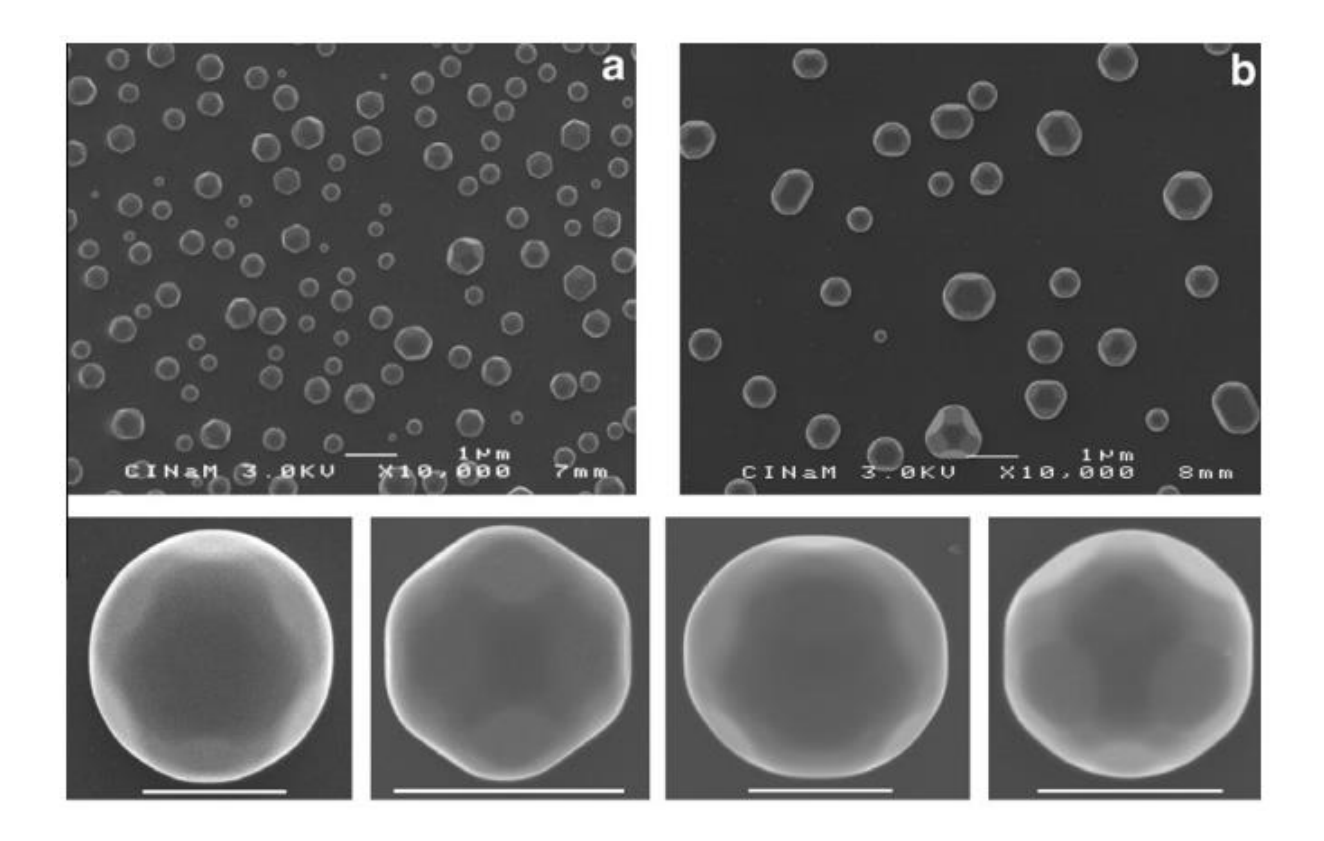


Figure 6: Copper nanoparticles formed via a) LSD and b) SSD on a single crystalline sapphire substrate. In both cases the particles form a crystal, and thereby facets, however the precise orientation of the facets varies between SSD and LSD [25].

.

# 2.3 Epitaxy of metals on ceramic

The specific orientations of the facets tell a lot about the interfacial energy. In the previous part the relation between the uppermost facet and the substrate was important. For example, in face-centered-cubic (fcc) materials, to minimize the total energy of the system the {111} directions tend to align themselves out of plane (OOP) since it is the plane with lowest surface energy [26]. However, the in-plane orientations of the particles and the substrate are also important. When growing a metal on a single crystalline substrate, epitaxy leads to an alignment of crystal directions of the particle along the substrate crystal. This is called orientation relation (OR) between the metal and the substrate. Specific ORs form to decrease the energy of the system, through the formation of low-energy interfaces. This is achieved via the lock-in of densely packed directions, as described by Fecht and Gleiter [27]. For fcc metals on a hexagonal substrate, two main ORs, OR I and OR II, are observed [28]–[30].

OR I: 
$$\{111\} \pm \langle \bar{1}10 \rangle_{fcc} ||(0001) \langle 10\bar{1}0 \rangle_{hcp}$$
 (4)

OR II: 
$$\{111\} \pm \langle 2\overline{11} \rangle_{fcc} ||(0001) \langle 10\overline{1}0 \rangle_{hcp}$$
 (5)

These ORs show twin variation, which are rotated by  $180^{\circ}$  to the original variants and indicated with  $\pm$  in Formula 4 and 5. Depending on the specific substrate and metal, the lattice parameters and thus the aligned d-spacings are not overlapping perfectly, leading to a lattice mismatch. This mismatch can be calculated via [28], [30]:

$$f_{ORI} = \frac{d_{30\overline{3}0} - d_{220}}{d_{30\overline{3}0}} \tag{6}$$

$$f_{ORII} = \frac{d_{30\overline{3}0} - d_{2\overline{1}\overline{1}}}{d_{30\overline{3}0}} \tag{7}$$

As already mentioned, LSD can change the ORs of a system. In a study of Curiotto et al. [25], they investigated the ORs of Cu on c-plane sapphire and compared SSD to LSD. They observed, that in both cases the particles form preferred ORs, however for SSD only OR I was observed, whereas in LSD beside OR I and OR II three additional ORs were present. The presence of ORs after LSD conducts the assumption, that the nucleation is heterogeneous.

# 2.4 Melting point depression of thin films

Melting point depression (MPD) of nanoparticles was observed in many instances across the literature. Atoms at the surface are weaker bound than inside the material, thus decreasing the melting point when the ratio between surface atoms to the total number of atoms increases. This was also observed for thin metal films, however some additional aspects of the system have to be taken into account [31]–[33].

#### 2.4.1 Film thickness

The melting point of metal films depends on the thickness of the film. This effect is rather similar to that of nanoparticles, and accordingly is exponentially stronger for very thin films below 10nm. In a study of Zhan et al. [33] they investigated the melting point of a thin indium film, with different thicknesses via the usage of thin-film differential scanning calorimetry. They observed a MPD of about 12 °C for a film thickness of 5.6 nm. More interestingly, as seen in Figure 7, the width of the heat capacity peak, increases when the film thickness decreases, thereby raising the question if there is a precise melting point or more a temperature range at which melting occurs [33], [34].

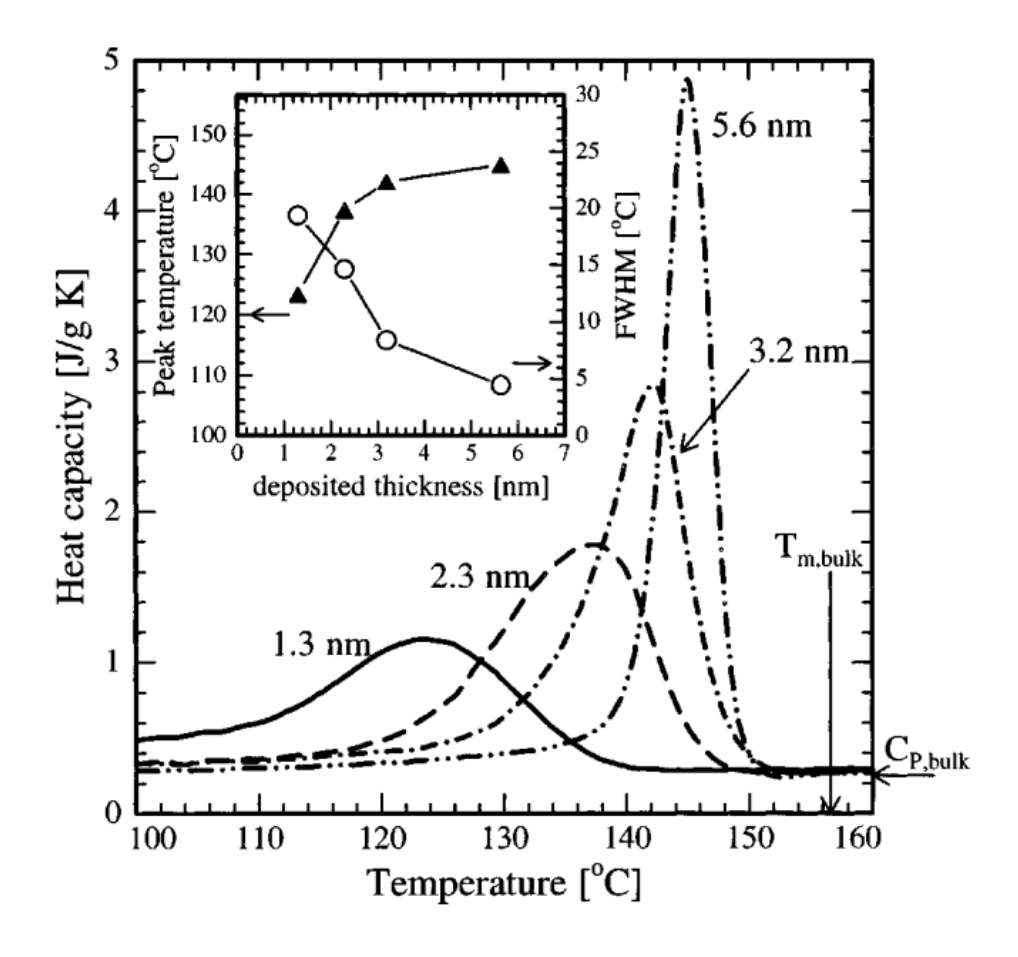


Figure 7: The melting point is described via the heat capacity of the system. The temperature where the system shows the highest heat capacity, which is needed to increase the temperature even further indicates a phase transition, in this case the transition from solid to liquid [33].

#### 2.4.2 Grain size

The melting point of thin films is not solely depending on the thickness of the film, but also on the grain size of it. In a Study of Wejrzanowski et al. [35] they simulated the melting behaviour of thin Al films with different grain sizes. Figure 8 shows how the melting point is decreased by a few hundred degrees depending on the grain size of the Al film. Additionally, they observed that melting starts at the grain boundaries and proceeds towards the centre of the grains. 2D defects (like grain boundaries) in the film can act as a nucleation side for melting thereby decreasing the melting point [35].

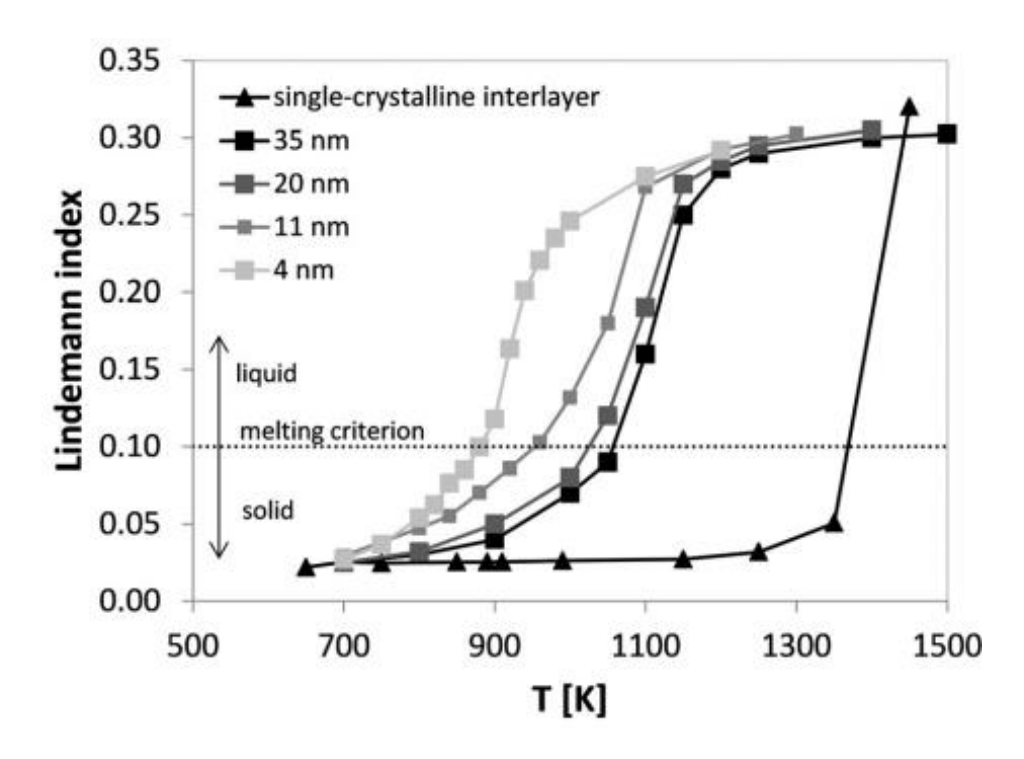


Figure 8: In the graph the Lindemann index of a thin film with different grain sizes is depicted. The Lindemann index indicates the disorder of the system. If the Lindemann index is above 0.1 the material is considered being molten [35].

# 3 Materials and Methods

# 3.1 Gold Nickel-system on $\alpha$ -Al<sub>2</sub>O<sub>3</sub>

The phase diagram of Au and Ni is shown in Figure 9. Due to the large differences in atomic radii, the AuNi system shows a miscibility gap, covering the whole concentration range at low temperatures, with a maximum at 810 °C at around 70 at%. A thermal processing above the miscibility gap, enables the formation of an fcc solid-solution, which can be maintained by quenching to room-temperature after the thermal processing. The lattice parameter of this fcc lattice evolves gradually over the concentration range. This results in a changing lattice mismatch between the alloy and the sapphire substrate. The equation (6) for OR I shows that the mismatch of the system ranges from a positive mismatch to a negative mismatch, which makes it possible to achieve a perfect lattice match at a given Au concentration.

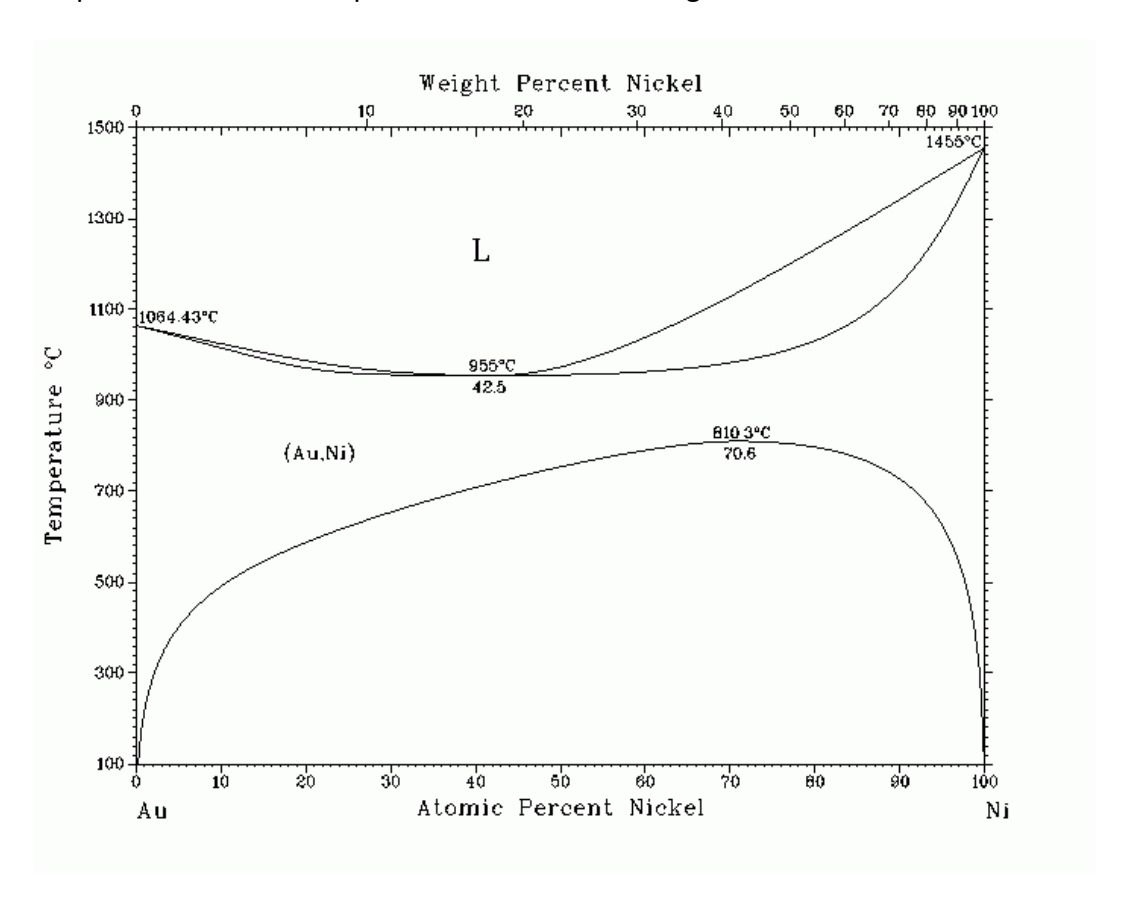


Figure 9: The phase diagram of Au and Ni [17], showing a miscibility gab over the whole concentration range.

# 3.2 Electron beam physical vapour deposition (e-beam PVD)

In research as well as industry PVD is a widely used process, which is capable of producing thin film coatings for biomedical applications, thermal barrier systems, optics and electronics.

The deposition takes place by vaporizing a target material into atoms or molecules and accelerating them onto a substrate. Therefore, a vacuum is needed, in order to prevent accelerated atoms to be stopped before deposited onto a sample. The accelerated atoms condensate onto the target material, thereby forming the film layer by layer and atom by atom. This makes PVD processes capable of producing films with a thickness ranging from a few angstroms to several µm, depending on the deposition rate and time. The deposition rate itself is dependent of several different parameters like the chamber pressure, the source of power, voltage bias, temperature, and the sputter yield of the target material. Several different PVD process do exist, which can be discriminated by the technique, which vaporizes the target material. The target material can either be evaporated or sputtered. For industrial applications PVD is of high interest, because of its low energy consumption compared to chemical vapour deposition (CVD) techniques. The process temperature is one of the main reasons for that. It lies between 750 °C and 1150 °C for CVD and between 200 °C and 600 °C for PVD techniques. Therefore, in CVD a large margin of the energy is needed to heat and cool the sample. This represents in the total energy coast for both techniques, which are 974 kWh for CVD and 112 kWh for PVD [36]-[38].

One popular evaporation technique is the e-beam PVD process and can be seen in Figure 10 a. During this process an electron beam is focused via magnetic fields onto the target, thus evaporating the target material. Via the use of an additional magnetic field the electron beam is stirred over the target, ensuring an even evaporation. The target material then condensates on the substrate material. Films produced via this technique are polycrystalline, with a small grain size, which is roughly double the film thickness [37]–[39].

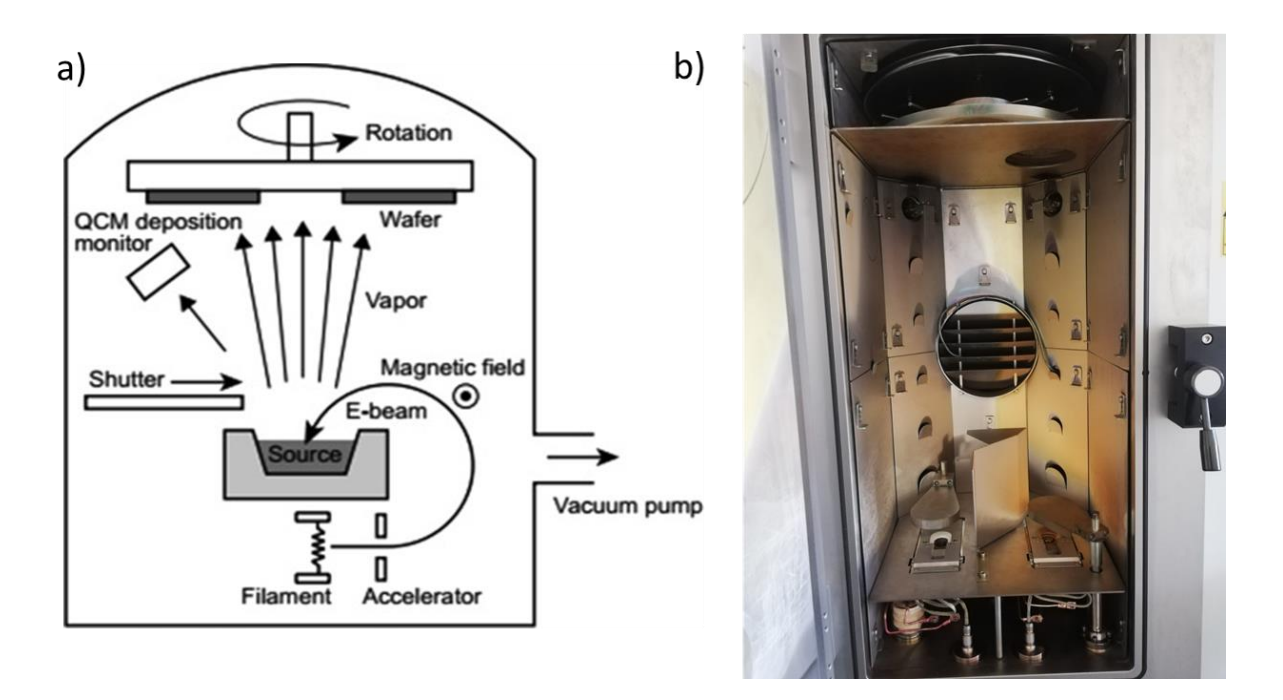


Figure 10: a) In e-beam PVD an electron beam is directed onto the source material, in order to vaporize it. Through the vaporization the atoms are accelerated in direction of the sample, which in this image is depicted as a Wafer. A quartz crystal inside the chamber tracks the deposition rate, by measuring the weight increase of the crystal. b) The PVD device used in this study is equipped with 2 individual electron guns with four crucibles on each which makes it possible to deposit multiple different materials in one process [40].

# 3.3 Scanning electron microscopy (SEM)

Scanning electron microscopy (SEM) is a powerful tool to analyse the shape and topology of nanostructures. In addition, it can extract chemical and structural information from the material. This is achieved by scanning an electron beam over the sample and analysing the radiation leaving the sample surface at every given scanning position. The acceleration voltage can range from 500 V to 30 kV [41], [42]. The SEM device used in this study is the FEI Helios NanoLab 660 Dual Beam SEM-FIB. For imaging an acceleration voltage of 5 kV was used, whereas for EDX measurements an acceleration voltage of 30 kV was applied.

#### 3.3.1 Electron beam – specimen interactions

The electron beam can interact with the sample in several certain ways depending on the sample material, shape, and acceleration voltage. The interaction happens at different depth of the specimen and can be described via the interaction volume. A typical Interaction volume is given in Figure 11. The main emission are secondary electrons (SE), backscattered electrons (BSE) and X-rays. SE are emitted via inelastic scattering events of the primary electron beam with electrons of the target material, during which enough energy is transmitted in order to remove the electron from the target material. Compared to the primary electron beam the energy transferred to the SE is rather small, resulting in a lower mean free path length compared to BSE and the primary electron beam. BSE are electrons of the primary beam which are elastically scattered in the material. The resulting stochastic direction change of the electrons path can lead to their escape out of the sample surface. Elastic scattering events reduce the energy of the incoming electrons only by a small amount. Therefore, BSE exhibit way higher energies than SE. This energy makes BSE capable of evoking SE at the positions where the BSE leave the material, as well as inside of the sample camber. These SE are called SE II and SE III, whereas SE generated at the incident position of the primary beam are classified as SE I [41], [42].

SE show manly topological information of the target material. The scattering event of BSE on the other hand strongly depend on the Z-number of the target material. Heavier elements lead to a stronger scattering of the BSE thus allowing more BSE to escape from the target material before being absorbed in the material. This allows for a material contrast when collecting BSE, which shows heavier elements brighter. This contrast can be used qualitatively to distinguish known elements in the material. If one does not know what elements the

material is made of or is interested in the precise composition, x-ray analysis is necessary. X-rays are evoked by inelastic and elastic scattering events of the primary beam. If the electron path is deflected by the core of the element, the lost energy is released in form of bremsstrahlung. This radiation is dependent on the strength of scattering, thus giving a uniform background in an x-ray spectrum. Inelastic x-ray emission happens, when the electron beam transfers enough energy to an electron of the target material, so that the electron escapes from the atom of the material. An electron of a higher shell may take the empty space afterwards. The energy difference between the two electron states is emitted as a characteristic x-ray which is unique for each element. Characteristic x-rays show peaks in the spectrum, which can be used to identify elements qualitatively as well as quantitatively [41], [42].

Figure 12 shows the dependency the interaction volume on the acceleration voltage. An increased voltage also increases the interaction voltage. This results in a worse spatial resolution when using higher voltages. However, for analytical methods, like x-ray spectroscopy the voltage has to be high enough to evoke the x-rays.

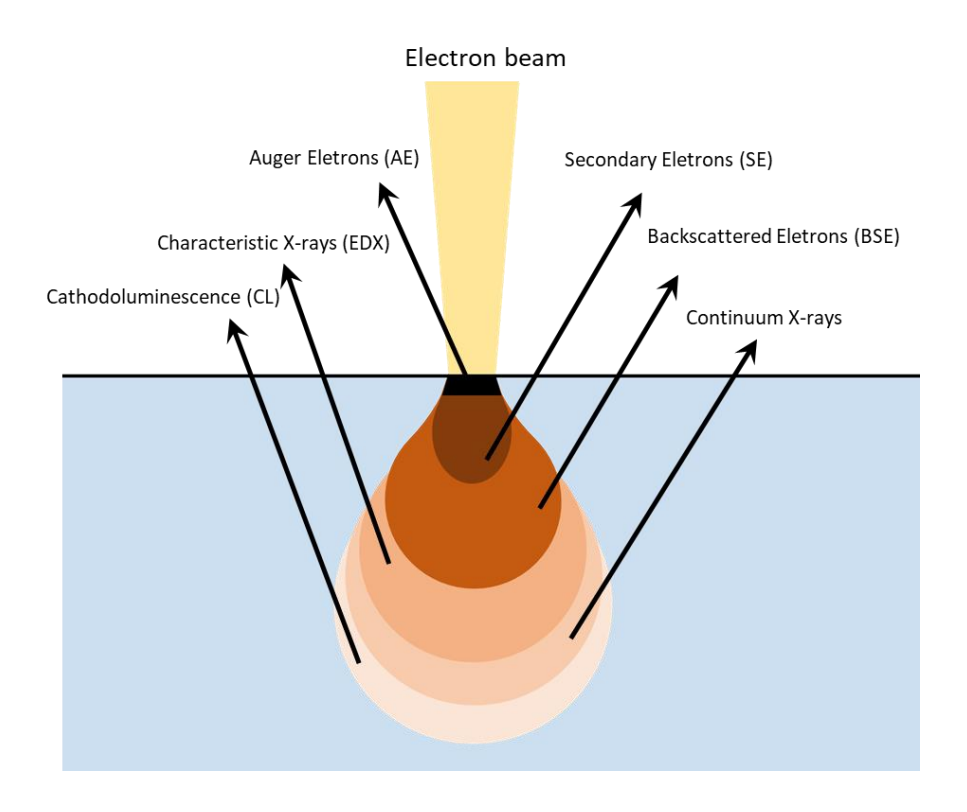


Figure 11: The interaction volume resembles the volume of the material in which the electron beam evokes a multitude of different radiations from the target material. The energetically higher radiations are capable of being generated deeper in the material, thus reducing the special resolution of energetically higher radiations. Image adapted from [43].

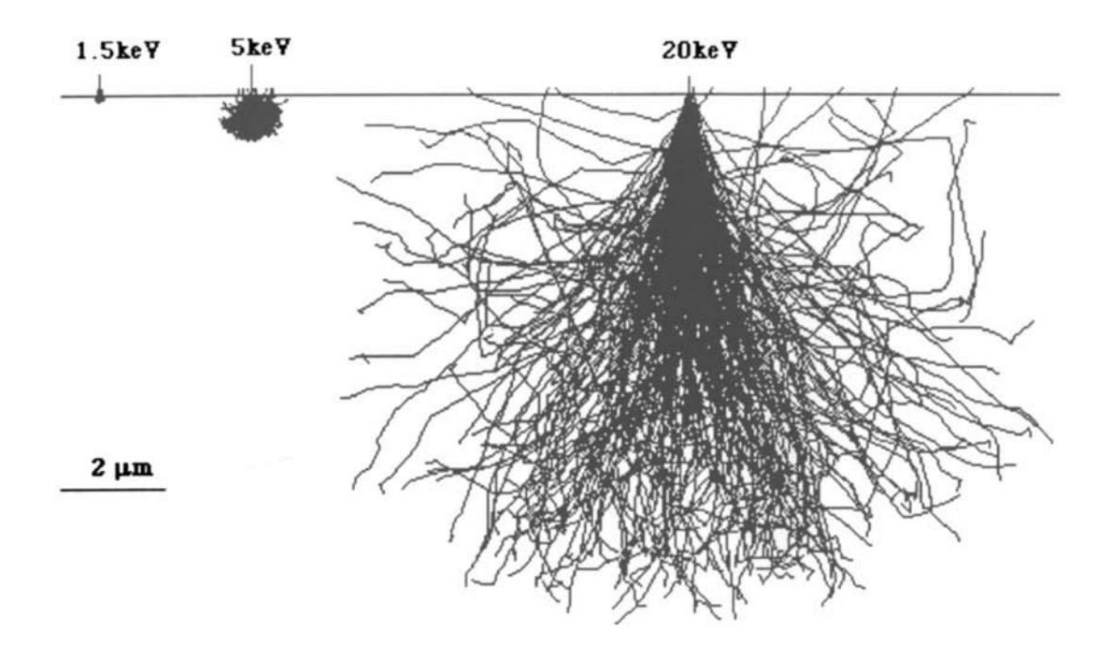


Figure 12: Monte carlo simulations of the electron path at different acceleration voltages show, that the interaction volume increases substantial with higher voltages. This influences the resolution of SEM. In high resolution SEM low voltages are used to localize the information and increase the resolution [42].

#### 3.3.2 Electron backscatter diffraction (EBSD)

EBSD is a technique which is implemented in the SEM for investigating crystallinity and grain orientation. A schematic representation of the measuring setup is depicted in Figure 13. For this technique the sample has to be mounted 60 ° to 70 ° relative towards the electron beam. The angle increases the amount of electrons which are backscatter from the sample. After penetrating the sample, the electrons are diffusely scattered. Some of these electrons can then fulfil the Bragg condition in accordance to the crystal planes of the sample and afterwards exit the sample when they are close to the surface, without further scattering. The BSE are then distributed in Kossel cones which intersect with the detector and then form a pattern. This pattern shows Kikuchi lines similar to TEM scattering techniques. In a conventional diffraction pattern the position of each diffraction spot does not change when the crystal is rotating. Kikuchi lines however move respective to the crystal orientation. This makes it possible to identify the local crystal orientation by analysing the Kikuchi pattern of the scanning position. The Kikuchi lines show which crystal orientation is oriented normally to the EBSD detector [44]–[47].

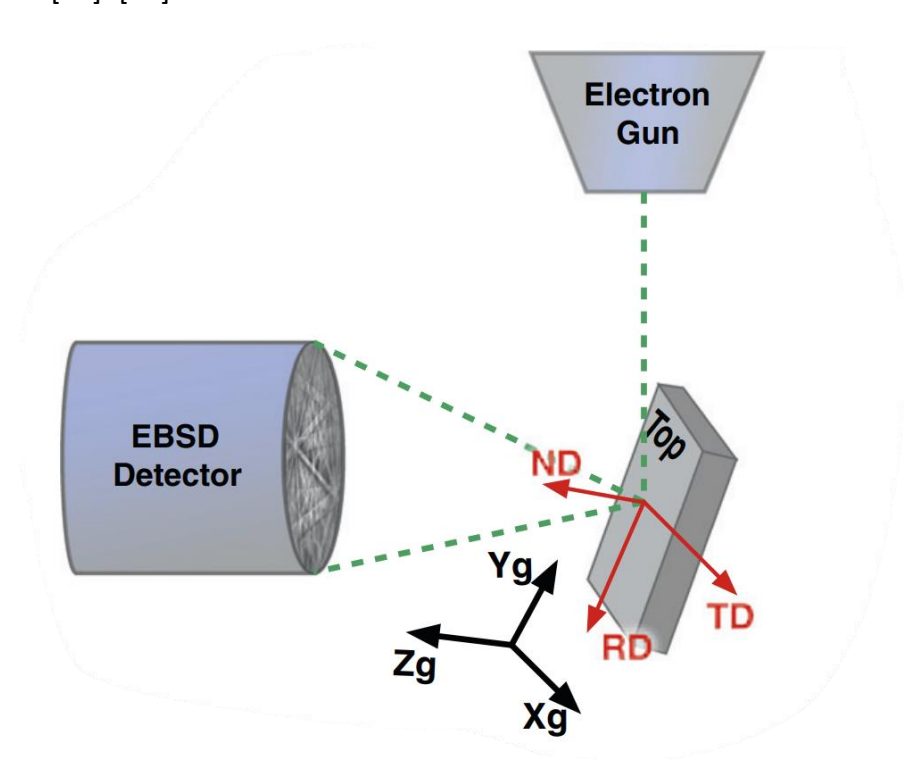


Figure 13: When measuring EBSD the sample should be mounted 60° to 70° relative to the electron beam. This increases the BSE yield and thereby the quality of the EBSD patterns. To analyse the crystal orientation, one must take this tilt angle into account[48].

#### 3.3.2.1 Indexing EBSD data

The acquired data from EBSD measurements now consists of multitude of different Kikuchi pattern. To identify the local crystal orientation these EBSD patterns have to be analysed. In the past this was achieved manually. Analysing EBSD data manually is rather slow and was replaced by the Hough indexing (HI) method in the early 1990s. HI relies on the Hough transform, which is a technique of identifying complex patterns of image points, by reducing the information necessary from a global detection problem down to a peak detection problem. This is done by converting the EBSD patterns into the Hough space, using the following equation:

$$\rho = x \cos \theta + y \sin \theta \tag{8}$$

, where x and y are two points in the diffraction pattern and  $\rho$  and  $\theta$  are the corresponding coordinates in Hough space. Through this transformation straight lines are converted into maxima (points) in the Hough space. The maxima in Hough space are now mathematically easy to identify and vice versa now also straight features like Kikuchi bands in the EBSD pattern. This makes it possible to identify and index the Kikuchi bands in the EBSD patterns. The position of the Kikuchi bands in the EBSD pattern will now be compared to EBSD measurements from literature to identify the orientation of the measured grain. Figure 14 depicts this workflow for one exemplary EBSD patterns of silicon [49].

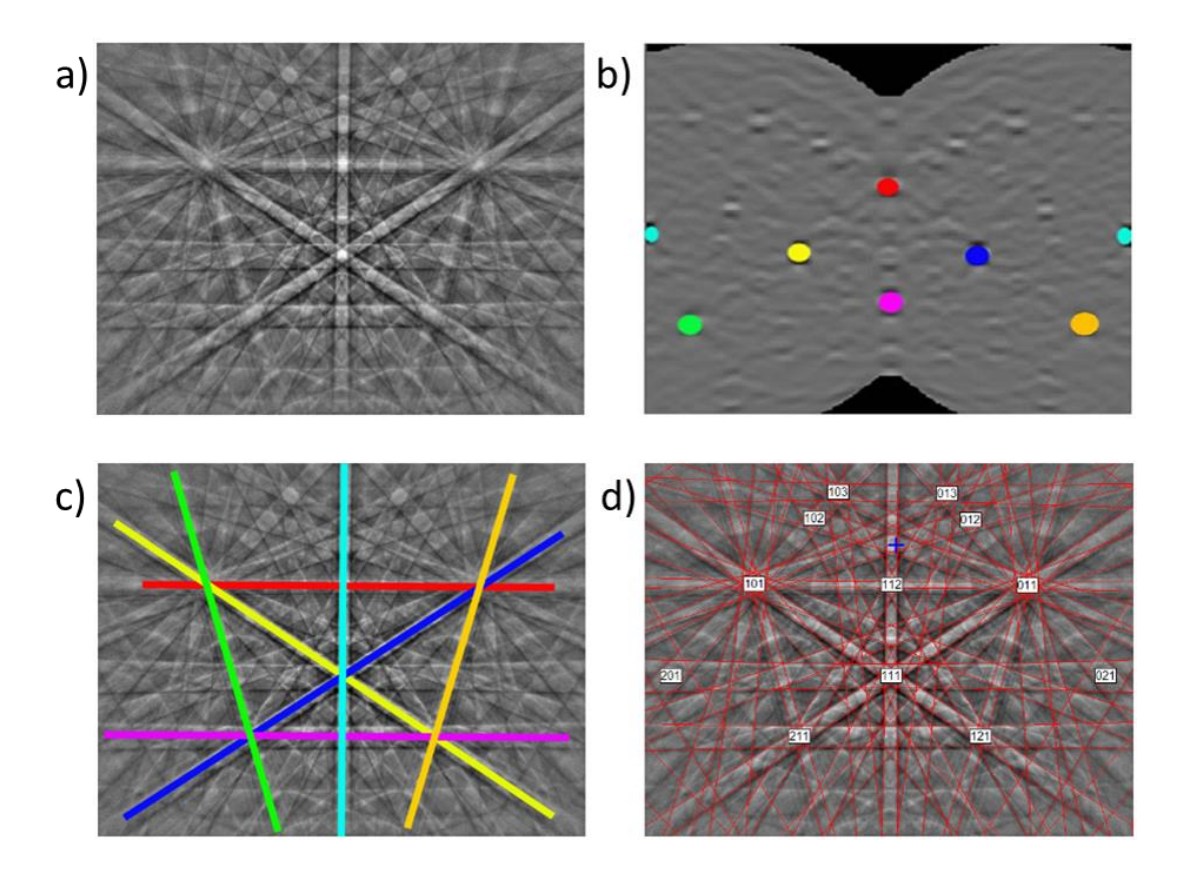


Figure 14: The image in b) shows the Hough transform of the EBSD pattern in image a). The maxima in the Hough space in b) are corresponding to the coloured lines in c). From theses straight lines the Kikuchi lines are reconstructed and indexed (d). Image adapted from [50].

## 3.3.2.2 Pole figures

Pole figures are a way of depicting the orientation of grains graphically. Figure 15 shows the principle of pole figure construction. To do so, one must project the 3-dimensional EBSD data into a 2-dimensional pole figure. This is done via the use of the isogonic stereographic projection [51]. For this technique a unit sphere is constructed around the crystal. Each crystal plane has a normal vector that will now intersect at some point with the unit sphere. The intersection is described via two angles ( $\psi$ , $\varphi$ ) and Figure 15 a) shows schematically how the angles are constructed. This line is afterwards connected to the south pole of the unit sphere, giving another straight line that will intersect the horizontal cantered plane of the unit cell at the coordinates x and y. These coordinates give now the position of a measured point in the pole figure. The projection works via the formula 8 and 9:

$$x = \frac{\sin \psi \cos \varphi}{1 + \cos \psi} \tag{9}$$

$$y = \frac{\sin \psi \sin \varphi}{1 + \cos \psi} \tag{10}$$

Pole figures can be plotted via heat maps, showing the mean uniform density (MUD) of the data points (preferred orientation has high density as shown in Figure 15 b), or the scattered data is shown, where each individual measuring point is depicted in the pole figure (see Figure 15 c) [51].

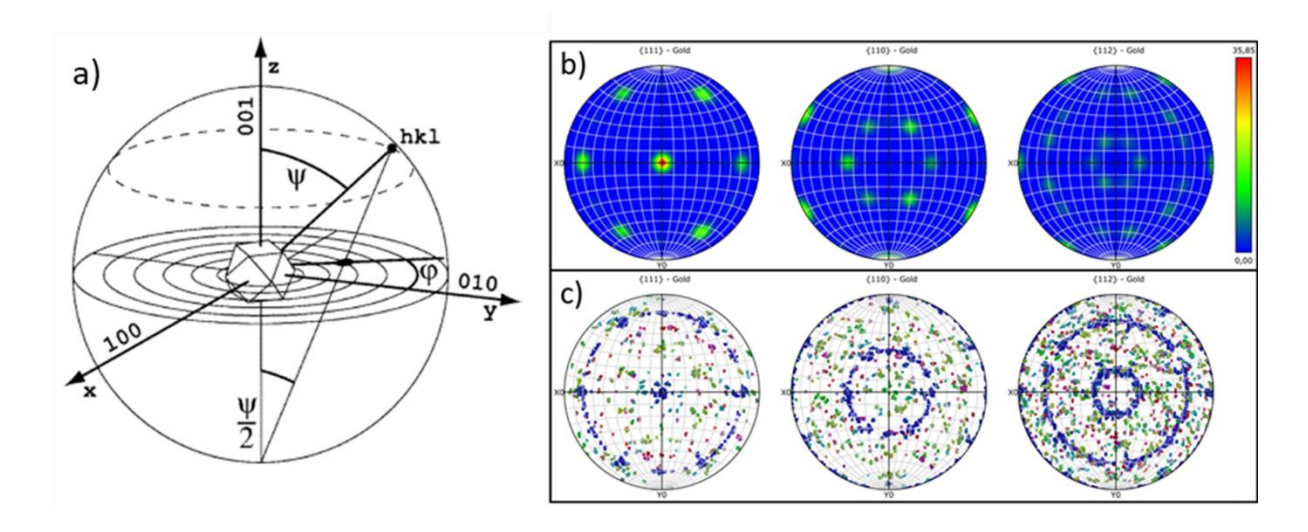


Figure 15: The left image a) depicts the procedure of transferring a 3D-crystal orientations into a 2D pole figure (b/c). The intersections of the crystal directions with the unit sphere are projected onto the respective plane of the pole figure, thus giving a measured point [51].

#### 3.4 Focused ion beam

Besides the regular electron beam inside a SEM device the use of a focused ion beam (FIB) can be helpful as well. The FIB is a versatile tool to either image, mil, or deposit. In most cases the ions used are positively charged gallium ions (Ga+), but recently less heavy helium ions are getting more and more use [52].

Similar to the electrons in SEM, the interaction of the ion beam with the target material produces secondary particles like atoms, ions, and electrons. These particles can be collected and analysed, similar to the imaging technique of the SEM. However, due to the potential of damaging the sample with the FIB imaging with ions plays only a minor role in applications [52]. The main applications are ion beam induced milling and the deposition of materials, which will be explained in the following.

The principle of FIB milling is shown in Figure 16 a). The milling process relies on physical sputtering, where the etching rate is dependent on the ion beam current. By milling the sample, complex nanostructures can be created in the target material or lift outs for later transmission electron microscopy analysis can be produced. Especially for such applications the damage depth of the ion beam has to be taken into account. While getting closer and closer to the region of interest the acceleration voltage should be reduced in order to reduce the damage at the area. Additionally, the sputtered material can re-deposited next to the area of milling. It is therefore of advantage to mill towards the region of interest, because redisposition is located behind the scanning direction [52].

Most FIB devices are additionally equipped with a gas injection nozzle. This makes it possible to not only sputter material away, but also to deposit material (see Figure 16 b). The process is a chemical vapour deposition process. This means that a gaseous precursor needs to be injected onto the area, where deposition is wanted. The gaseous species will adsorb at the surface of the sample and then ion-beam needs to be focused onto the sample. This will break down the precursor into the desired species for deposition and other highly volatile reaction products. Those highly volatile products will evaporate and leaves the system through the vacuum system, whereas the desired species will deposit on the surface. The newly formed layers most likely will contain impurities, either from the precursor or from the ion-beam itself. Typical elements for deposition are metals like platinum and tungsten, but also carbon is very common [52].

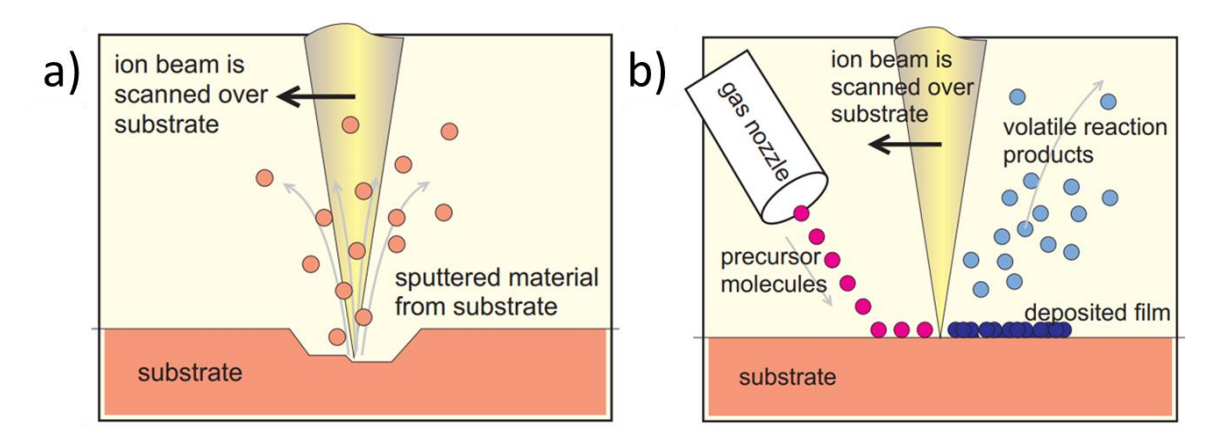


Figure 16: The main techniques which a FIB device is capable of are a) milling and b) deposition. For a) milling the heavy  $Ga^+$  ions are accelerated to higher voltages as for imaging, which leads to the removal of material from the targets surface. Via the injection of a precursor gas b) deposition can be achieved instead of milling. The image is adapted from [52].

# 3.5 Scanning transmission electron microscopy (STEM)

STEM can be conducted in a dedicated device or as an additional image acquisition mode in conventional transmission electron microscopes (CTEM). Except from the direction the electrons travel (upwards or downwards), the beam path for STEM in a dedicated device is nearly equivalent to that of CTEM. In both cases the electrons transmit trough the sample and the detectors lay behind, which means that the sample has to be thin enough to be electron transmissible or as a rule of thumb thinner than 100 nm. In CTEM the sample is illuminated in parallel beam optics (see Figure 17 b). This results in complex image artefacts from scattering, like for example lattice fringes. In STEM mode the electron beam is focused on one small spot and scanned over the sample (see Figure 17 a). This removes image artefact from scattering and makes the images easier for interpretation, when compared to CTEM images. However, to get a decent magnification with STEM, the beam probe needs to be as small as possible. Therefore, lens aberrations need to be eradicated or reduced as low as possible [53].

Also, the detectors vary between CTEM and STEM. In STEM the detectors are arranged at different angles towards the electron beam probe, which makes it possible to inherited different contrast for one image. For the bright field (BF) detector the angles measured are smaller than the semi convergent angle of the focused electron beam, thus as a result mainly measuring transmitted electrons of the primary electron beam, which did not undergo scattering. The annular dark field (ADF) and high angle annular dark field (HAADF) detectors measure electrons at higher angles than the semi convergent angle. Between BF and ADF the contrast is mostly inverted, like conventional bright field and dark field imaging. The HAADF detector on the other hand detects electrons which are very strongly scattered. Such a strong scattering results from interactions of the electrons directly with the atom core of the sample. The degree of scattering thus strongly depends on the atomic mass (Z-number) of the element, which means that the HAADF contrast inherits information about the chemical structure of the sample. The brighter areas appear in HAADF contrast, the heavier the element in that area [53], [54].

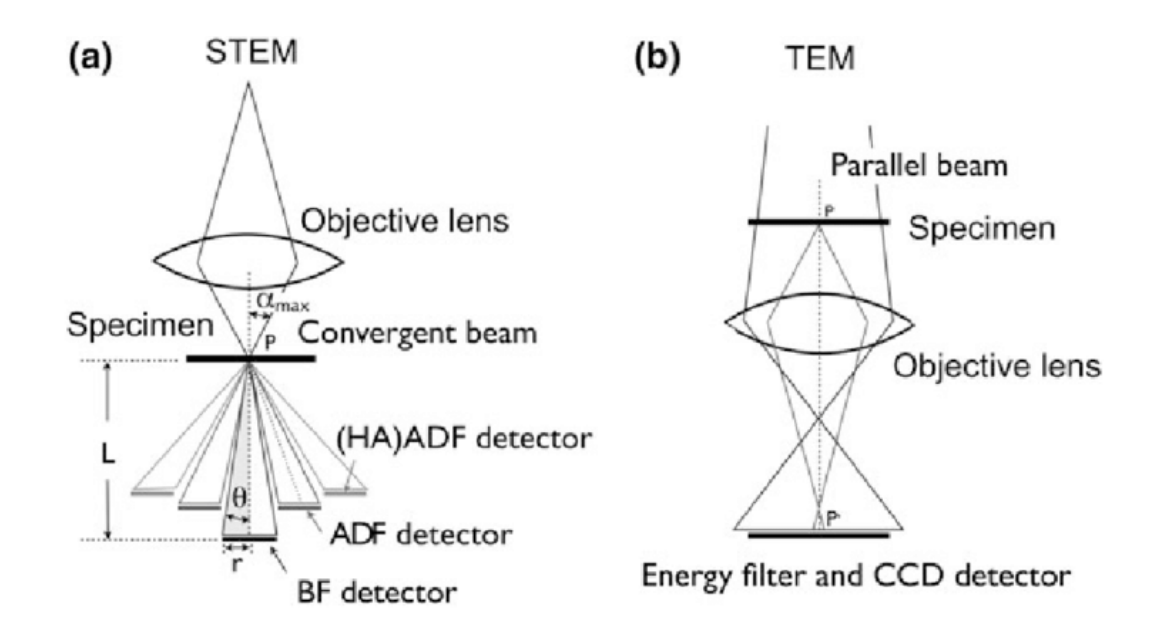


Figure 17: The acquisition of a) STEM imaging and b) TEM imaging mostly differs in the illumination of the sample and detectors. For TEM the sample is illuminated in a parallel beam, whereas for STEM the electron beam is focused onto a small spot and then scanned over the sample. In STEM imaging several more detectors are used at different angles towards the sample. The BF detectors detects electrons at angles lower than the semi convergent angle of the beam, whereas the ADF and HAADF detector detects electrons at higher angles [54].

# 3.6 X-ray diffraction (XRD)

X-ray diffraction (XRD) is a common technique to identify the crystallinity of a material. In XRD an X-ray beam is pointed onto the sample under a specific incident angle and a detector is placed at the same angle respective to the samples horizontal. At angles of constructive Bragg diffraction, intensity is measured at the detector. The Bragg diffraction is defined as:

$$2d_{hkl}\sin\theta_{hkl} = \lambda \tag{11}$$

where  $d_{hkl}$  is the lattice spacing of the planes with the indices h, k and l,  $\theta$  is the incident angle of the x-ray beam and  $\lambda$  the wavelength of the x-ray beam [55].

If the angle does not fulfil the Bragg condition the interference will be destructive, thus leading to an intensity drop at the detector. By scanning now over different angles between source and detector towards the sample the angles at which constructive interference takes place can be used to identify the targets crystal structure and crystal orientation. [55], [56].

The peak position and intensity can be used to analyse the sample in more detail. In general, the peak intensity depends on the initial intensity of the source, the structure factor of the element and the percentage of crystals oriented in Bragg condition. The peak position is mainly influenced by the distance between planes, which have evoked the peak in the first place. Depending on the overall crystal structure the lattice parameters of the crystal can be calculated from the peak position, however the precise formula is dependent on the geometric shape of one unit cell. The lattice parameter a can be calculated by using any appearing (hkl) reflection and firstly calculating the distance  $d_{hkl}$  between those planes, as shown in Formula (11). From that the lattice parameter can be calculated via the formula:

$$\frac{1}{d_{hkl}^2} = \frac{h^2 + k^2 + l^2}{a^2} \tag{12}$$

Formula (12) is only applicable for a cubic crystal. Other crystal systems like tetragonal or orthorhombic crystals have different formulas, due to the difference geometric factors of the crystals systems [55].

As already mentioned, the peak intensity does scale with the structure factor  $F_{hkl}$  of the material. The structure factor is calculated with the following formula:

$$F_{hkl} = \sum_{i=1}^{N} f_i(\theta_{hkl}) \exp(-2\pi i [hx_i + ky_i + lz_i])$$
(13)

, where  $f_i(\theta_{hkl})$  is the scattering amplitude of the respective atom in a unit cell with i amounts of atoms.  $f_i(\theta_{hkl})$  is dependent on the angle of scattering and decrease with higher angles, but also is highly dependent on the Z-number of the atom and increases with increasing weight of the atoms [57], [58].

# 3.7 Basics of combinatorial material investigations

Combinatorial approaches are used to greatly enhance the process of material discovery and investigation. During the process, a library of many different material compositions or preparation properties is produced in one single experiment. This assures that the conditions are the same. Candidate materials are selected by characterizing the entire material library. This process can then be repeated, with smaller increments around the candidate materials or if the properties are optimised enough, the process is stopped. Figure 18 shows a schematic of a combinatorial investigation of semiconductor materials [59], [60].

In some cases, it is of advantage to use a gradient instead of discrete compositions. A gradient structured sample makes it possible to cover nearly the whole concentration range with one single sample. Apart from the optimization of alloys, this makes it possible to investigate a specific concentration, which is sometimes hard to achieve with a conventional sample. This for example is of great interest, when investigating the OR of metals on ceramics. Via the usage of a gradient sample the precise point of lattice match can be achieved. A gradient structured sample can be produced with any sort of directional deposition process and the usage of a movable shutters during the deposition process. By rotation of the sample about 180° binary systems can be produced, whereas for ternary systems the sample has to be rotated 120° between every deposition step. Afterwards the samples need to undergo a thermal treatment to achieve an alloy. In the case of SSD the heating step is not necessary before conducting the experiment. It is also possible to produce already mixed gradient samples, by co-deposition. The concentration range of co-deposited samples at room temperature is roughly 20-80 at% [59]–[63].

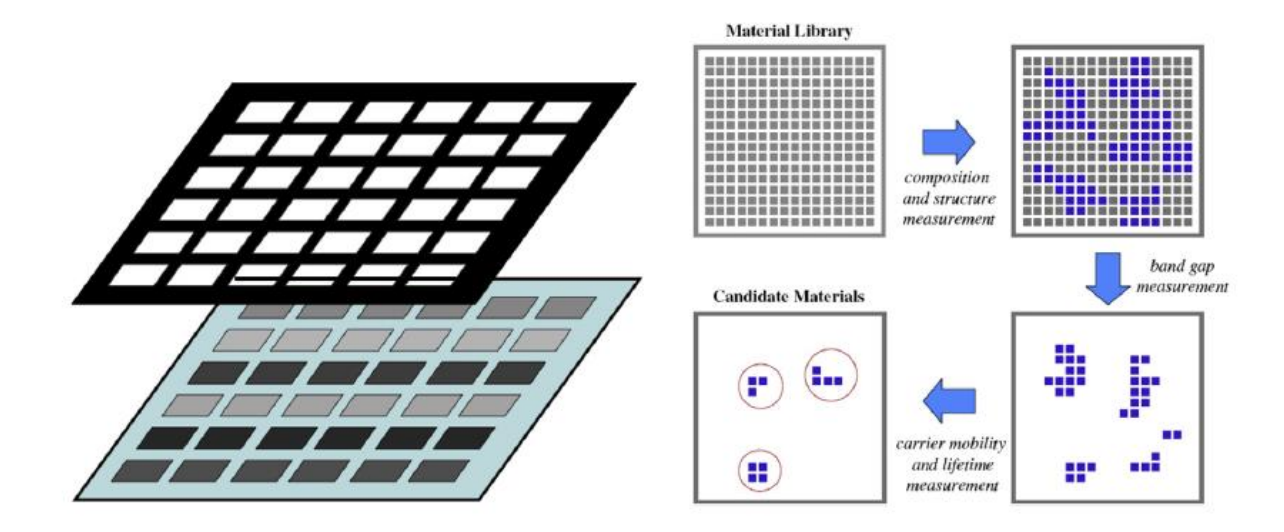


Figure 18: Schematic representation how a combinatorial library of different compositions can be created. In this example, an array of semiconductors with different compositions is first tested for their bandwidths and then for carrier mobility and lifetime. After each measurement candidate compositions are chosen, leaving only a few left for more detailed investigations [63].

## 3.8 Sample preparation and analysis

#### 3.8.1 Precleaning procedure

Before performing E-Beam PVD, the single crystalline sapphire substrates (miscut of < 0.25 °, one side polished, 5x5 mm, thickness of 500  $\mu$ m, CrysTec Kristalltechnologie Berlin, Germany) undergo several cleaning steps. The substrates are emerged in acetone (VWR CHEMICALS, purity  $\geq$  99 %) and put in an ultrasonic bath (Sonorex Super RK 31, BANDELIN electronic GmbH & Co. KG Berlin, Germany) for 5 min. Afterwards the polished surface of the substrates is cleaned via a cotton bud in an acetone, isopropanol (VWR CHEMICALS, purity  $\geq$  98 %) and ethanol (VWR CHEMICALS, purity  $\geq$  96 %) bath and dried with Nitrogen gas. Residuals of the solvents are removed via plasma cleaning (NanoClean Model 1070, Fischione Instruments Inc., Pennsylvania) with an Argon-Oxygen gas mixture for 5 min.

#### 3.8.2 Deposition process

Bilayers of Au (99.9 % ESG, Germany) and Ni (99.9 % Evochem, Germany) were deposited on the just cleaned substrates via electron beam evaporation (HVB 130, Winter Vakuumtechnik, Germany) (see Figure 10 b) with a deposition rate of 0.5 Å/s. The deposition rate was measured during the process using an osculation quartz. The samples were mounted onto a self-build holder, which masks the samples. The holder is capable of moving with a constant speed, thus allowing to subsequently uncover the sample during the deposition process. This results in a gradient sample structure of the deposited material. Firstly, 40 nm Ni are deposited on the substrates with the holder moving during the process, followed by a deposition of 40 nm Au, while the holder moves in the opposite direction. The schematic sample structure is shown in Figure 19.



Figure 19: The gradient samples possess a concentration gradient of Au and Ni, while having a constant concentration perpendicular to the gradient and a constant thickness of 40nm throughout the whole sample.

#### 3.8.3 Heating of samples

After the deposition process, samples are transferred to a rapid thermal annealing (RTA) furnace (AS One RTP, ANNEALSYS Montpellier, France). For the thermal treatment, a heating ramp of 100 °C/s is used and at the end the samples are quenched after their respective heating time to prevent de-alloying of the AuNi system. In this study the processing temperature and time was varied for different samples to investigate their influence on the film morphology and texture. Table 1 shows and overview over all produced samples. The last sample - the 2step sample - in the list was heated at two different temperatures. Firstly at 1000 °C for 30 s and afterwards cooled down, with a cooling ramp of 1 °C/s, to 850 °C. The temperature of 850 °C was held for 180 s before quenching the sample.

Table 1: Heating temperatures and times of all samples used in this study.

| Sample name  | Temperature / °C | Time / s |
|--------------|------------------|----------|
| 875C 120s    | 875              | 120      |
| 875C 3600s   | 875              | 3600     |
| 900C 120s    | 900              | 120      |
| 910C 120s    | 910              | 120      |
| 920C 120s    | 920              | 120      |
| 1000C 30s    | 1000             | 30       |
| 2step sample | 1000             | 30       |
| •            | 850              | 180      |

### 4 Results

### 4.1 Proof of concept

To proof the concentration range of the deposited samples, EDX measurements were done on an unheated sample. One measurement was performed in direction of the gradient, as well as three measurements perpendicular to the gradient. Figure 20 shows, that the Au concentration subsequently increases along the gradient ranging from 0 to 100 at% Au (orange line). It appears, that at lower Ni concentrations the Ni concentration increases slower than compared to the increase in Au concentration on the other side. The reason for that might be, that the Au layer is deposited on top of the Ni layer, thus leading to a screening effect of the Au layer onto the Ni layer and therefore, an underrepresentation of the Ni signal. For heated samples the layers have intermixed and formed an alloy, and so the underrepresentation of the Ni signal should not be relevant anymore. Furthermore, the concentration stays constant perpendicular to the gradient direction at all three measured regions (see Figure 20 green, red, and blue lines). This makes it possible to increase the amount of statistical information by making multiple measurement above each other, which than will be at a location of similar concentrations.

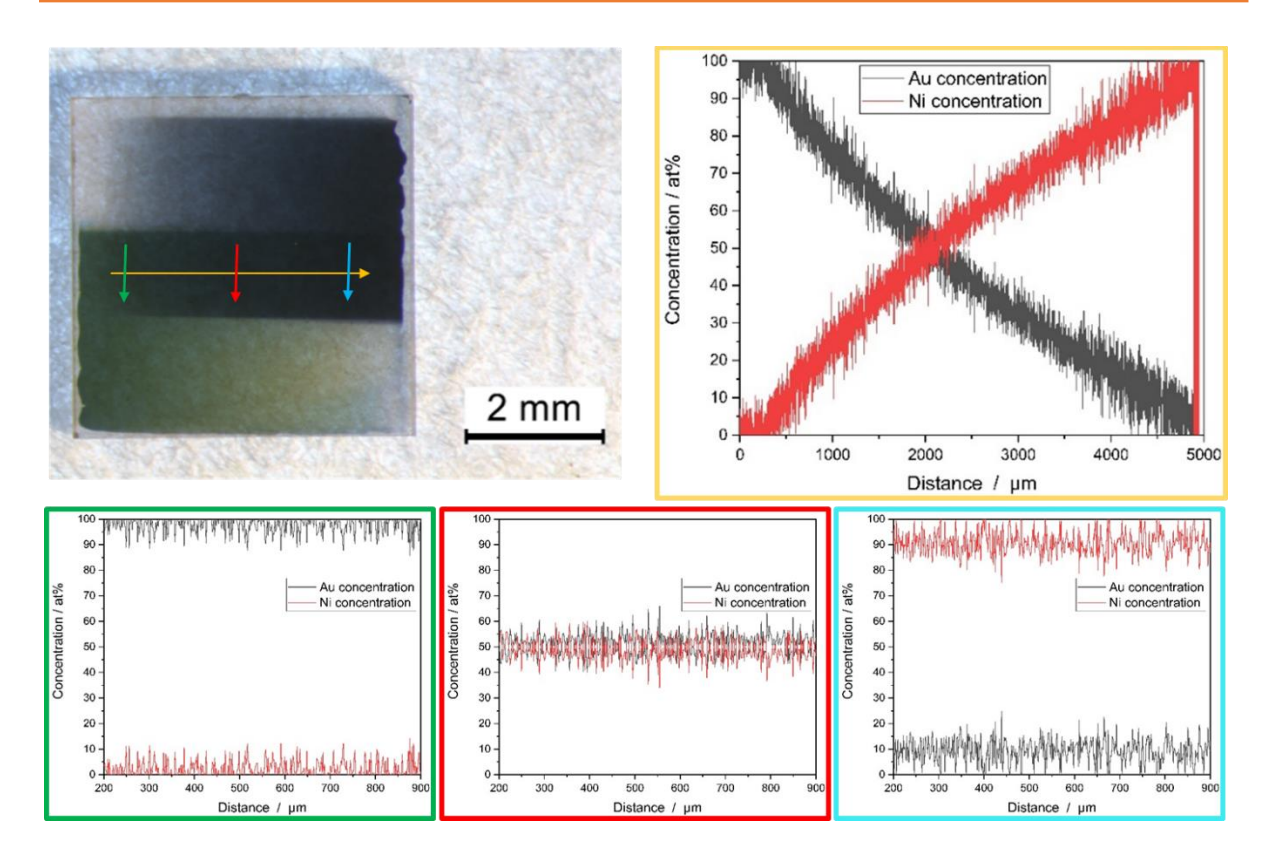


Figure 20: Four EDX measurements of an unheated sample were conducted. The colours of the scanning area and direction shown on the sample correspond to the outlines surrounding the graphs. In direction of the gradient the EDX graphs shows a constant and gradual increases of Ni and a subsequent decrease of Au from left to right. Additionally at all three measurements perpendicular to the gradient the concentration stays constant.

In addition, a cross section of one unheated sample was performed and analysed via STEM, to ensure the thickness of the samples, as well as the distribution of the Au and Ni layers. Figure 21 shows, that the total film thickness of an unheated sample is  $40.1 \text{ nm} \pm 1.4 \text{ nm}$ , which is a typical roughness for PVD prepared thin metal films [37]. As intended the Au layer lays on top of the Ni film.

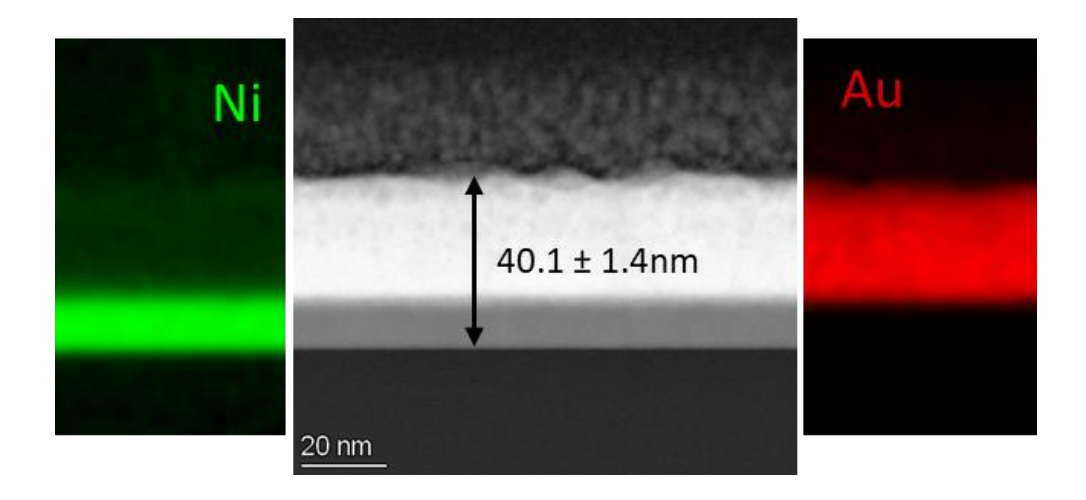


Figure 21: A STEM cross section of an unheated sample shows, that a total film thickness of around 40 nm was achieved. The Au and Ni layer are well separated before heating the samples.

To ensure that after quenching no de-alloying takes place, local XRD measurements with a beam slit of 0.5 mm, were conducted. The Graph in Figure 22 shows the {111} peak of the alloy at 10 different positions on the sample. The concentration values were calculated by using the position of the peaks and formula (12) to firstly calculate the lattice parameter. The resulting calculated lattice parameters were then compared to values from the literature (see Figure A1). With increasing Au concentration, the peak shifts towards lower angles, as a result of an increasing lattice parameter with higher Au concentrations [64]. In the case of dealloying the {111} peak would split up into the two peaks of Au and Ni at the positions corresponding to their respective lattice parameter. Because in this study the peaks do not split up, no de-alloying is happening during the heating processes. Additionally, the peak height increases towards higher Au concentrations.

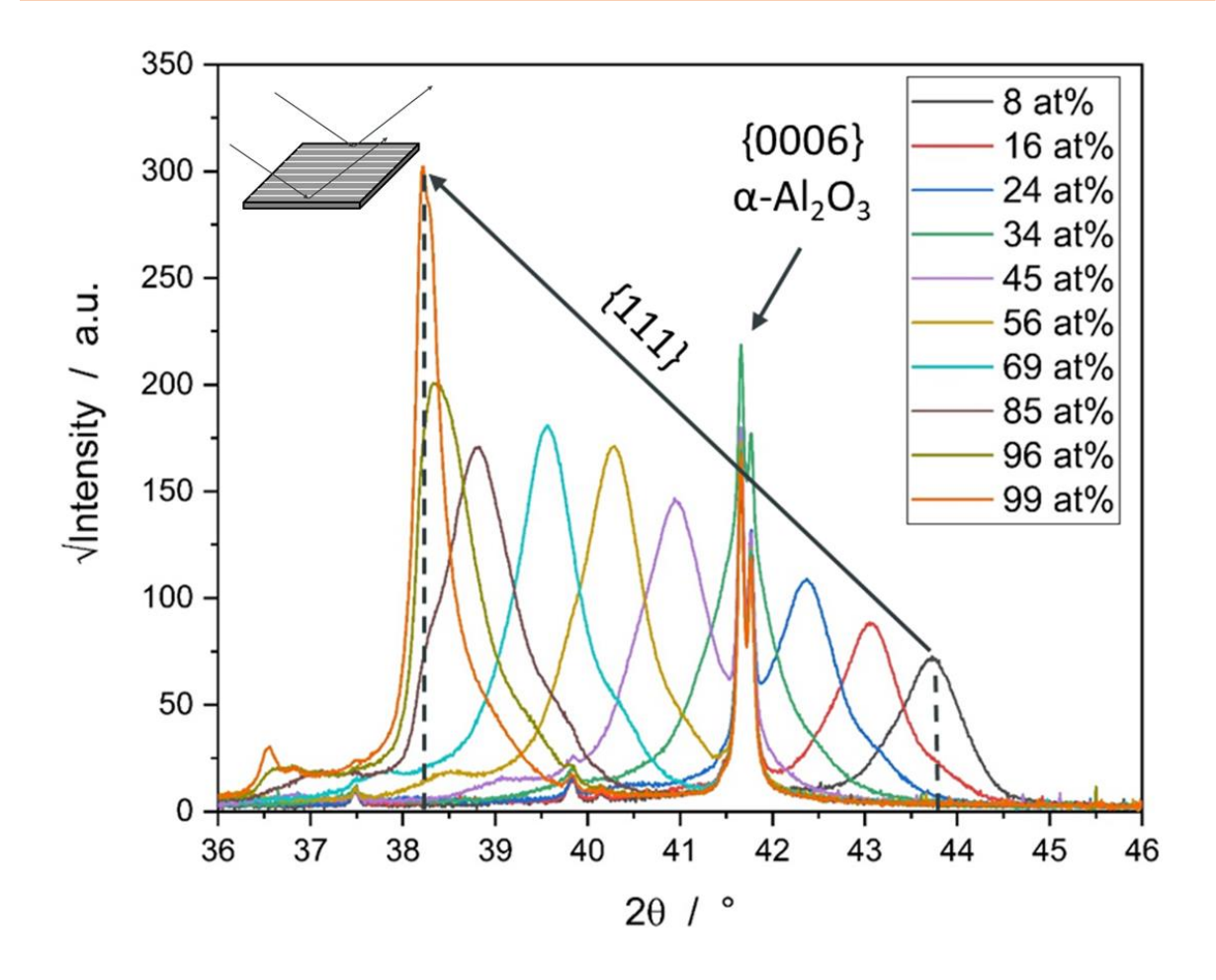


Figure 22: In XRD measurements of a heated sample a peak shift alongside an increase in peak height with increasing Au concentration can be observed. This can be explained by the increasing amount of Au, which on the one hand causes an increasing lattice parameter, and on the other hand is a strong scattering element. This behaviour shows that there is just one crystal structure of Au and Ni present, thereby no de-alloying is taking place.

### 4.2 Process-Time variation at 875°C

To investigate the influence of time on the SSD behaviour of AuNi thin gradient films, two samples were heated at 875 °C, one for 120 s and one for 3600 s. The graphs in Figure 23 show the exposed over unexposed area (a), particle density (b), equivalent circle diameter (ECD) (c) and circularity (d) of the two different samples. At 10 at% the exposed over unexposed area ratio of both samples is relatively high around 7, while the ECD is low at roughly 0.35 μm. This suggests a very far dewetted state of the samples, which is proven by SEM images in Figure 24. At this Au concentration round, slightly elongated particles can be observed with no significant difference between heating times of 120 s and 3600 s. With increasing Au concentration, the exposed over unexposed area begins to decrease. This happens between 10 at% and roughly 35 at% and goes along with an increase of the ECD, suggesting now a slowdown of SSD in that concentration range. After 35 at% the exposed over unexposed area is increasing until 75 at% for both samples, whereas after 75 at% only the exposed over unexposed area of the 3600 s sample keeps increasing. The exposed over unexposed are of the 120 s sample now decreases, indicating a deviation between the SSD of both samples at this point.

When only considering the exposed over unexposed area, particle density, and ECD both samples behave rather similar in the concentration range between 10 at% and roughly 75 at%, however the circularity starts to deviate between both samples after 20 at%. The SEM images (see Figure 24) show, that after 20 at% the 3600 s sample shows round, slightly elongated particles, with just minor changes on particle morphology when compared to the SEM image taken at 8 at%. After 120 s on the other hand, elongated finger-like structures start to appear at 22 at% and at 52 at% the morphology is dominated by those finger-like, elongated structures. At even higher concentrations the SEM images reveal, that along the elongated structures even some areas appear where there is still some film visible. The exposed over unexposed area ratio in that region starts to deviate from the 3600 s sample, thereby representing the change in morphology.

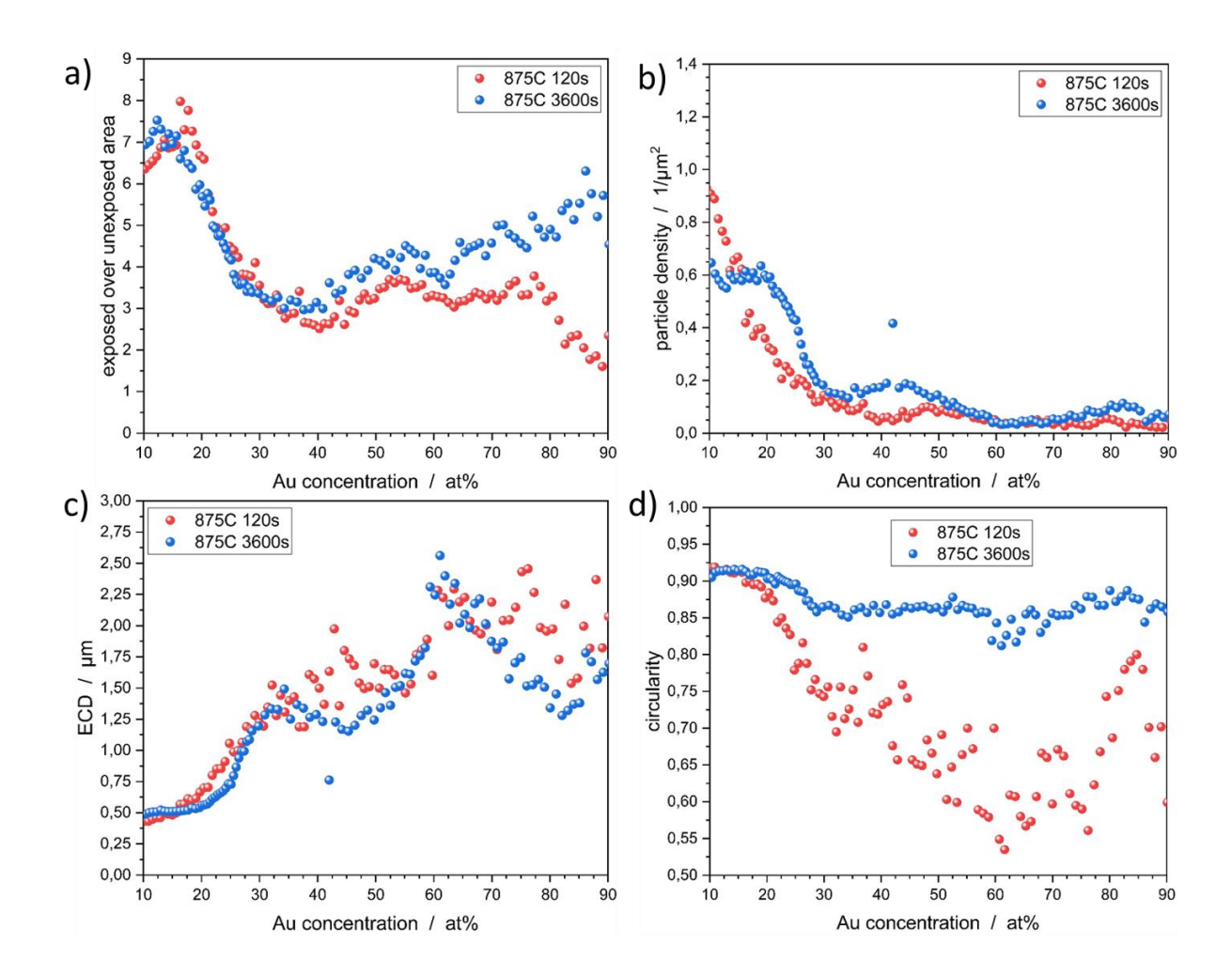


Figure 23: Between 10 at% to 35 at% the a) exposed over unexposed area and b) particle density decreases whilst the c) ECD increases, suggesting a slowdown in SSD. Between 35 at% to 75 at% the trend reverses and now the exposed over unexposed area is increasing, while the increase in ECD starts to slow down. Comparing the SSD behaviour of samples heated up for 120 s and 3600 s show only slight differences. The a) exposed over unexposed area, b) particle density and c) ECD suggest no large difference between the two samples however, the d) circularity shows a vast change after 20 at%. This can be verified via SEM images.

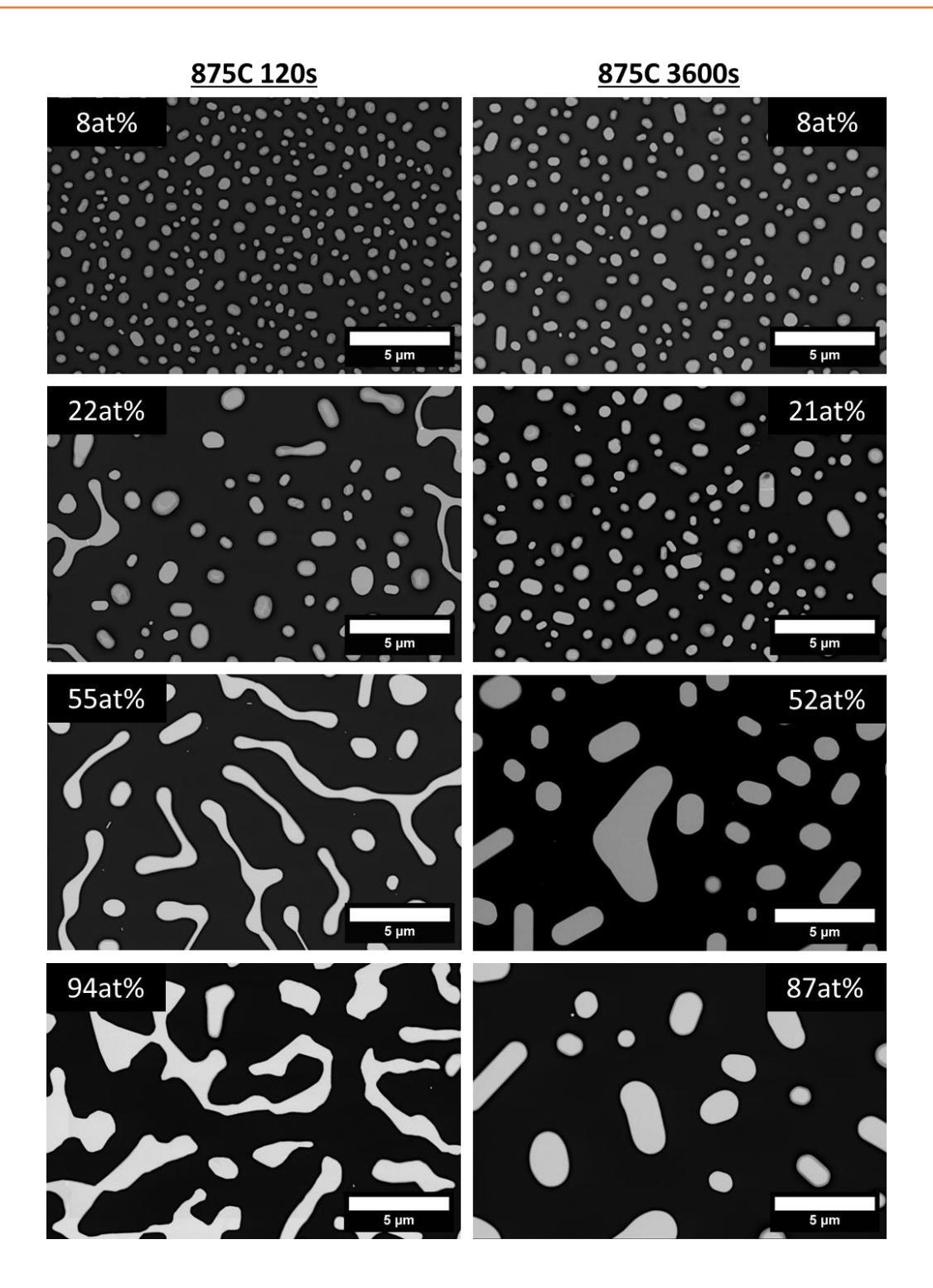


Figure 24: At low concentrations both samples appear very similar in shape and morphology. After 20 at% however samples heated up for a longer period of time stay at small slightly elongated particles, even at higher concentrations. Films heated up for 120 s on the other hand show drastic changes with increasing Au concentration. At 52 at% elongated structures are visible and at 92 at% there are even some areas with closed film visible.

## 4.3 Process-temperature variation

In order to investigate the influence of heating temperature onto the SSD kinetics, three samples were prepared at 900 °C, 910 °C and 920 °C for 120 s each. To compare the samples, Figure 25 shows graphs of the exposed over unexposed area (a), particle density (b), ECD (c) and circularity (d). Between 10 at% and 35 at%, the exposed over unexposed area decreases, thereby suggesting a slowdown of the SSD. SEM images in Figure 26 prove, that at low Au concentrations of ~15 at% all three samples show small, slightly elongated structures, whereas at 20-25 at% elongated structures dominate the image, with some areas where the film is still partially visible and hole growth is happening. This trend is also shown in particle density, ECD and circularity. After 35 at% the exposed over unexposed area increases for all samples and an area of enhanced SSD is visible until roughly 70 at%. In this area there is a large difference visible between the sample heated at 900 °C and the sample heated at higher temperatures. While the exposed over unexposed area of the 900 °C sample increases gradually, the exposed over unexposed area of the other two samples increases drastically by nearly tripling at some point. The SEM images reveal at this concentration an area of very fast-dewetting, where only small and round particles are visible. This area of fast-dewetting ranges from 56 at% to 69 at% for the 910C 12s sample and from 48 at% to 76 at% for the 920C 120s sample, which means that at higher temperatures the area of fast-dewetting is larger.

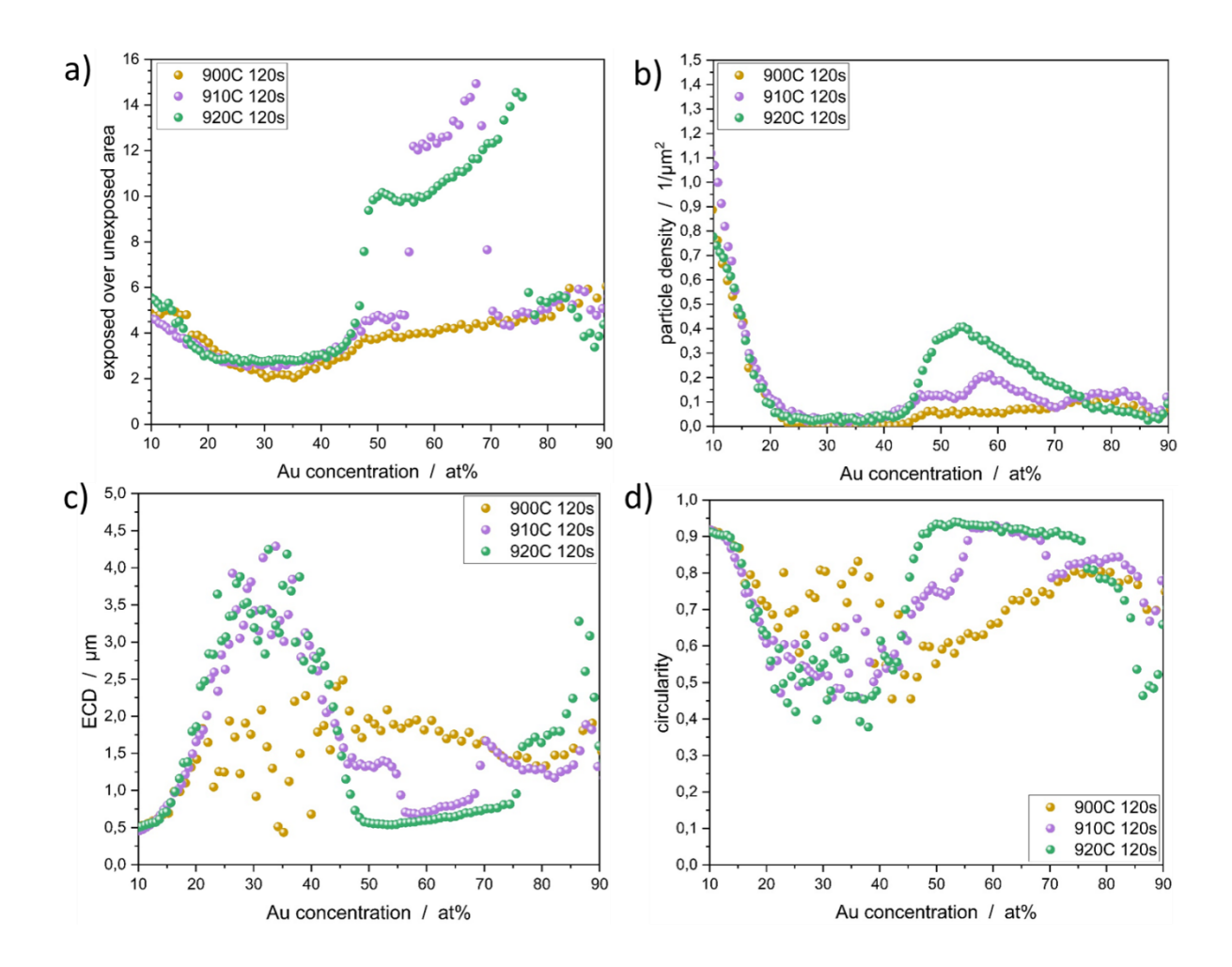


Figure 25: Comparing samples heated up for 120 s but at different temperatures of 900 °C, 910 °C and 920 °C show very similar SSD behaviours along most of the concentration range. At low Au concentrations an increase in Au concentration leads to a decrease in SSD up until roughly 35 at%. Afterwards the SSD starts to increase slightly again for all sample, however at ~50 at% a sudden change in the a) exposed over unexposed area is visible. This sudden change in kinetic is visible for samples heated at 910 °C and 920 °C, but not for the sample heated at 900 °C and goes along with a sudden decrease in c) ECD and increase in b) particle density and d) circularity. Samples heated up at higher temperatures show a larger area of fast SSD. At high concentrations between 70 at% and 75 at% the exposed over unexposed area drops again, reaching a similar value as between 20 and 40 at%.

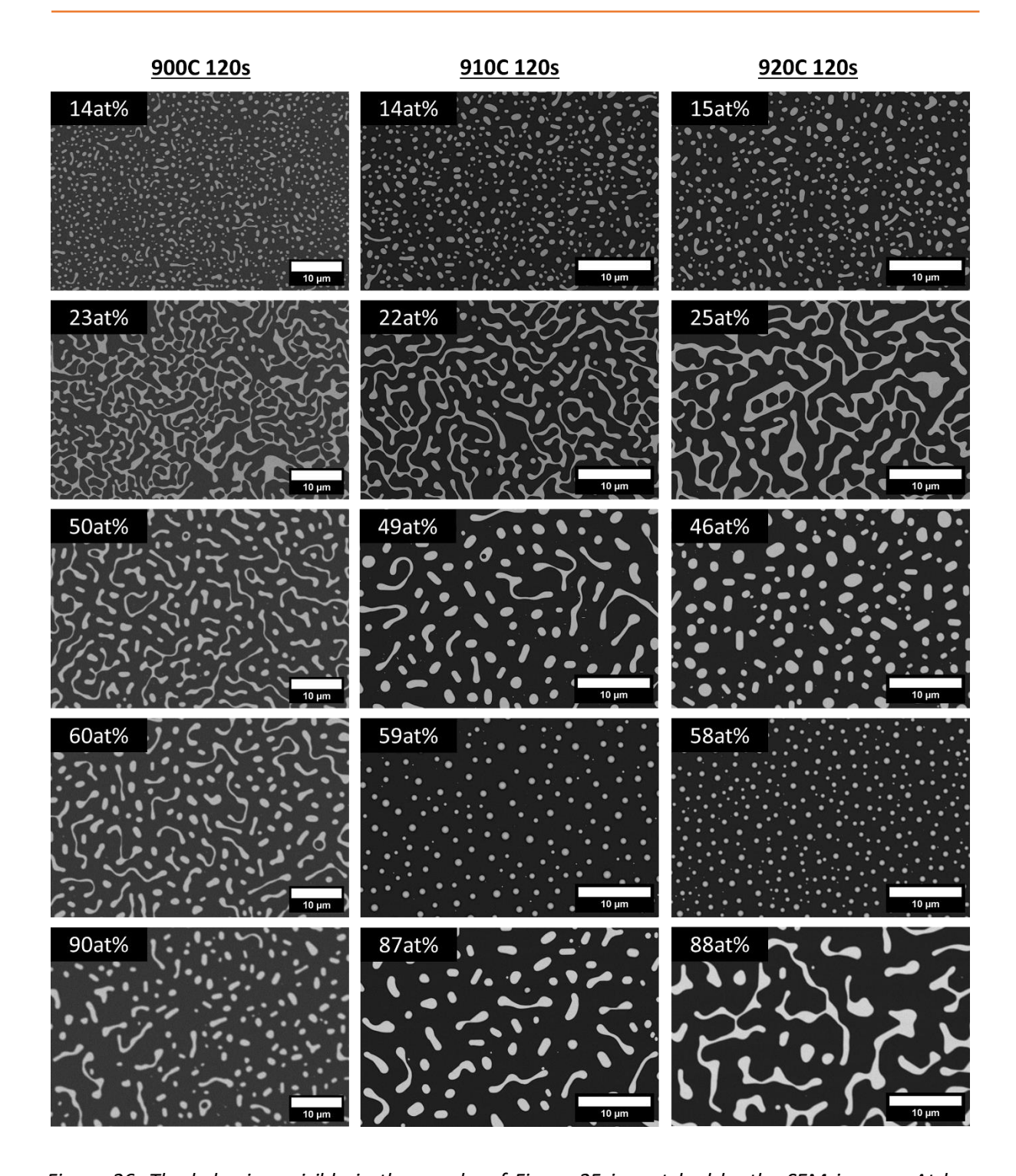


Figure 26: The behaviour visible in the graphs of Figure 25 is matched by the SEM images. At low concentrations small slightly elongated structures are visible. With increasing amount of Au, the structures become larger are more elongated, until a stage where hole formation and ligament break up are parallel. By further increasing the concentration the structures start to break down and the SSD kinetic enhances again. At roughly 60 at% samples heated at 910 °C and 920 °C reveal a sudden change in SSD showing small round particles, which indicate the final state and result of SSD, whereas the sample heated at 900 °C shows enhanced dewetting, but still elongated finger-like structures. At even higher concentrations the change of morphology is very sudden again, however now the structures increase in size. There are no significant changes in morphology after that.

The OR of the structures is of high interest. Figure 27 shows pole figure plots of all three samples at low Au concentration, inside of the fast-dewetted area (intermediate Au concentrations) and high Au concentrations. At low Au concentrations, all samples show some misoriented grains, but none the less a clear visible OR I between film and substrate appears. The OR is visible even stronger in MUD plots of the pole figures (see Figure A2). With increasing concentration, the OR enhances and gets more pronounced being most pronounced at 57 at% in the 900 °C sample. At very high concentrations of nearly pure Au an OOP orientation is still present, but the in-plane orientation is lost, revealing a fibre like texture. This behaviour is very similar for all samples, with an exception in the area of fast-dewetting. The samples heated at 910 °C and 920 °C show a complete loss of texture inside the area of fast-dewetting, whereas the sample heated at 900 °C still exhibits remaining texture.

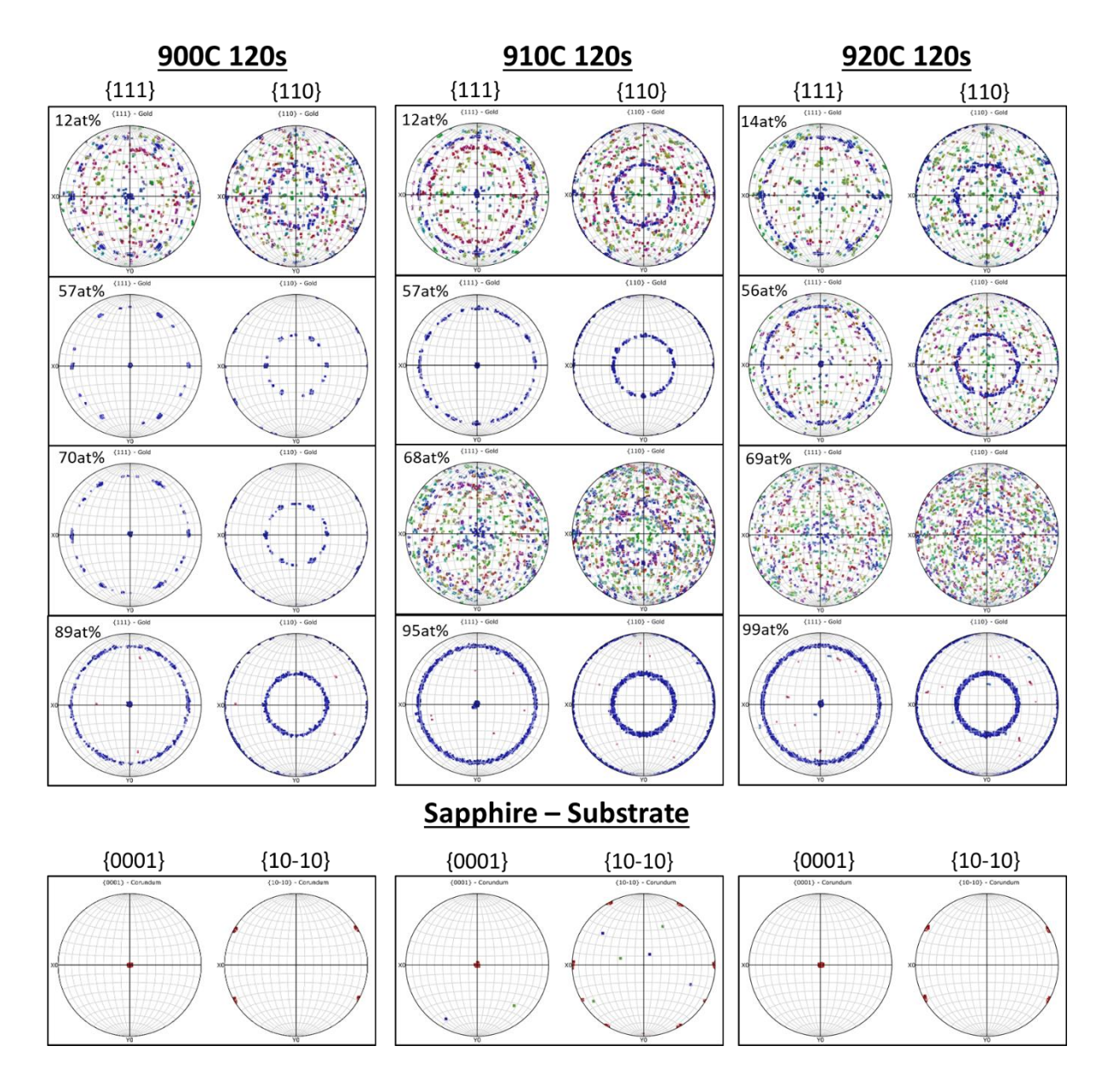


Figure 27: The Crystal orientation of the samples is changing significantly throughout the concentration range. At low concentrations an OR with in plane and OOP orientation is visible, together with some degree of random oriented grains. With an increase in concentration the OR gets more pronounced. The sample heated at 900 °C shows that the OR is most dominant at 57 at%. Inside of the area of fast SSD the OR is suddenly lost and the grains show completely random orientation for samples heated at 910 °C and 920 °C. At higher concentrations of nearly pure Au the in-plane Orientation is not visible anymore and the samples shows a fibre like structure with strong OOP, but no in plane orientation.

#### 4.4 LSD at 1000°C

To investigate the OR loss dependent on the temperature, two samples were heated up to 1000°C for 30 s. One of the samples was quenched to room temperature after the 30 s, the other one was cooled down to 850 °C with 1 °C/s and held at this temperature for 180 s, after which the sample is also quenched.

Figure 28 shows the exposed over unexposed area (a), particle density (b), ECD (c) and circularity (d) of both samples over the whole concentration range. At low Au concentrations the exposed over unexposed area scatters a lot, but behaves similar to all previously discussed samples in chapter 4.2 and 4.3 it appears a trend, that the exposed over unexposed area decreases between 10 at% to 30 at%. The ECD decreases in that area as well, whereas the particle density increases. Between 30 at% and 60 at% a plateau is visible in all four diagrams. After 60 at% the exposed over unexposed area begins to increase similar to other samples. Parallel to the increase, the ECD increases again, and the particle density is decreasing. The circularity on the other hand does not change significantly anymore after roughly 30 at%, which might indicate that the general morphology is not changing. Comparing the SEM images in Figure 29 shows why. At lower concentrations the morphology shows some round particles, but most of the structures are slightly elongated, thus leading to the decrease in circularity. However, at 40 at% the SEM images show only round particles of different sizes. At this point, the changes in exposed over unexposed area are only caused by the change in particle size and density, but the morphology stays the same. Thereby, also the circularity does not change with increasing concentration. Overall, both samples are nearly indistinguishable in the graphs as well as in the SEM images.

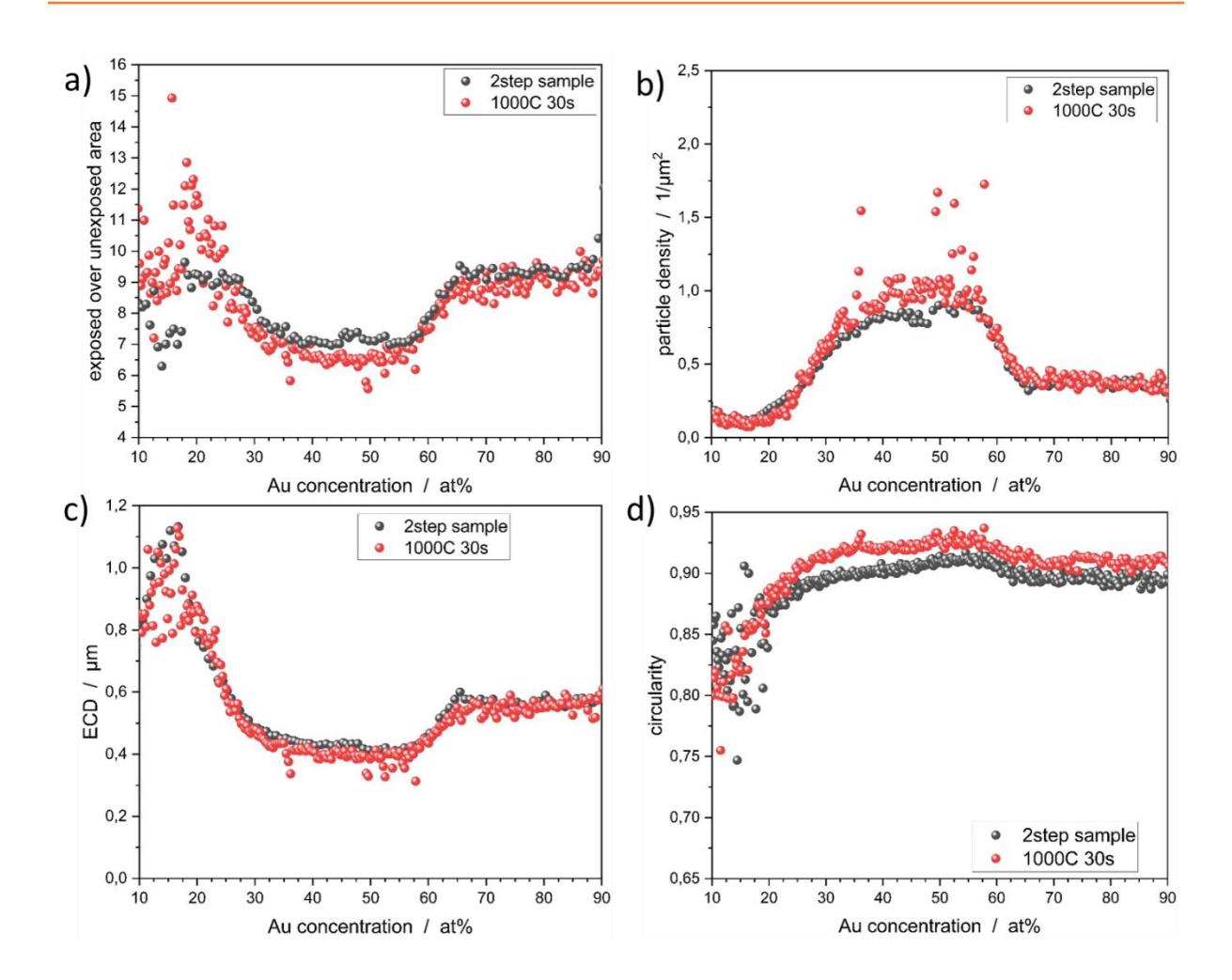


Figure 28: Both samples were heated up at 1000 °C for 30 s, but one of the samples was quenched, were as the other was firstly cooled down slowly and quenched afterwards. This different tempering procedure seems not to influence the SSD kinetic in any way, thus all graphs of both samples appear to be rather similar.

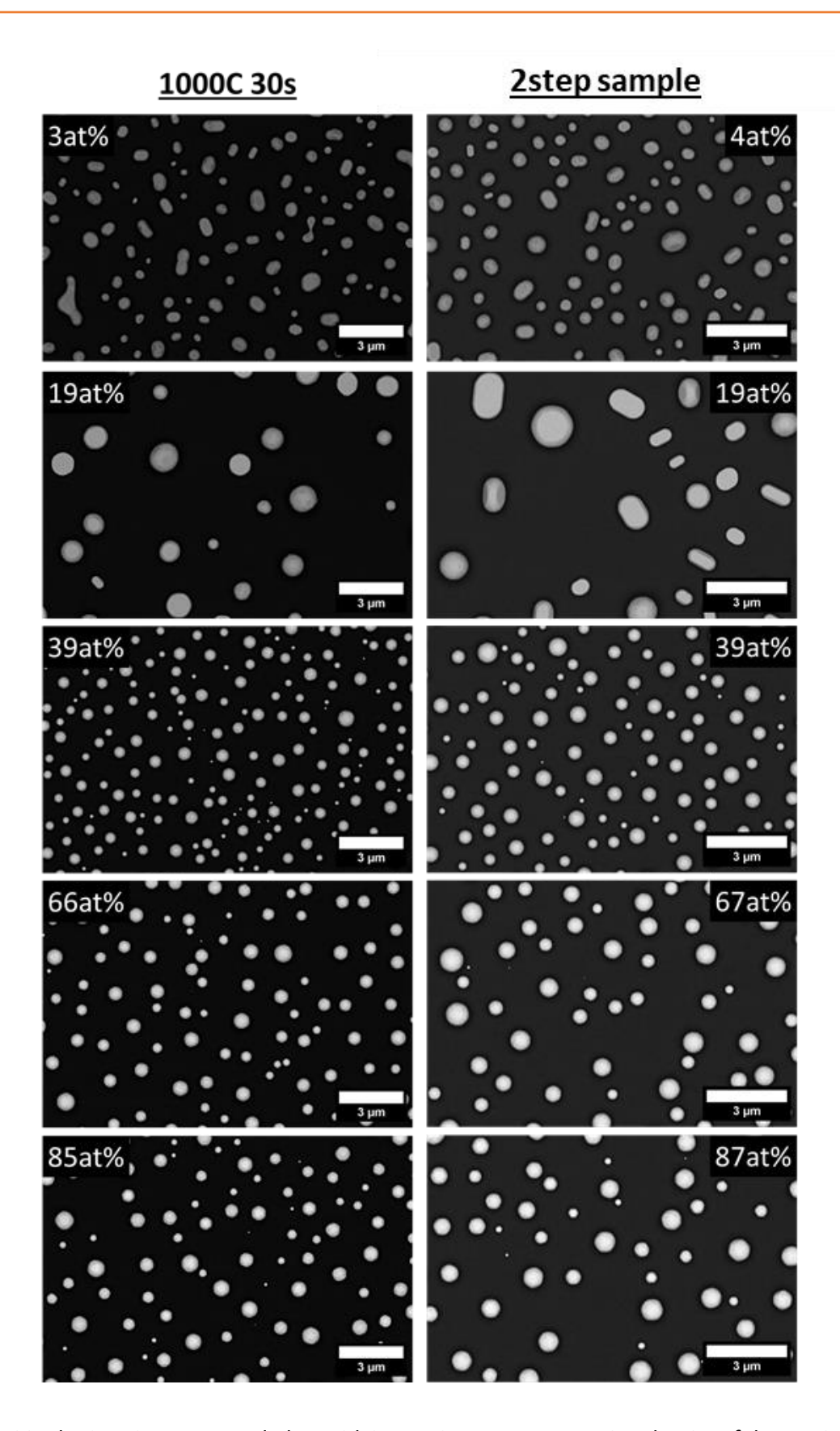


Figure 29: The SEM images reveal, that with increasing Au concentration the size of the particles starts to increase at first. However, after 20 at% the size of the particles drops, and small round particles are visible. This particle shape does not change significantly with increasing concentration. The size of the particles on the other hand tends to increase with increasing concentration.

The SSD kinetic of both samples behaves quite similar, but the OR of the samples is a bit different. Figure 30 shows pole figures of the {111}, {110} and {112} of both samples at different concentrations. At low Au concentrations the samples show an OR similar to the samples heated at 910°C and 920°C. The OR I of the sample is clearly visible (see better Figure A3), however many grains are also randomly oriented. At the concentrations around the lowest melting temperature of the system both samples behave differently. The sample which was quenched immediately after being heated for 30 s at 1000 °C shows a clear OR I. On the other hand, the samples which was cooled down slowly at first and held at 850 °C for additional 120 s shows a complete loss of OR at these concentrations, which is analogous to the samples heated at 910 °C and 920 °C. At high concentrations both samples now behave similar, showing an OR with some random oriented grains.

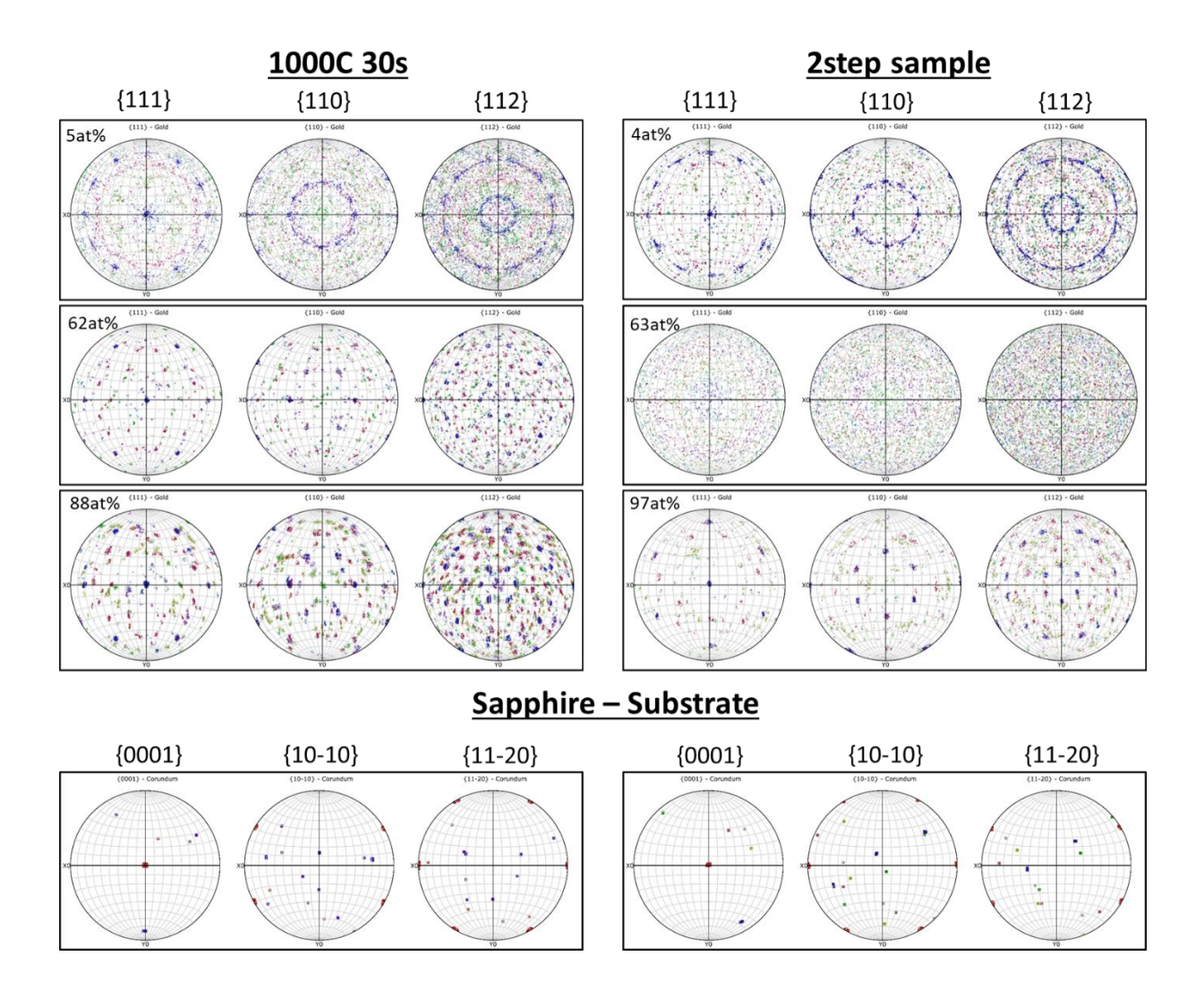


Figure 30: The EBSD measurements reveal a difference between the two samples. At low Au concentrations both samples show OR I with some randomly oriented grains. At high Au concentrations they also show the same behaviour with OR I and some randomly aligned grains. Around the lowest melting temperature of the system however the two samples behave different. The 1000C 30s samples shows still an OR I at this concentration, whereas the 2step sample has a complete loss of orientation at this point.

## 5 Discussion

### 5.1 Peak analysis of local XRD measurements

Figure 31 a) show that the lattice parameter, which was calculated from the peak position of the XRD measurements, increases steadily with changing measuring positions. Analogous to that, Figure 31 b) shows a very similar steady increase of the lattice parameter with increasing Au concentration. As described already in Section 4.1 the concentration was determined by comparing the lattice parameter with the lattice parameter of bulk alloys [65] (see Figure A1). The comparison with bulk values is possible, because after SSD the structure size lies in the micrometre range, where the lattice parameter is not affected by size effects. This is validated by other EDX measurements on unheated samples (see section 4.1 and Figure 21), where the concentration trend is similar and by the literature, where this method is already used [66].

The peaks shape of the {0006} peak from the sapphire substrate differs strongly from the {111} peaks of the alloy (see Figure 22). The peak width can be influenced by the crystallinity of the samples. Because the substrate is single crystalline, the peak is as small as the incident peak, which means it could be used to identify the initial peak shape. The peaks of the alloy on the other hand are significantly broader. The XRD measurements were conducted by using a beam slit of 0.5 mm, which means that the measurements were not at one single concentration, but rather an averaging over a range of concentrations. The beam has its strongest intensity in the centre of measurement, and so the highest intensity of the peaks corresponds to the concentration in the centre of the measured area. The broadening of the beams originates from the other concentrations measured, which have different lattice parameter and so a different position of the {111} peak.

The peak height in Figure 22 increases steadily with increasing Au concentration. Analysing the integrated intensity of the peaks (see Figure 31 c) proves that not only the height, but the overall intensity of scattering is increasing with increasing Au concentration. As already mentioned in section 3.6 the scattering amplitude is increasing with increasing Z-number [67]. The Z- number of Ni is lower with 58.69 compared to Au with 196.97. As a result, the integrated intensity increases with increasing Au concentration.

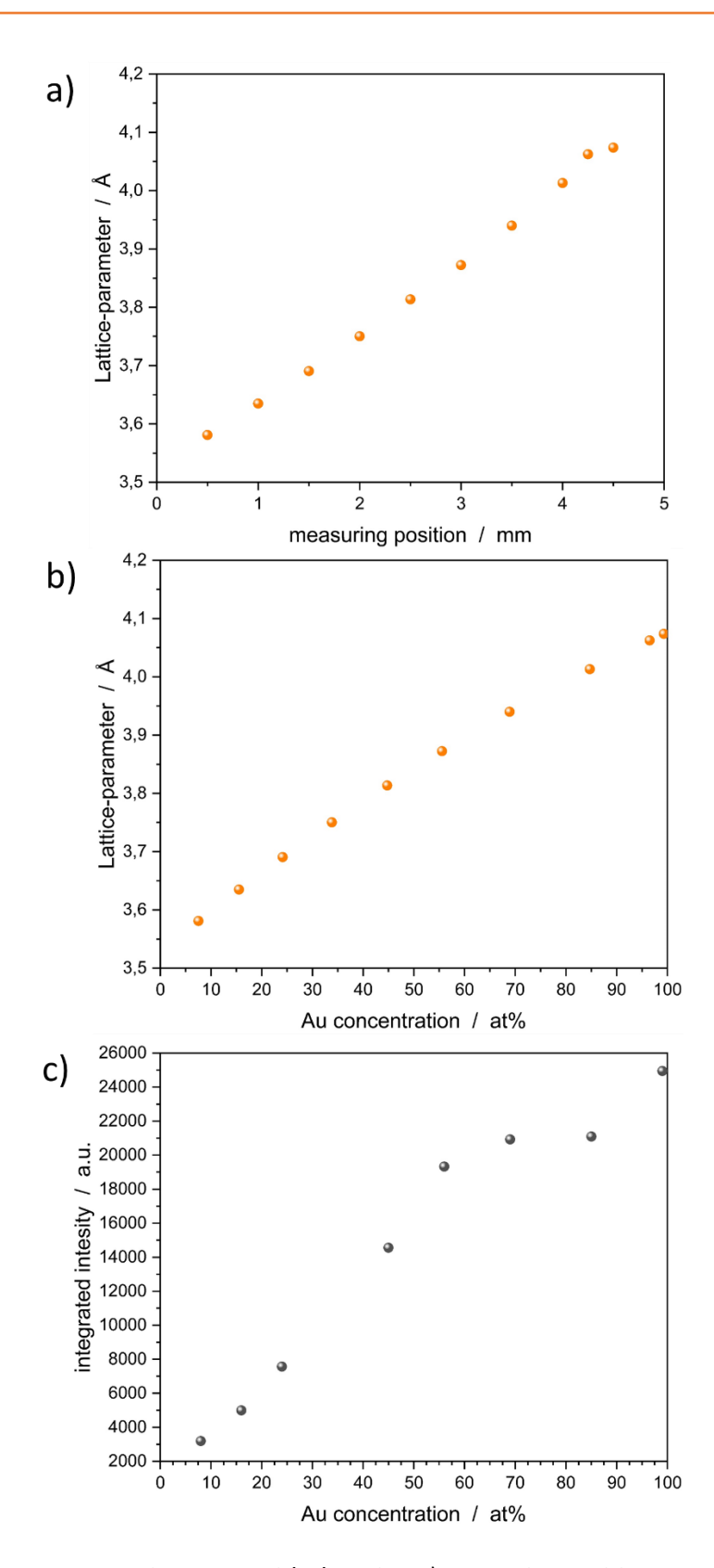


Figure 31: The lattice parameter increases with changing a) measuring position as a result of the steady increase of Au over the samples. b) As a result, the changing lattice parameter with changing Au concentration fits nicely to each measuring position. The c) integrated intensity increases with increasing Au concentration, because of the higher atomic scattering amplitude of Au compared to Ni. The integrated intensities were extracted from fits, which can be seen in Figure A4 and Figure A5.

### 5.2 Influence of Au concentration onto SSD

As mentioned in section 4.2 - 4.4 for all samples described in this study the exposed over unexposed area begins to drop between 10 at% to 35 at%. There are already some studies, which conduct the SSD behaviour of Au and Ni at different concentrations. In a Study of Barda and Rabkin [20], they investigated the SSD of Ni with around 1 at% Au in different configurations. The different configurations are pure Ni, doped Ni, an Au layer between two Ni layers and an Au layer on top of Ni. They observed, that in all configurations, adding Au to Ni will slow down SSD. The highest degree of reduction is observed for an Au layer on top of the Ni layer, similar how it is done in this study. They explained this behaviour via an increase in anisotropy of the surface energy. This increased anisotropy leads to shallower grooves, with a smaller curvature, and thereby reduced mobility. It is also noteworthy, that Au does not only segregate at the surface and grain boundaries, but also at the interface between substrate and sample, where it might influence the interfacial energy between the alloy and the sapphire substrate [20], [68].

At higher Au concentrations, above roughly 35 at%, the exposed over unexposed area starts to increase again for all samples until around 75 at%. A similar behaviour was observed by Dierner et al. [69]. In their study the exposed over unexposed area of an AuNi film on sapphire increased strongly, in the same concentration range. The change in SSD was attributed to the change in melting temperature of the system with changing concentrations. The lowest melting temperature of the system lies at around 55 at% Au with a temperature of 955 °C. The main process for SSD is surface self-diffusion and therefore the diffusivity of the system is one of the main values to influence SSD. The diffusivity of metals with fcc crystal structures is similar at similar homologous temperature, which implies on the other hand, that the diffusivity increases at higher relative temperatures compared to the melting temperature. In this study the process temperatures were not changed and kept constant. The ratio between process temperature and melting temperature will, on the other hand, change with changing concentration and melting temperature, which explains the increases SSD at concentrations where the melting temperature is low [70].

It is noteworthy, that very high and low concentrations are difficult to investigate with the combinatorial sample structure. At the boarder of the samples edge effects may alter the result of the SSD kinetic. Additionally, the films will most likely not be closed at such small film

thicknesses [37]. This adds already present holes to the system, therefore increasing the dewetting. It is also not possible to ensure 100 at% Au or Ni at the edges of the sample, at least in the configuration used in this study. The shutter was moving over the whole sample and therefore covering at some point every area of the sample. In future studies edge effect could be reduced be adding areas around the gradient where the shutter is always uncovering the sample. In that way these areas would be composed of only the pure elements and act as a transition zone for edge effect. Because of unstable deposition rates at the beginning of a process the sample had to be covered completely at the start, therefore making it not possible to apply areas of pure elements in this study.

### 5.3 Influence of time onto SSD

Comparing the two samples heated at 875 °C for 120 s and 3600 s (see Section 4.2), the influence of vastly different heating times can be observed. When only considering the exposed over unexposed area in Figure 23 a) it seems that from 10 at% to 75 at% the SSD of both samples is very similar, even though the heating time of one sample was 30 time longer. When comparing this with the SEM images of Figure 24 it appears that even though the exposed over unexposed areas are nearly the same, the SSD of the samples is different after already 20 at% and higher. At lower concentration of around 10 at% the SEM images show a similar picture of round particles, but at 20 at%, whilst the 875C 3600s sample still shows only round slightly elongated structure, the SEM images of the 875C 120s sample now show also elongated structures. With even higher concentrations the differences between both samples get stronger. The change in morphology cannot be depicted by the exposed over unexposed area because it only gives a ratio between areas which are covered and areas which are uncovered, but gives no information about the shape of still covering areas. The circularity plot in Figure 23 d) on the other hand describes only the shape and morphology, which thereby shows after 20 at% the difference between both samples. Some studies only use the exposed over unexposed area to describe the dewetting behaviour of their sample [20], which hold a lot of information about the state of SSD but should always be compared to either SEM images or shape describing values like circularity.

The SEM images in Figure 24 show that when the 875C 120s sample is already dewetted rather far, as for example at 8 at%, the differences between the 875C 3600s samples are marginal or even not notable. At concentrations however where dewetting is slow, a large difference is visible between both samples. Brandon and Bradshaw [71] as well as Pierre-Louise et al. [72] derived models for the mass transport during SSD, especially edge retraction. As a main driving force for edge retraction the reduction of curvature is accounted for. While the edge retracts, it increases in height. This lowers the curvature of the edge, and thereby slowing down the SSD kinetic. Via Monte Carlo simulations of ultrathin films Pierre-Louis et al. established a model for this process:

$$\frac{dx_0}{dt} \propto D^{\frac{1}{2}} d^{-1} t^{-\frac{1}{2}} \tag{14}$$

, Where D is the surface self-diffusivity, d the film thickness and t the time. This shows, that further dewetted film dewet slower, which gives areas with slower dewetting the capability to catch up with longer annealing time.

## 5.4 SSD at higher temperatures

As discussed in chapter 4.3 at temperatures of 910 °C and higher, the samples show an area of very fast-dewetting. When comparing the temperatures and size of the fast-dewetting stripe with the phase diagram of AuNi, the fast-dewetting stripe is located around the area of lowest melting point of the alloy system (see Figure 32). The lowest melting point of the alloy lies at 955 °C at a concentration of 57 at% Au [73]. In addition, the area increases from 540 μm at 910 °C to a width of 1180 µm at 920 °C. This together with the sudden change in morphology raises the question if a phase transformation from solid to liquid is occurring inside the area. Looking at the particle shape, only round particles are present within these areas. During SSD beside round particles always also elongated particles are present, even at high temperatures [74] or long equilibration times [15]. On the other hand, a comparison of the morphology inside the fast-dewetting area with a sample heated above the melting temperature at 1000 °C (see Figure 33) backs the suggestion of melting. It seems that the overviews show nearly the same appearance of many particles of different sizes, but all with the same shape. Also, a closer look onto specific particles reveals, that the size of the particles may differ, but the shape appears to be similar. In the already mentioned study of Curiotto et al. they also saw a similar picture of only round particles after 5 min of LSD at 1357 K, but after 78 h of SSD at 1253 K, still some elongated structures were visible [25]. This supports the hypothesis, that all three samples undergo the same phase transformation in that concentration range, from solid to liquid, which implies that rather than SSD in the area of fast-dewetting LSD is occurring. However, for the samples heated at 910 °C and 920 °C this would mean a MPD of roughly 40 °C – 50 °C.

The melting point of a material system is a function of the size and shape of the material and so, thin films can have a reduced melting point compared to their bulk variant. There are studies which calculated the theoretical MPD of metal systems. In a study of Kaptay et al. [75] they calculated the MPD of a levitating thin Cu slap melting into a molten slap (route A) and into a molten droplet (route B). Considering a film with a thickness of 40 nm the MPD for route A lies around 10 °C, whereas the MPD for route B lies around 70 °C. The specific surface energy for a slap melting into a slap does not change significantly, thereby the MPD is rather low. A slap melting into a sphere reduces the relative surface of the system, thus also reducing the specific surface energy. This results in a much larger MPD. The melting route B described in the study by Kaptay et al. [75] is close to the melting phenomena which occurs in this study,

where a thin film melts into round droplets. This might therefore explain the reduced melting point of the system however, the model describes a levitating metal slap, without any interaction between metal and a substrate. It also does not take the grain sizes or internal stresses of the metal film into account. Especially the grain size may have a strong influence onto the melting temperature of a metal. At grain boundaries as well as surfaces the atoms are weaker bound, resulting in a reduction of energy needed to melt the material at those sites. Thereby grain boundaries act as nucleation sites for melting. Wejrzanowski et al. [35] showed, that a reduced grain size can lead to a MPD of a few hundred degrees. Even though the grain size was not measured in this study, the grain size for thin films produced via PVD lays in the range of the film thickness [76]. The overall film thickness in this study is 40 nm, but because the film is produced via depositing two metals above each other, the film thickness of the individual metals is below the 40 nm, thus also the grain size of each metal could be even smaller.

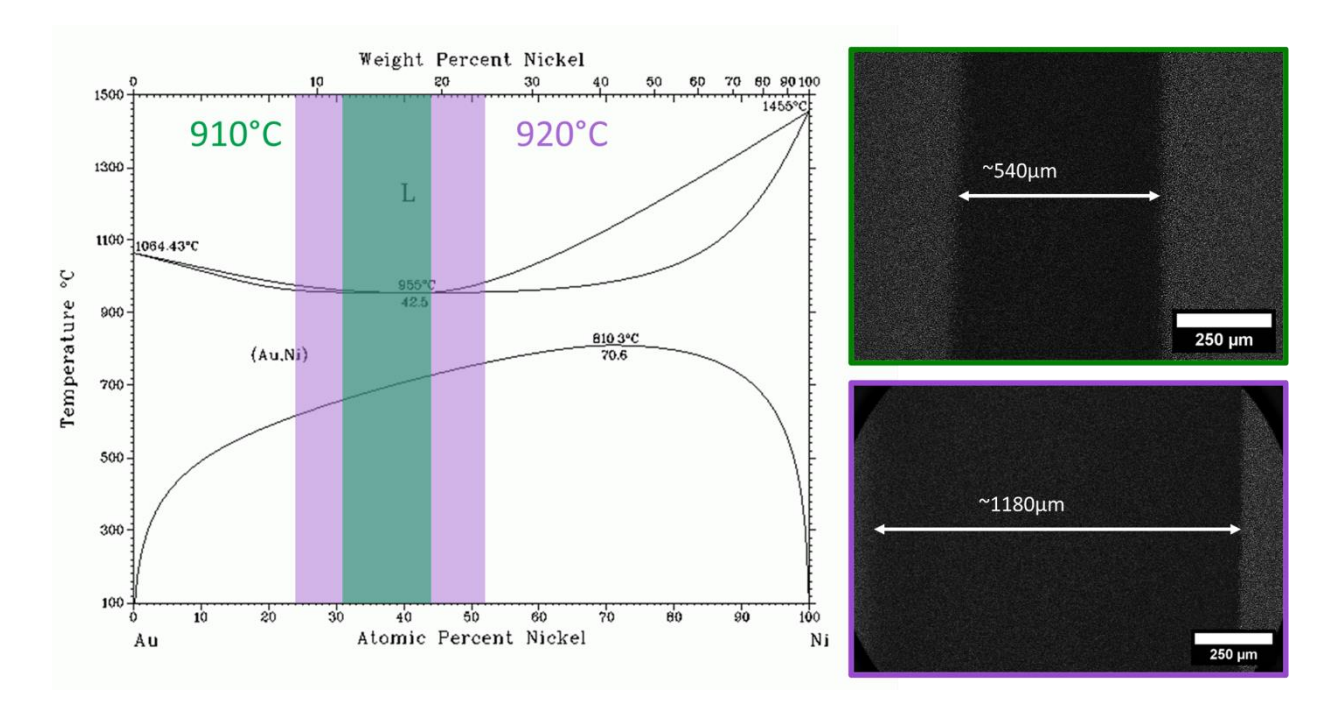


Figure 32: The purple and green stripes mark the concentration range where the samples show fast-dewetting and round and small particles. Those areas lie at the lowest melting point of the alloy and increase in size with increasing temperature, which means that inside the area of fast-dewetting melting might be the reason for the sudden change in appearance.

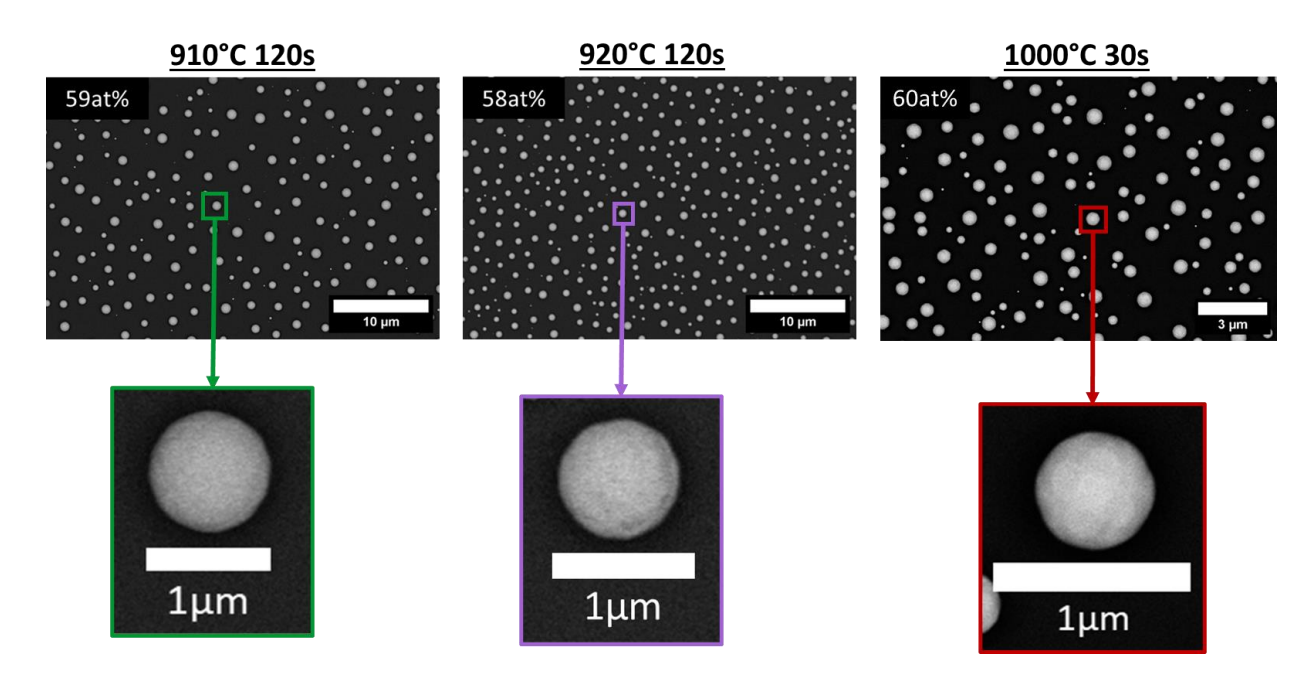


Figure 33: The morphology of samples heated at 910 °C and 920 °C inside of the fast-dewetted area is compared to a sample heated at 1000 °C, which is above the liquidus line for a wide Au concentration range. The appearance of all samples is nearly equivalent, and the occurrence of exclusively round particles suggests that in the fast-dewetting area melting may occur, even though annealing took place 40 °C to 50 °C below the melting temperature.

#### 5.5 Texture evolution at 900 °C

At 900 °C the texture evolution over the concentration is rather linear. At low Au concentration of 12 at% the scattered plots of the pole figures (see Figure 27) show several random oriented grains, but certain measured grain overlaps at specific angles. Figure 34 shows coloured EBSD maps, in which a green colour corresponds to grains in OR I and purple coloured grains in OR II. First and foremost, an increased number of grains oriented with the {111} plane OOP are visible. This combined with the in-plane orientation, where the {110} crystal direction is oriented parallel compared to the {01-10} direction of the sapphire substrate indicates epitaxy between the metal film and the ceramic substrate. As already covered in section 2.3 such an in-plane and OOP alignment is the OR I and was already observed in literature for Ni on sapphire [77]. With increasing Au concentration, the texture of the system changes a bit, and the OR becomes more pronounced. At 57 at% no random oriented grains are visible anymore in the scattered plots (see Figure 27) and the EBSD maps (see Figure 34) show only grains in OR I with just one exception of a grain oriented in OR II. This might be a result of the changing lattice parameter and therefore also the changing lattice mismatch between alloy and substrate. According to equation (6), at 12 at% the lattice mismatch is 7.07 % and at 57 at% the lattice mismatch is 0.15 %, when using  $d_{30\overline{3}0} = 1.374$  Å [30] of the substrate. One reason for the formation of ORs is the reduction of surface energy and strain at the interface. If the mismatch of the system tends to zero each atom of the metal will be able to interlock with an atom of the substrate, thus reducing the strain of the system significantly [27]. At even higher concentrations of nearly pure Au the in-plane orientation is lost, and therefore also the OR, but the alignment of the {111} planes being parallel to the {0001} remains, leaving behind a fiber-like texture. This was also observed in literature for pure Au on a single crystalline sapphire substrate [78].

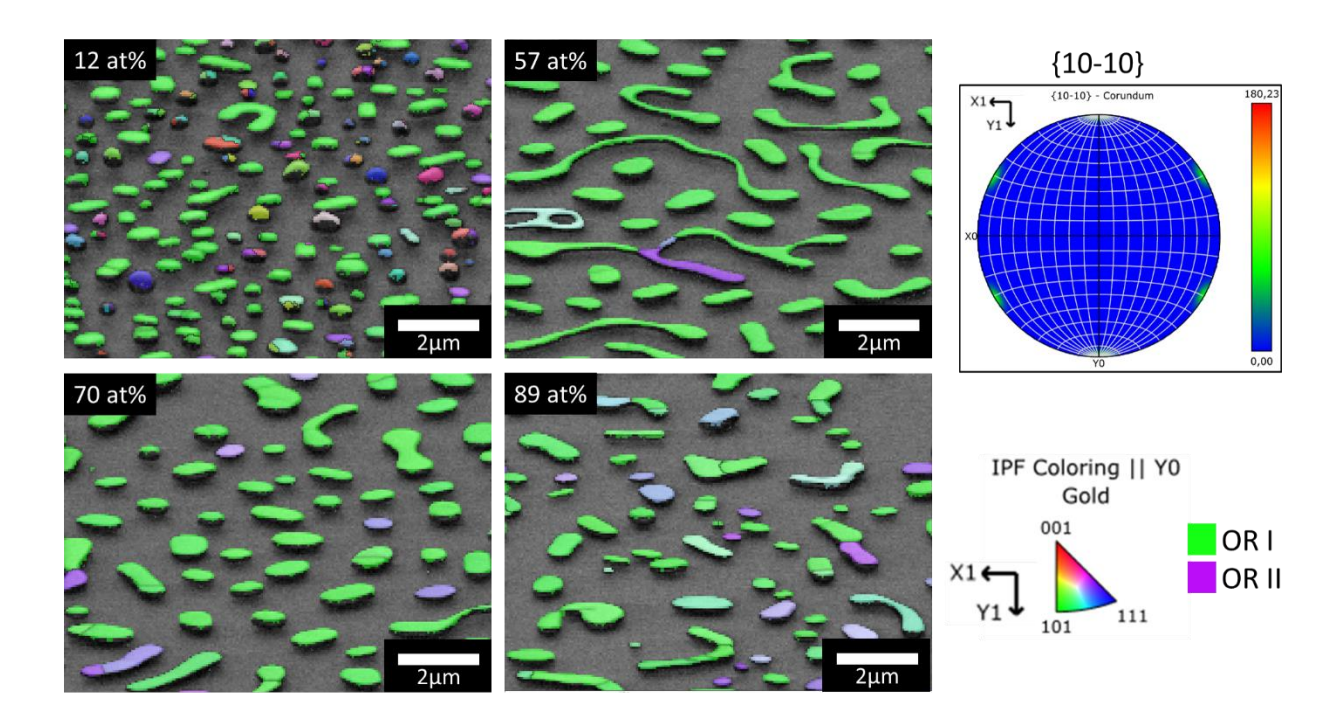


Figure 34: The colour of the particles corresponds to the grain orientation in y-direction. Green structures indicate grains which are oriented in OR I. At 12 at% several grains are randomly oriented, however OR I tends to dominate. With increasing concentration, the OR becomes more pronounced, and all grains are oriented in OR I instead of some purple grains, which correspond to OR II.

### 5.6 Texture evolution of partially molten samples

Although the samples heated at 910 °C and 920 °C show a similar texture evolution for low Au concentrations (0 at% to ~55 at%) and high Au concentrations (70 at% to ~100 at%) compared to the sample heated at 900 °C, a significant difference can be found in the area of fast SSD, since the texture in this area is completely lost. If the samples, heated at 910 °C and 920 °C, are partially molten, it appears that the loss of OR is related to the melting of the samples. With increasing temperature, the concentration range, where the OR loss can be observed, increases (see Figure 35 a). The loss of texture ranges from 59 at% to 69 at% when heating at 910 °C and from 55 at% to 75 at% when heating at 920 °C, which displays a doubling of the concentration range without OR. However, not all particles, which seems to be molten at one point, show the loss of OR. The area of OR loss is in all cases narrower, than the area of melting. This is seen in the exposed over unexposed area graph next to the mean angular deviation (MAD) in Figure 35. The exposed over unexposed area also changes drastically around the region of texture loss, but the exposed over unexposed area change expands even further. Even though it seems obvious that LSD has happened, it is quite surprising, that the texture is completely lost, since it is not observed for similar material systems. In a study of Curiotto et al. [25] they investigated the dewetting behaviour and texture of pure copper particle on a single crystalline sapphire substrate produced via SSD and LSD. There was a change in preferred OR between SSD and LSD visible in their study, but still in LSD a preferred OR was present and therefore a clear texture of the Cu grains. The difference might be explainable by the difference in crystallization between a pure element and an alloy.

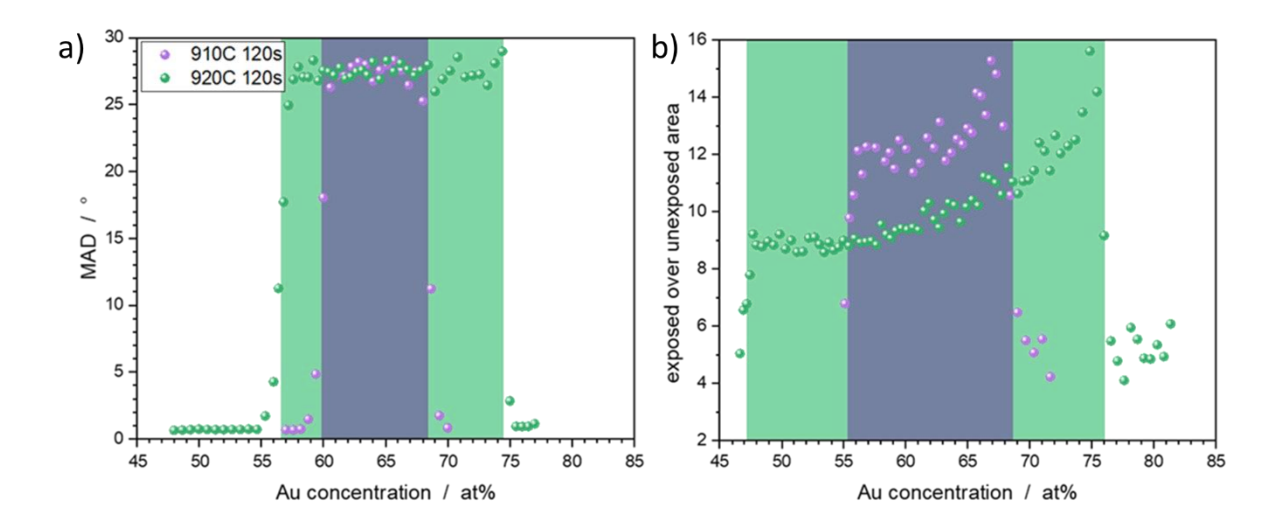


Figure 35: a) The MAD is depicted for the {111} planes in Z-direction. At a certain concentration the MAD increases drastically, up to a value of about 26°-27°, which indicates random orientation. A higher temperature leads to a larger concentration range, where the orientation is lost. b) The exposed over unexposed area in the same area also undergoes drastic changes. The area of change for that is even larger compared to the loss of OR.

The areas of texture loss and melting are very narrow for samples heated at 910 °C or 920 °C. To better understand the reasons for the texture loss a sample heated at a higher temperature of 1000 °C is advantageous. Figure 36 shows a plot of the MAD of the {111} peak OOP of the 2step sample. If comparing the MAD with the phase diagram of the AuNi system, three areas of different behaviour appear. At points with the highest melting temperature, or in other words with very high or very low Au concentration, the temperature is not sufficient to melt the alloy. In this region SSD occurs. If the process temperature is higher than the melting temperature LSD is the underlying process instead of SSD. However, the AuNi sample system has a solidus and liquids temperature instead of one melting temperature. It appears, that if the temperature is high enough to surpass the liquidus line, the OR is lost (region C in Figure 36). In this case the alloy is fully molten, meaning it is in an amorphous state thus no OR can be present. When now cooling down the sample, it seems that the crystallization happens without interacting with the substrate or in other words, homogenous nucleation or nucleation at the surface is happening rather than heterogeneous nucleation at the interface. As a result, the crystals forming when cooling down, do not form an OR and the grain orientation will be random. If the temperature is not high enough to surpass the liquidus line (Figure 36 region b), but high enough to surpass the solidus line, melting occurs and LSD happens (only round particles present), though the temperature is not high enough to fully melt the film. This results in solid and liquid regions in one single particle. Because there are

now still solid parts present, also crystals are still present. Several studies suggest, that melting occurs at the surface of a film [33], which means, that the remaining solid phases (thus crystalline phase) are located at the interface between alloy and substrate. During the crystallization when cooling down, those crystals will now determine the orientation of the whole particle and therefore the OR is not lost if the liquidus lines is not surpassed.

Unfortunately, the 1000C 30s sample did not exhibit the same OR loss as the 2step sample. This difference is not analogous to the above-described effect but might be a result of the heating process itself. Quenching from 1000 °C down to room temperature applies a large amount of thermal stress into the system, and thereby also onto the silicon nitrate  $(Si_3N_4)$  Wafer on which the samples are mounted for heating. This stress can lead to a shattering of the Wafer, thus hindering a proper and controlled cooling down of the sample, which might result in the deviation between of texture evolution between the 2step sample and the 1000C 30s sample.

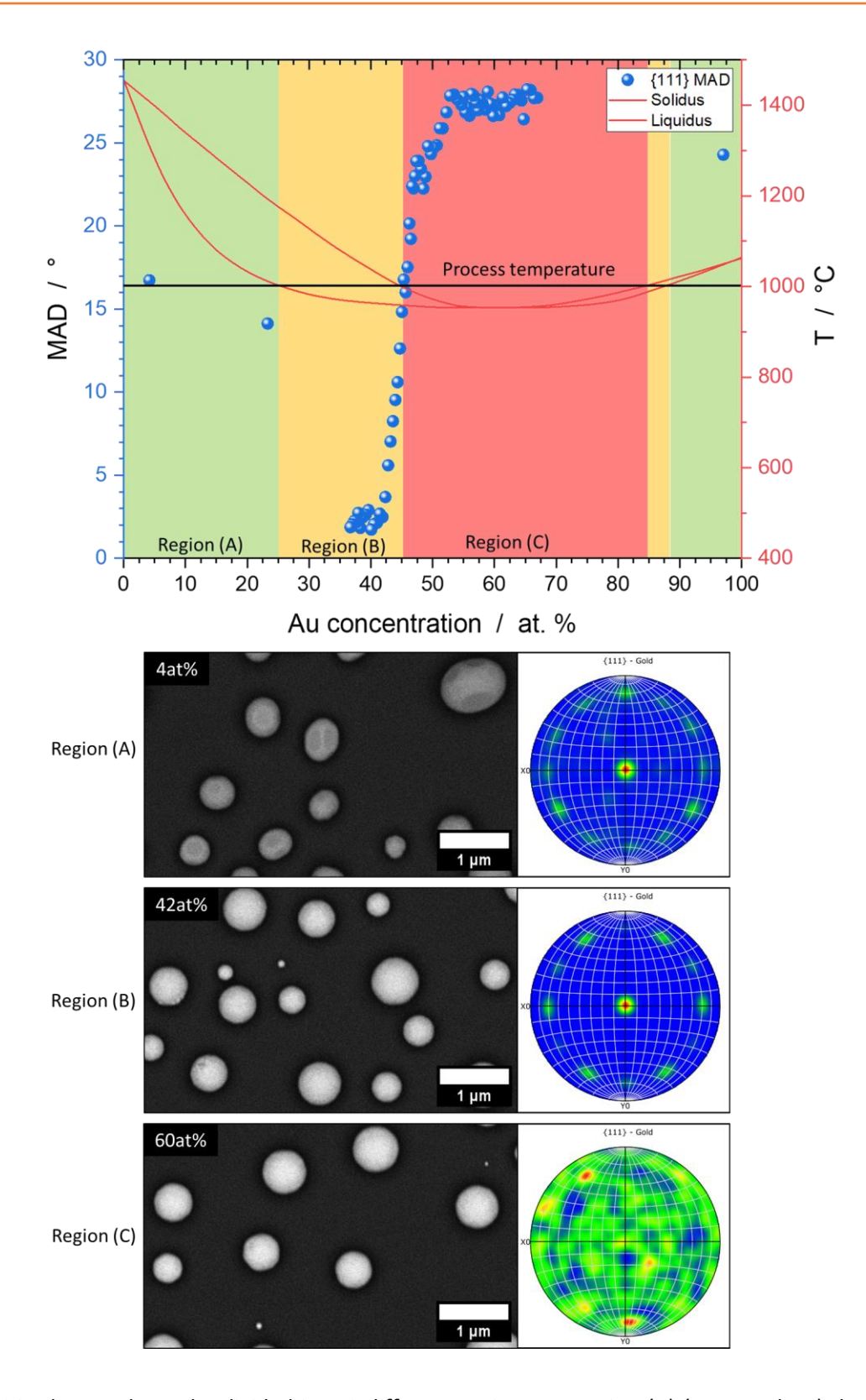


Figure 36: The graph can be divided into 3 different regions. In Region (A) (green colour) the process temperature does not exceed the melting temperature of the system. Thereby SSD occurs similar to other samples, already covered in this thesis. In region (B) (orange colour) the temperature is high enough to surpass the solidus line, but not high enough for exceeding the liquidus line. The particle morphology represents that of LSD, but the OR still remains in that region. In region (C) (red colour) the temperature is now high enough to also surpass the liquidus lines. This results in a fully molten sample, which undergoes LSD. In region (C) the OR is lost even after cooling down.

## 6 Conclusion

SSD is an efficient route to manufacture metal nanoparticle, which are of high interest for catalysis, biomedical applications, or imaging. However, the precise processes behind SSD are still unclear. Especially the complexity of bimetallic alloys is difficult to investigate in a conventional way.

In this study the use of a combinatorial approach was developed, by producing AuNi gradient thin films. Via EDX and XRD measurements it was shown that the Au concentration and thus the lattice parameter of the alloy can be successfully controlled over a wide range (~0 at% to ~100 at%). As a result, the number of samples needed to study the SSD kinetics and texture evolution, together with aspects of MPD and texture evolution during LSD, over nearly the whole concentration range of the AuNi system was effectively reduced to only 7 samples.

The studies on SSD Kinetics revealed significant changes over the concentration range. Between 10 at% and 35 at% SSD appears to slow down with increasing Au concentration. Afterwards the trend is turning around and between 35 at% and 75 at% the SSD kinetic increases again. This overall trend was observed on all samples in this study in which is in-line with literature [20], [69].

The investigations of the influence of time on SSD at 875 °C showed, that regions of slow SSD can catch up with time, whereas areas of already fast SSD do not show significant differences after heating times of 120 s and 3600 s. During SSD one of the main diving forces beeing the curvature of the surface is reduced, which as a result will slow down SSD as SSD progresses further [72]. In addition, the exposed over unexposed area is not solely sufficient enough to describe the state of SSD, as the covered area is similar after long heating times, but the morphology is clearly different. A shape describing factor like the circularity is therefore additionally needed to fully investigate the SSD behaviour.

The texture of the AuNi system annealed at 900 °C for 120 s was systematically investigated. The EBSD data showed, that OR I is the main OR in the AuNi-Sapphire system for a wide concentration range. Additionally, a sharpening of the epitaxial relation was found with decreasing misfit between the {10-10} planes of the sapphire substrate and the {110} planes of the alloy.

Annealing at 910 °C and 920 °C led to an area of anomalously strong SSD between 56 at% to 69 at% and 48 at% to 76 at%, respectively. Comparing the morphology of the sample with an actively molten sample suggests, that a melting point reduction has occurred, and the samples were in the liquid state within these areas. Secondly, a texture loss was observed within the molten areas. A detailed analysis of the texture at the actively molten sample at 1000 °C revealed 3 regions of dewetting:

- Region (A): The temperature is not high enough to exceed the solidus line, therefore SSD happens, and the texture of the system is still present.
- Region (B): The temperature is high enough to exceed the solidus line, but not the liquidus lines, therefore LSD is occurring, but the OR is preserved.
- Region (C): The temperature is high enough to also exceed the liquidus lines. The sample is now fully molten, which leads to LSD and a complete loss of OR

The processes happening during the melting and solidification of the alloy are still not fully understood. In region B) residual crystals which are present along the liquid phase led to a heterogeneous crystallization and therefore to a preservation of the OR. In region C) other processes occur which lead to a crystallization that does not consider the substrate and therefore the OR is lost. These explanations are mainly assumptions, especially for the loss of OR, as a similar behaviour was not yet published in literature. In order to investigate those processes and validate them, in-situ TEM heating experiments would give better insides into the change of morphology, together with the loss and formation of OR.

Overall, it was shown, that the advantages of combinatorial samples make it possible to observe changes in dewetting dynamics from one concentration to the other with way less samples needed. This makes combinatorial sample systems a powerful tool to enhance and accelerate research.

## 7 List of Figures

| Figure 1: Schematic representation of a Mullins type grooving at a grain boundary [8] 3                       |
|---|
| Figure 2: Schematic representation of the rim-pinch of mechanism and fingering instabilities                  |
| [9]   |
| Figure 3: The Rayleigh plateau instability of an elongated jet [11]4  |
| Figure 4: Winterbottom construction in dependency of wetting between particle and subtrate                    |
| [5] 5   |
| Figure 5: The graph shows that the average particle diameter in proportion to the initial film thickness [16] |
| thickness [10]  |
| Figure 6: Copper nanoparticles formed via a) LSD and b) SSD on a single crystalline sapphire                  |
| substrate [25]  |
| Figure 7: Influence of film thickness onto the melting temperature[33]11                                      |
| Figure 8: Influence of grain size onto the melting temperature[35]  |
| Figure 9: The phase diagram of Au and Ni [17]13   |
| Figure 10: a) Schematic depiction of an e-beam PVD process and b) the e-beam PVD device                       |
| used in this study [40]   |
| Figure 11: Interaction volume for SEM [43]17  |
| Figure 12: Monte carlo simulations of the electron path in a SEM device at different                          |
| acceleration voltages [42]  |
| Figure 13: Schematic depiction of an EBSD measurement [48]  |
| Figure 14: Examplary process of the Hough transform for EBSD measurements [50] 21                             |
| Figure 15: Procedure for transforming EBSD data into a pole figure [51]22                                     |
| Figure 16: Schematic representation of milling and deposition with a FIB [52]24                               |

| Figure 17: Differences between CTEM and STEM imaging [54]26                                      |
|--|
| Figure 18: Schematic representation how a combinatorial library of different compositions can    |
| be created [63]30  |
| Figure 19: 3D model of the gradient samples  |
| Figure 20: EDX measurements on an unheated sample35  |
| Figure 21: STEM cross section of an unheated sample with EDX measurements 36                     |
| Figure 22: Local XRD measurements of a heated sample   |
| Figure 23: a) Exposed over unexposed area, b) particle density, c) ECD and d) circularity of     |
| samples heated at 875 °C for 120 s and 3600 s  |
| Figure 24: SEM images of samples heated at 875 °C for 120 s and 3600 s40                         |
| Figure 25: a) Exposed over unexposed area, b) particle density, c) ECD and d) circularity of     |
| samples heated at 900 °C, 910 °C and 920 °C for 120 s42  |
| Figure 26: SEM images of samples heated at 900 °C, 910 °C and 920 °C for 120 s 43                |
| Figure 27: Pole figures from EBSD measurements of samples heated at 900 °C, 910 °C and           |
| 920 °C for 120 s   |
| Figure 28: a) Exposed over unexposed area, b) particle density, c) ECD and d) circularity of the |
| 1000C 120s and 2step samples   |
| Figure 29: SEM images of the 1000C 120s and 2step samples  |
| Figure 30: Pole figures from EBSD measurements of the 1000C 120s and 2step samples 50            |
| Figure 31: Lattice parameter, concentration and integrated intensity of the XRD measurments      |
| at different positions522  |
| Figure 32: Overview of the areas of fast-dewetting for samples heated at 910 °C and 920 °C       |
| 58   |

| Figure 33: Morphology comparisiopn of samples heated at 910 °C and 920 °C with a sample  |
|--|
| heated at 1000 °C59  |
| Figure 34: Depiction of the OR I and OR II distribution via EBSD maps at 900 °C  |
| Figure 35: Comaprision of the texture loss and fast-dewetting are of samples heated at 910 °C and 920 °C63   |
| Figure 36: The 3 Regions of dewetting on the 2step sample, in dependacy of the heating temperature   |
| Figure A1: The positions of the XRD measurements were used to firstly calculate the lattice parameter and then afterwards compare the values with concentration values from literature |
| Figure A2: MUD plots of the EBSD measurements made from samples heated at 900 °C, 910 °C and 920 °C  |
| Figure A3: MUD plots of the 1000C 30s and 2step sample81   |
| Figure A4: The fits of the XRD measurements at measuring position a) 0.5 mm, b) 1 mm, c) 1.5 mm, d) 2 mm, e) 2.5 mm and f) 3 mm82  |
| Figure A5: The fits of the XRD measurements at measuring position a) 3.5 mm, b) 4 mm and c)  |

## 8 References

- [1] F. Shahvaranfard, P. Ghigna, A. Minguzzi, E. Wierzbicka, P. Schmuki, and M. Altomare, "Dewetting of PtCu Nanoalloys on TiO2Nanocavities Provides a Synergistic Photocatalytic Enhancement for Efficient H2Evolution," *ACS Appl Mater Interfaces*, vol. 12, no. 34, pp. 38211–38221, Aug. 2020, doi: 10.1021/acsami.0c10968.
- [2] K. Loza, M. Heggen, and M. Epple, "Synthesis, Structure, Properties, and Applications of Bimetallic Nanoparticles of Noble Metals," *Advanced Functional Materials*, vol. 30, no. 21. Wiley-VCH Verlag, May 01, 2020. doi: 10.1002/adfm.201909260.
- [3] R. A. Hughes, E. Menumerov, and S. Neretina, "When lithography meets self-Assembly: A review of recent advances in the directed assembly of complex metal nanostructures on planar and textured surfaces," *Nanotechnology*, vol. 28, no. 28. Institute of Physics Publishing, Jun. 22, 2017. doi: 10.1088/1361-6528/aa77ce.
- [4] F. Leroy *et al.*, "How to control solid state dewetting: A short review," *Surface Science Reports*, vol. 71, no. 2. Elsevier, pp. 391–409, Jun. 01, 2016. doi: 10.1016/j.surfrep.2016.03.002.
- [5] W. L. Winterbottom, "Equilibrium shape of a small particle in contact with a foreign substrate," Acta Metallurgica, vol. 15, no. 2, 1967, doi: 10.1016/0001-6160(67)90206-4.
- [6] C. V. Thompson, "Solid-state dewetting of thin films," *Annual Review of Materials Research*, vol. 42. 2012. doi: 10.1146/annurev-matsci-070511-155048.
- [7] W. W. Mullins, "Theory of Thermal Grooving," *J Appl Phys*, vol. 28, no. 3, 1957, doi: 10.1063/1.1722742.
- [8] D. Amram, L. Klinger, N. Gazit, H. Gluska, and E. Rabkin, "Grain boundary grooving in thin films revisited: The role of interface diffusion," *Acta Mater*, vol. 69, pp. 386–396, 2014, doi: 10.1016/j.actamat.2014.02.008.
- [9] R. V. Zucker, G. H. Kim, W. Craig Carter, and C. V. Thompson, "A model for solid-state dewetting of a fully-faceted thin film," *Comptes Rendus Physique*, vol. 14, no. 7. pp. 564–577, Aug. 2013. doi: 10.1016/j.crhy.2013.06.005.

- [10] J. Fowlkes, S. Horton, M. Fuentes-Cabrera, and P. D. Rack, "Signatures of the rayleigh-plateau instability revealed by imposing synthetic perturbations on nanometer-sized liquid metals on substrates," *Angewandte Chemie International Edition*, vol. 51, no. 35, pp. 8768–8772, Aug. 2012, doi: 10.1002/anie.201202113.
- [11] C. Zhao, J. E. Sprittles, and D. A. Lockerby, "Revisiting the Rayleigh-Plateau instability for the nanoscale," *J Fluid Mech*, vol. 861, p. R3, Feb. 2019, doi: 10.1017/jfm.2018.950.
- [12] G. Wulff, "XXV. Zur Frage der Geschwindigkeit des Wachsthums und der Auflösung der Krystallflächen," Z Kristallogr Cryst Mater, vol. 34, no. 1–6, 1901, doi: 10.1524/zkri.1901.34.1.449.
- [13] H. Sadan and W. D. Kaplan, "Au-Sapphire (0001) solid-solid interfacial energy," in *Journal of Materials Science*, Aug. 2006, pp. 5099–5107. doi: 10.1007/s10853-006-0437-5.
- [14] D. J. Lewis, L. Z. Zornberg, D. J. D. Carter, and R. J. Macfarlane, "Single-crystal Winterbottom constructions of nanoparticle superlattices," *Nat Mater*, vol. 19, no. 7, pp. 719–724, Jul. 2020, doi: 10.1038/s41563-020-0643-6.
- [15] H. Meltzman, D. Chatain, D. Avizemer, T. M. Besmann, and W. D. Kaplan, "The equilibrium crystal shape of nickel," *Acta Mater*, vol. 59, no. 9, pp. 3473–3483, May 2011, doi: 10.1016/j.actamat.2011.02.021.
- [16] Y. Kojima and T. Kato, "Nanoparticle formation in Au thin films by electron-beam-induced dewetting," *Nanotechnology*, vol. 19, no. 25, 2008, doi: 10.1088/0957-4484/19/25/255605.
- [17] H. Okamoto, M. E. Schlesinger, and E. M. Mueller, "Binary Alloy Phase Diagrams," in *Alloy Phase Diagrams*, 2018. doi: 10.31399/asm.hb.v03.a0006247.
- [18] A. Devaraj *et al.*, "Grain boundary segregation and intermetallic precipitation in coarsening resistant nanocrystalline aluminum alloys," *Acta Mater*, vol. 165, 2019, doi: 10.1016/j.actamat.2018.09.038.
- [19] D. Raabe *et al.*, "Grain boundary segregation engineering in metallic alloys: A pathway to the design of interfaces," *Current Opinion in Solid State and Materials Science*, vol. 18, no. 4. Elsevier Ltd, pp. 253–261, 2014. doi: 10.1016/j.cossms.2014.06.002.

- [20] H. Barda and E. Rabkin, "Improving the thermal stability of nickel thin films on sapphire by a minor alloying addition of gold," *Appl Surf Sci*, vol. 484, pp. 1070–1079, Aug. 2019, doi: 10.1016/j.apsusc.2019.04.176.
- [21] Y. Wang, W. Jiang, W. Bao, and D. J. Srolovitz, "Sharp interface model for solid-state dewetting problems with weakly anisotropic surface energies," *Phys Rev B Condens Matter Mater Phys*, vol. 91, no. 4, 2015, doi: 10.1103/PhysRevB.91.045303.
- [22] L. Kondic, A. G. Gonzalez, J. A. Diez, J. D. Fowlkes, and P. Rack, "Liquid-State Dewetting of Pulsed-Laser-Heated Nanoscale Metal Films and Other Geometries," *Annual Review of Fluid Mechanics*, vol. 52. 2020. doi: 10.1146/annurev-fluid-010719-060340.
- [23] A. Atena and M. Khenner, "Thermocapillary effects in driven dewetting and self assembly of pulsed-laser-irradiated metallic films," *Phys Rev B Condens Matter Mater Phys*, vol. 80, no. 7, 2009, doi: 10.1103/PhysRevB.80.075402.
- [24] F. Ruffino and M. G. Grimaldi, "Nano-shaping of gold particles on silicon carbide substrate from solid-state to liquid-state dewetting," *Surfaces and Interfaces*, vol. 24, Jun. 2021, doi: 10.1016/j.surfin.2021.101041.
- [25] S. Curiotto *et al.*, "Orientation relationships of copper crystals on c-plane sapphire," *Acta Mater*, vol. 59, no. 13, pp. 5320–5331, Aug. 2011, doi: 10.1016/j.actamat.2011.05.008.
- [26] J. Wang and S. Q. Wang, "Surface energy and work function of fcc and bcc crystals: Density functional study," *Surf Sci*, vol. 630, 2014, doi: 10.1016/j.susc.2014.08.017.
- [27] H. J. Fecht and H. Gleiter, "A lock-in model for the atomic structure of interphase boundaries between metals and ionic crystals," *Acta Metallurgica*, vol. 33, no. 4, 1985, doi: 10.1016/0001-6160(85)90019-7.
- [28] G. Dehm, B. J. Inkson, and T. Wagner, "Growth and microstructural stability of epitaxial Al films on (0001)  $\alpha$ -Al 2 O 3 substrates," 2002. [Online]. Available: www.actamat-journals.com
- [29] C. J. Palmstroem, "EPITAXY OF DISSIMILAR MATERIALS," 1995. [Online]. Available: www.annualreviews.org

- [30] S. W. Hieke, B. Breitbach, G. Dehm, and C. Scheu, "Microstructural evolution and solid state dewetting of epitaxial Al thin films on sapphire (α-Al2O3)," *Acta Mater*, vol. 133, pp. 356–366, Jul. 2017, doi: 10.1016/j.actamat.2017.05.026.
- [31] W. H. Qi and M. P. Wang, "Size and shape dependent melting temperature of metallic nanoparticles," *Mater Chem Phys*, vol. 88, no. 2–3, pp. 280–284, Dec. 2004, doi: 10.1016/j.matchemphys.2004.04.026.
- [32] A. Van Teijlingen, S. A. Davis, and S. R. Hall, "Size-dependent melting point depression of nickel nanoparticles," *Nanoscale Adv*, vol. 2, no. 6, pp. 2347–2351, Jun. 2020, doi: 10.1039/d0na00153h.
- [33] M. Zhang *et al.*, "Size-dependent melting point depression of nanostructures: Nanocalorimetric measurements," *Phys Rev B Condens Matter Mater Phys*, vol. 62, no. 15, 2000, doi: 10.1103/PhysRevB.62.10548.
- [34] A. Kryshtal, A. Minenkov, S. Bogatyrenko, and A. Gruszczyński, "Melting process and the size depression of the eutectic temperature in Ag/Ge and Ge/Ag/Ge layered films," *J Alloys Compd*, vol. 786, pp. 817–825, May 2019, doi: 10.1016/j.jallcom.2019.01.383.
- [35] T. Wejrzanowski, M. Lewandowska, K. Sikorski, and K. J. Kurzydlowski, "Effect of grain size on the melting point of confined thin aluminum films," *J Appl Phys*, vol. 116, no. 16, Oct. 2014, doi: 10.1063/1.4899240.
- [36] M. Gassner *et al.*, "Energy consumption and material fluxes in hard coating deposition processes," *Surf Coat Technol*, vol. 299, 2016, doi: 10.1016/j.surfcoat.2016.04.062.
- [37] M. Vorobyova *et al.*, "PVD for Decorative Applications: A Review," *Materials*, vol. 16, no. 14. 2023. doi: 10.3390/ma16144919.
- [38] C. Metzner, K. Goedicke, G. Hoetzsch, B. Scheffel, and J. P. Heinss, "Electron beam-PVD for enhanced surface properties on metallic strips and sheets," *Surf Coat Technol*, vol. 94–95, 1997, doi: 10.1016/S0257-8972(97)00515-X.
- [39] G. S. Fox-Rabinovich, I. S. Gershman, and S. Veldhuis, "Thin-film pvd coating metamaterials exhibiting similarities to natural processes under extreme tribological conditions," *Nanomaterials*, vol. 10, no. 9. 2020. doi: 10.3390/nano10091720.

- [40] A. Bashir, T. I. Awan, A. Tehseen, M. B. Tahir, and M. Ijaz, "Chapter 3 Interfaces and surfaces," in *Chemistry of Nanomaterials*, 2020.
- [41] K. D. Vernon-Parry, "Scanning Electron Microscopy: an introduction," *III-Vs Review*, vol. 13, no. 4, 2000.
- [42] D. C. Joy and J. B. Pawley, "High-resolution scanning electron microscopy," *Ultramicroscopy*, vol. 47, no. 1–3, 1992, doi: 10.1016/0304-3991(92)90186-N.
- [43] By Antonis Nanakoudis, "SEM: Types of Electrons and the Information They Provide."

  Accessed: Nov. 29, 2023. [Online]. Available: https://www.thermofisher.com/blog/materials/sem-signal-types-electrons-and-the-information-they-provide/
- [44] A. J. Wilkinson and T. Ben Britton, "Strains, planes, and EBSD in materials science," *Materials Today*, vol. 15, no. 9. 2012. doi: 10.1016/S1369-7021(12)70163-3.
- [45] S. Suzuki, "Features of transmission EBSD and its application," *JOM*, vol. 65, no. 9, 2013, doi: 10.1007/s11837-013-0700-6.
- [46] S. D. Sitzman, "Introduction to EBSD analysis of micro- to nanoscale microstructures in metals and ceramics," in *Testing, Reliability, and Application of Micro- and Nano-Material Systems II*, 2004. doi: 10.1117/12.542082.
- [47] K. Z. Baba-Kishi, "Electron backscatter Kikuchi diffraction in the scanning electron microscope for crystallographic analysis," *Journal of Materials Science*, vol. 37, no. 9. 2002. doi: 10.1023/A:1014964916670.
- [48] M. A. Jackson, M. A. Groeber, M. D. Uchic, D. J. Rowenhorst, and M. De Graef, "h5ebsd: an archival data format for electron back-scatter diffraction data sets," *Integr Mater Manuf Innov*, vol. 3, no. 1, 2014, doi: 10.1186/2193-9772-3-4.
- [49] C. Maurice and R. Fortunier, "A 3D Hough transform for indexing EBSD and Kossel patterns," in *Journal of Microscopy*, 2008. doi: 10.1111/j.1365-2818.2008.02045.x.
- [50] © Oxford Instruments, "Basics of Automated Indexing." Accessed: Nov. 29, 2023.

  [Online]. Available: https://www.ebsd.com/ebsd-explained/basics-of-automated-indexing

- [51] I. Salzmann and R. Resel, "STEREOPOLE: Software for the analysis of X-ray diffraction pole figures with IDL," *J Appl Crystallogr*, vol. 37, no. 6, 2004, doi: 10.1107/S002188980402165X.
- [52] S. Reyntjens and R. Puers, "A review of focused ion beam applications in microsystem technology," *Journal of Micromechanics and Microengineering*, vol. 11, no. 4. 2001. doi: 10.1088/0960-1317/11/4/301.
- [53] P. D. Nellist, "Scanning transmission electron microscopy," in *Springer Handbooks*, 2019. doi: 10.1007/978-3-030-00069-1\_2.
- [54] S. G. Wolf, E. Shimoni, M. Elbaum, and L. Houben, "STEM Tomography in Biology," 2018. doi: 10.1007/978-3-319-68997-5 2.
- [55] B. Fultz and J. M. Howe, *Transmission electron microscopy and diffractometry of materials*. 2008. doi: 10.1007/978-3-540-73886-2.
- [56] A. Chauhan, "Powder XRD Technique and its Applications in Science and Technology," *J Anal Bioanal Tech*, vol. 5, no. 6, 2014, doi: 10.4172/2155-9872.1000212.
- [57] F. Smend, M. Schumacher, and I. Borchert, "The Z-dependence of the elastic scattering of γ-rays," *Nuclear Physics, Section A*, vol. 213, no. 2, 1973, doi: 10.1016/0375-9474(73)90152-8.
- [58] H. Daimon and I. Tanaka, "Z-dependence of forward scattering peak intensity of electron by atoms," *Chem Phys Lett*, vol. 806, 2022, doi: 10.1016/j.cplett.2022.140003.
- [59] P. J. McGinn, "Thin-film processing routes for combinatorial materials investigations a review," *ACS Comb Sci*, vol. 21, no. 7, pp. 501–515, Jul. 2019, doi: 10.1021/acscombsci.9b00032.
- [60] A. Ludwig, "Discovery of new materials using combinatorial synthesis and high-throughput characterization of thin-film materials libraries combined with computational methods," *npj Computational Materials*, vol. 5, no. 1. Nature Publishing Group, Dec. 01, 2019. doi: 10.1038/s41524-019-0205-0.
- [61] R. B. Merrifield, "Solid Phase Peptide Synthesis. I. The Synthesis of a Tetrapeptide," *J Am Chem Soc*, vol. 85, no. 14, 1963, doi: 10.1021/ja00897a025.

- [62] W. F. Maier, K. Stowe, and S. Sieg, "Combinatorial and high-throughput materials science," *Angewandte Chemie International Edition*, vol. 46, no. 32. pp. 6016–6067, 2007. doi: 10.1002/anie.200603675.
- [63] S. S. Mao and P. E. Burrows, "Combinatorial screening of thin film materials: An overview," *Journal of Materiomics*, vol. 1, no. 2. Chinese Ceramic Society, pp. 85–91, Jun. 01, 2015. doi: 10.1016/j.jmat.2015.04.002.
- [64] J. R. Clinton, E. H. Tyler, and H. L. Luo, "Electrical and magnetic properties of Au-Ni alloys," *Journal of Physics F: Metal Physics*, vol. 4, no. 8, 1974, doi: 10.1088/0305-4608/4/8/012.
- [65] A. F. Crawley, "Lattice vacancies and diffusion in the gold-nickel alloy system," University of Glasgow (United Kingdom), Glasgow, 1965.
- [66] M. Oliva-Ramirez, P. Schade, C. Zobel, D. Wang, and P. Schaaf, "Morphological and compositional mapping of supersaturated AuNi alloy nanoparticles fabricated by solid state dewetting," *Applied Surface Science Advances*, vol. 4, 2021, doi: 10.1016/j.apsadv.2021.100082.
- [67] M. M. J. Treacy, "Z dependence of electron scattering by single atoms into annular dark-field detectors," *Microscopy and Microanalysis*, vol. 17, no. 6, 2011, doi: 10.1017/S1431927611012074.
- [68] H. Barda and E. Rabkin, "Metal hetero-diffusion along the metal-ceramic interfaces: A case study of Au diffusion along the Ni-sapphire interface," *Acta Mater*, vol. 186, 2020, doi: 10.1016/j.actamat.2019.12.051.
- [69] M. Dierner *et al.*, "Influence of Au Alloying on Solid State Dewetting Kinetics and Texture Evolution of Ag and Ni Thin Films," *under review*, 2023.
- [70] A. M. Brown and M. F. Ashby, "CORRELATIONS FOR DIFFUSION CONSTANTS.," Acta Metallurgica, vol. 28, no. 8, 1980, doi: 10.1016/0001-6160(80)90092-9.
- [71] R. Brandon and F. J. Bradshaw, "The mobility of the surface atoms of copper and silver evaporated deposits," *Tech. Rep.*, vol. 66095R, 1966.
- [72] O. Pierre-Louis, A. Chame, and Y. Saito, "Dewetting of a solid monolayer," *Phys Rev Lett*, vol. 99, no. 13, 2007, doi: 10.1103/PhysRevLett.99.136101.

- [73] J. Sopoušek *et al.*, "Au-Ni nanoparticles: Phase diagram prediction, synthesis, characterization, and thermal stability," *CALPHAD*, vol. 58, 2017, doi: 10.1016/j.calphad.2017.05.002.
- [74] P. Herre *et al.*, "Rapid fabrication and interface structure of highly faceted epitaxial Ni-Au solid solution nanoparticles on sapphire," *Acta Mater*, vol. 220, 2021, doi: 10.1016/j.actamat.2021.117318.
- [75] G. Kaptay, J. Janczak-Rusch, G. Pigozzi, and L. P. H. Jeurgens, "Theoretical analysis of melting point depression of pure metals in different initial configurations," in *Journal of Materials Engineering and Performance*, 2014. doi: 10.1007/s11665-014-0885-z.
- [76] C. Mitterer, P. H. Mayrhofer, and J. Musil, "Thermal stability of PVD hard coatings," in *Vacuum*, 2003. doi: 10.1016/S0042-207X(02)00751-0.
- [77] Z. Fogarassy, G. Dobrik, L. K. Varga, L. P. Biró, and J. L. Lábár, "Growth of Ni layers on single crystal sapphire substrates," *Thin Solid Films*, vol. 539, 2013, doi: 10.1016/j.tsf.2013.05.077.
- [78] D. Amram and E. Rabkin, "On the role of Fe in the growth of single crystalline heteroepitaxial Au thin films on sapphire," *Acta Mater*, vol. 61, no. 11, pp. 4113–4126, Jun. 2013, doi: 10.1016/j.actamat.2013.03.038.

## 9 Appendix

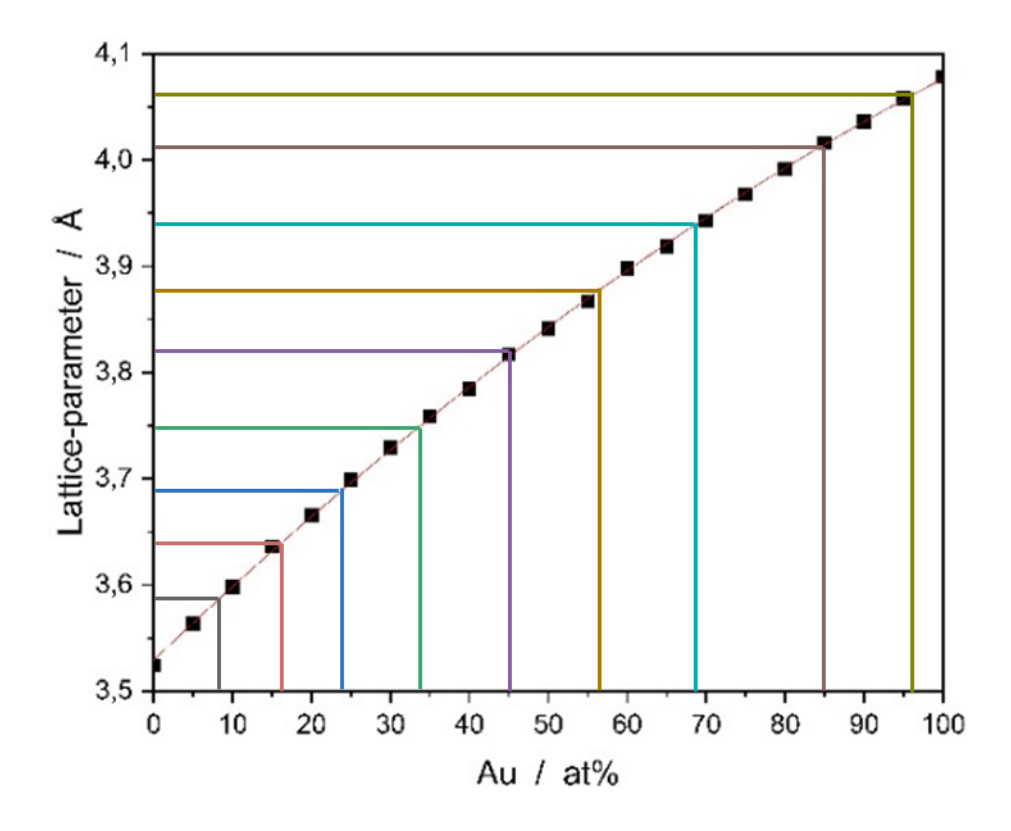


Figure A1: The positions of the XRD measurements were used to firstly calculate the lattice parameter and then afterwards compare the values with concentration values from literature [65].

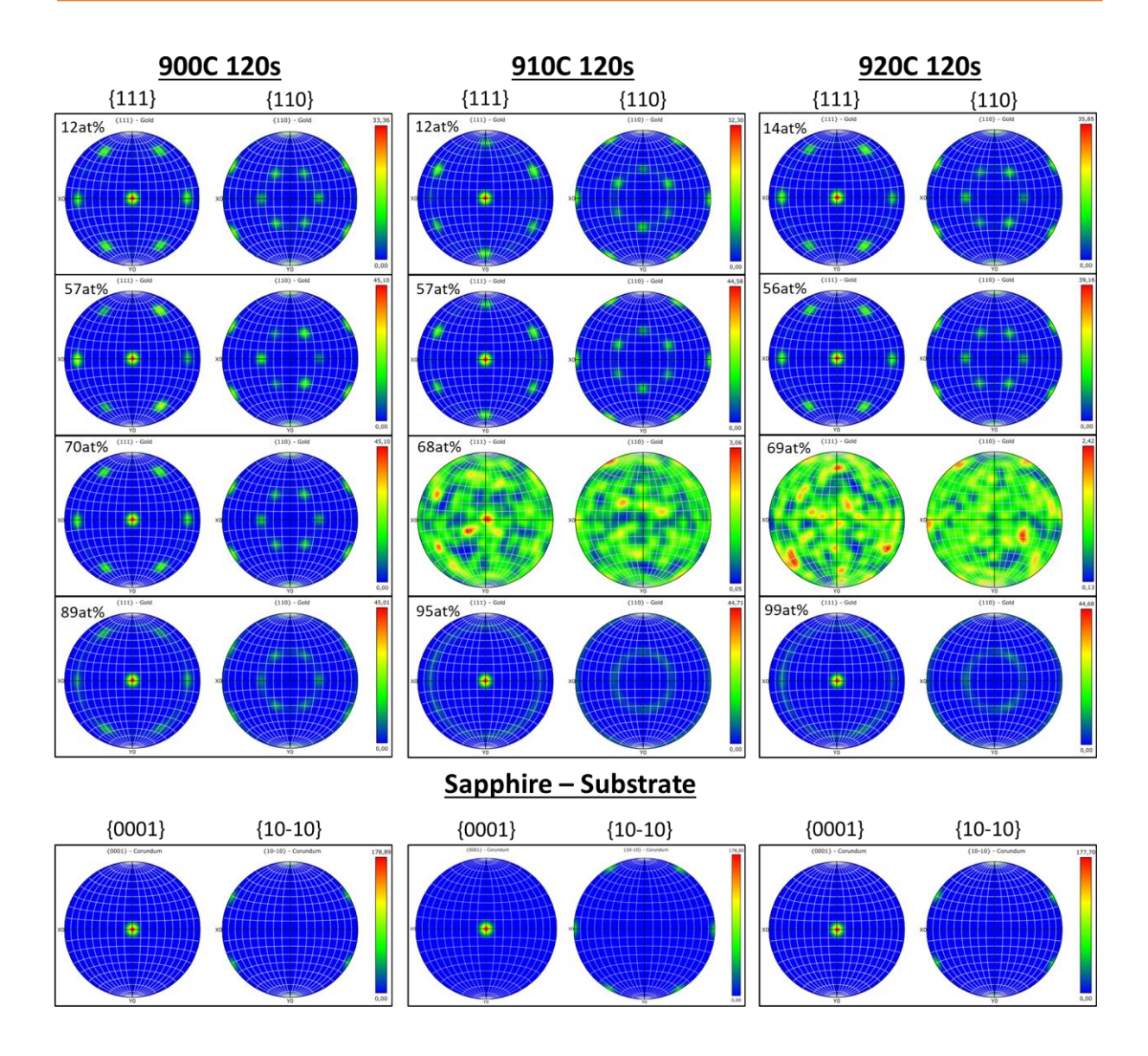


Figure A2: MUD plots of the EBSD measurements made from samples heated at 900 °C, 910 °C and 920 °C.

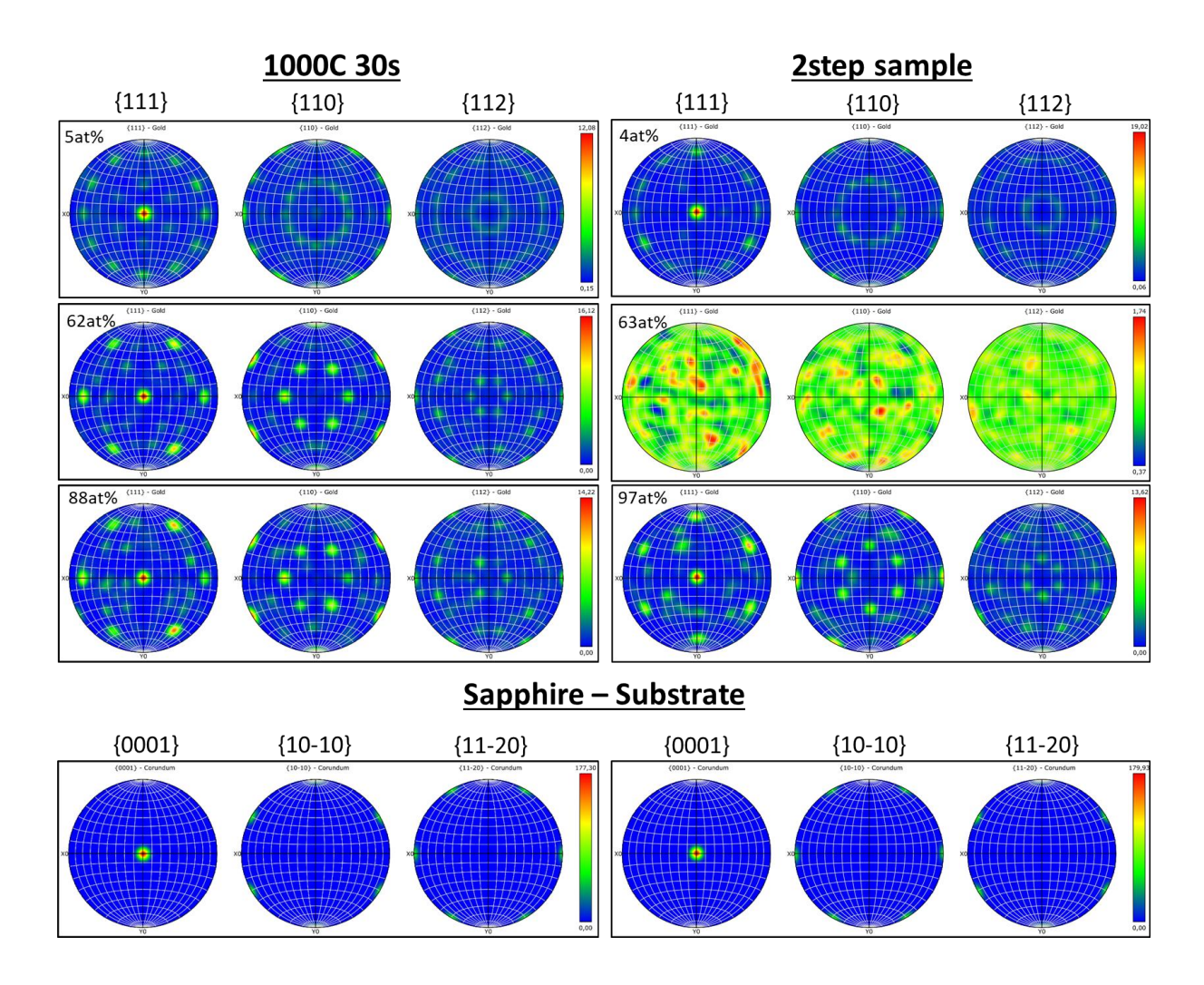


Figure A3: MUD plots of the 1000C 30s and 2step sample.

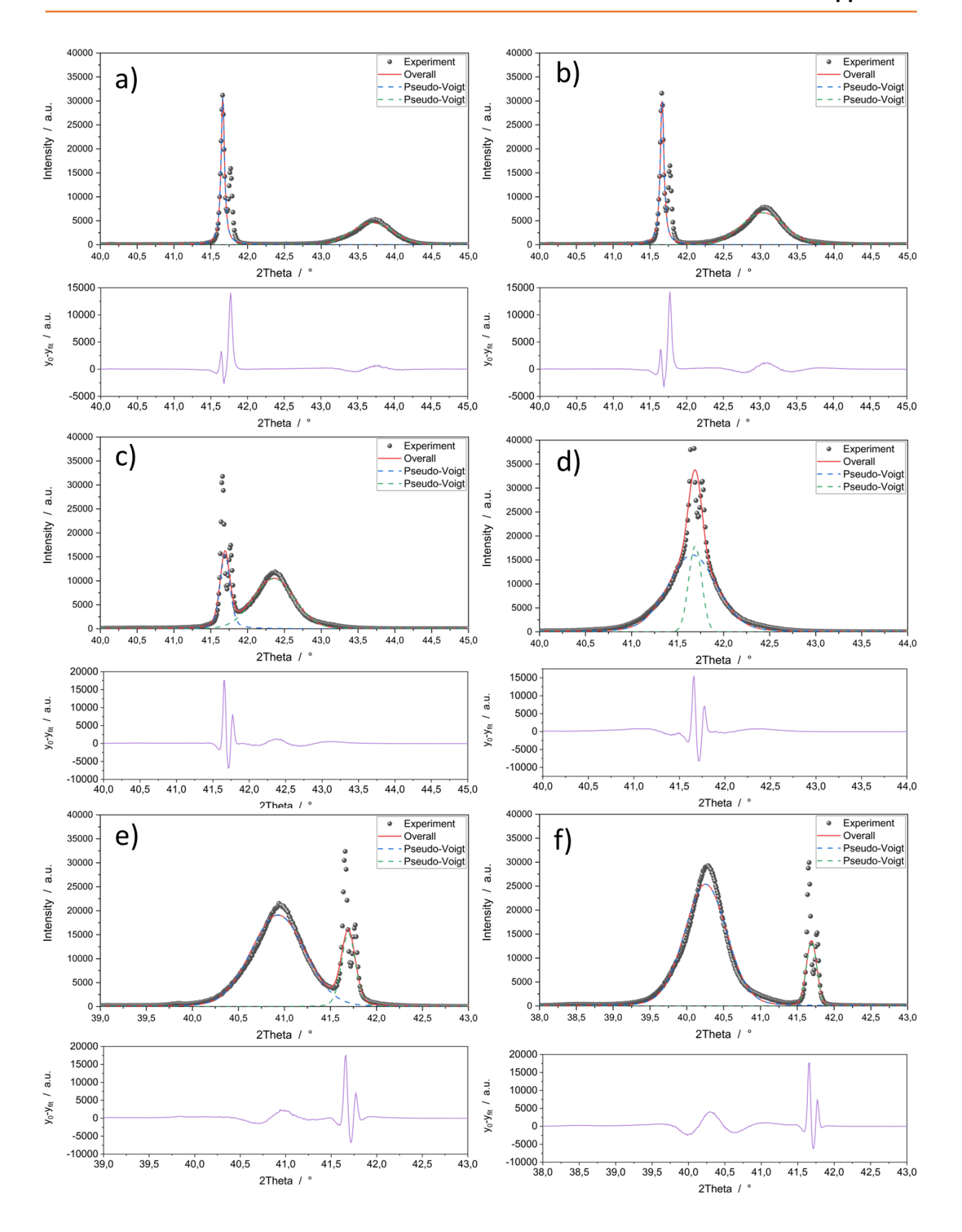


Figure A4: The fits of the XRD measurements at measuring position a) 0.5 mm, b) 1 mm, c) 1.5 mm, d) 2 mm, e) 2.5 mm and f) 3 mm.

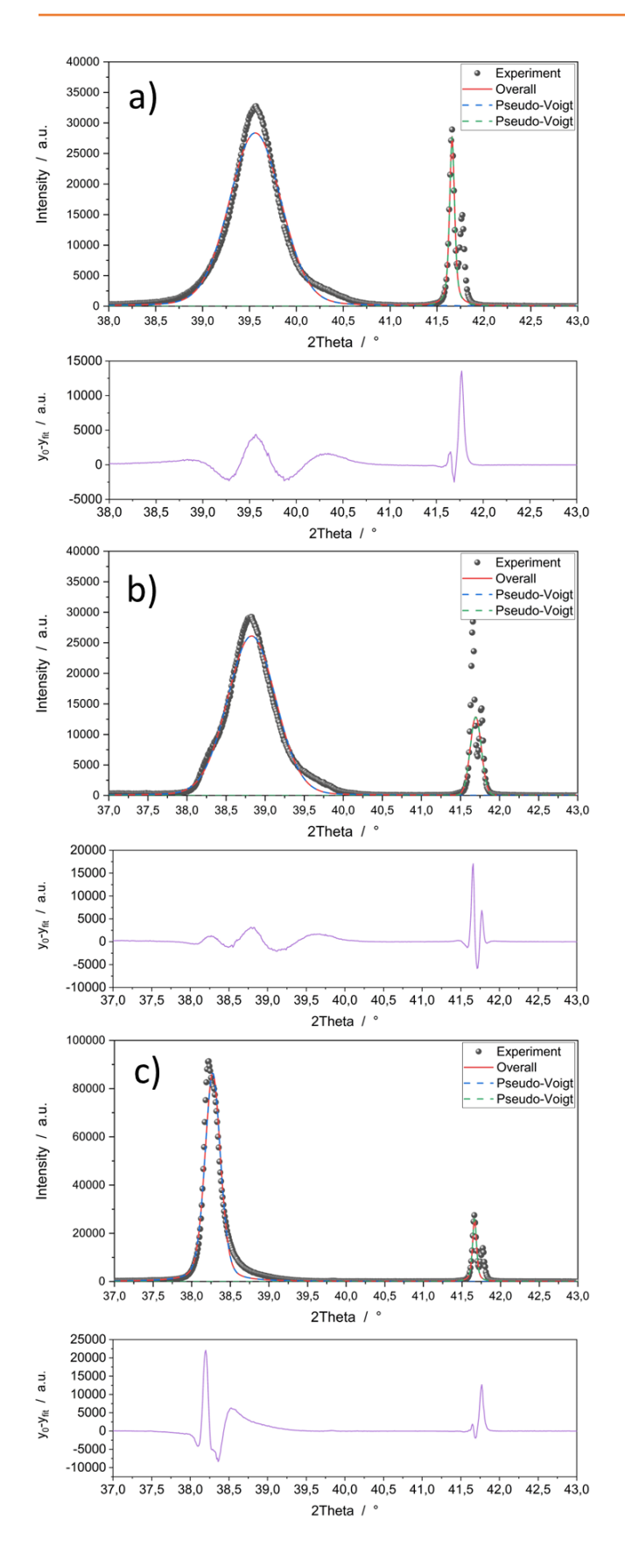


Figure A5: The fits of the XRD measurements at measuring position a) 3.5 mm, b) 4 mm and c) 4.5 mm